

A 2-D Visualisation Study of the Mechanisms behind Increased Recovery due to Polymer Injection in Sandstone

Master's Thesis
Petroleum Technology – Reservoir Physics

Svenn Erik Grønnestad



Department of Physics and Technology



Centre for Integrated Petroleum Research

University of Bergen

November 2011

Acknowledgement

I would like to express my gratitude towards my supervisor, Professor Arne Skauge, for his guidance and support during the work of this thesis. Discussions both on and off the subject with Arne have truly been valuable.

Special thanks go to the always-accommodating Bartek Vik and Per Arne Ormehaug for helping with experimental procedures and data processing. Thanks to Sverre Hetland for helping on the lab and to Tiril Gurholt for providing filtered images.

Further, I would also like to thank the Centre for Integrated Petroleum Research for providing research facilities and an office during my course of study. I am also grateful for all my fellow students and colleagues at the Faculty of Mathematics and Natural Sciences for social discussions and activities, especially Simen Bergsli, Sigbjørn Lunestad, Eivind Norheim, Rune Myredal Ludvigsen and Katrine Bergøy, which have been a motivating factor throughout these five years at the University of Bergen.

Thanks to my partner in crime, Ingvild Klokk, for valuable collaboration and endless discussions throughout this thesis. It has been an interesting journey, and I look forward to continue the team work in our professional career.

Finally, I would like to thank the rest of my friends and family for their support, especially Karoline for being there for me the last three years.

Svenn Erik Grønnestad

Bergen, November 2011

Abstract

The potential of synthetic polymer injection, such as hydrolysed polyacrylamide (HPAM), in reservoirs has been a field of study since the 1960's [1]. The main intension of polymer injection is to improve the problems with water injection due to high mobility ratio between oil and water and reservoir heterogeneity. Polymers are added to injection water in order to increase the viscosity and reduce the mobility ratio. Though polymers have been thought to only improve the volumetric sweep and not the microscopic sweep, recent research argue the opposite due to viscoelastic effects and high residual oil saturation after water injection. The application of water and polymer injections in viscous to heavy oils were also regarded as non beneficial, but new research proposes a favourable recovery of viscous oils. However, because the mechanisms behind polymer injection in viscous oil reservoirs are poorly understood in virtue of high fluid complexity and the non Newtonian behaviour, more research is required.

In this thesis, a two-dimensional core scanner is used to perform a combination of in-situ high resolution X-ray imaging of fluid movements and gamma-ray counts of fluid saturation. Together with rheological effluent analysis, this is used in order to identify mechanisms behind increased recovery of viscous crude oil by the use of HPAM. Two identical Bentheimer sandstone rock samples (named WF+PF and PF) are used to observe the difference between a primary and secondary polymer injection. To investigate the effect polymer may have on the displacement of oil, an initial condition with dampened capillary pressure is preferred. Ageing the rock material with crude oil at elevated temperature is assumed to alter wettability and thereby dampen capillarity.

Earlier experiments performed with the two-dimensional core scanner at the Centre for Integrated Petroleum Research (CIPR), have proved the scanner suitable for in-situ high resolution X-ray imaging in order to observe finger behaviour at both miscible and immiscible displacements [2, 3].

For this thesis, effluent dispersion tests revealed homogeneous samples, where flow was little affected by dead-end pore volume, but more affected by the configuration of the inlet and outlet. The ageing process at 70°C for six weeks, gave a moderate change in wettability from strongly water-wet. This was supported by the relative oil permeability for both samples and the observed fingering and capillary end-effects in the WF+PF sample.

No distinct oil bank was observed in the secondary polymer injection in the WF+PF sample. However, the water-cut was kept constant, and it is impossible to exclude the effect of the polymer. The primary polymer injection in the PF sample showed a more piston-like displacement compared to the water injection in the WF+PF sample. The polymer front arrived 0.4 pore volumes earlier than the dispersion front in the WF+PF sample, something which indicates inaccessible pore volume and depleted layer effects.

The final recovery in both samples after polymer injection was similar, but it was achieved in different time scales. In the PF sample it only took approximately one pore volume (*PV*) of polymer solution to obtain the same recovery as it took for the WF+PF sample, with approximately 1 *PV* of polymer in addition to 1 *PV* of water. This indicates that a direct polymer injection accelerates the recovery. The high recovery might be explained by the high-permeable porous medium and few dead-end pores, i.e. good hydraulically communication. No dramatic change in polymer viscosity was observed in effluent fluids, which indicate little mechanical degradation and mixing between polymer and resident water. The chase water injection into the polymer solution showed an unstable miscible displacement between the two fluids.

An unexpected phenomenon was observed during both polymer injections, where a dark ring surrounded the injection front. The effluent analysis confirmed no connate water banking, and it was verified by comparing images to the volume injected, that the darker area was a correct description of the displacement.

Nomenclature

Variables

A	adsorption, $\text{g} \cdot \text{g}^{-1}$
A	area, cm^2
C	concentration, $\text{g} \cdot \text{cm}^{-3}$
C	constant, dimensionless
c	concentration, $\text{g} \cdot \text{cm}^{-3}$
C_0	initial concentration, $\text{g} \cdot \text{cm}^{-3}$
d_p	average particle diameter, cm
D	dispersion/diffusion coefficient, $\text{cm}^2 \cdot \text{s}^{-1}$
D_0	bulk molecular diffusion coefficient, $\text{cm}^2 \cdot \text{s}^{-1}$
D_e	effective molecular diffusion coefficient, $\text{cm}^2 \cdot \text{s}^{-1}$
D_p	frontal advance loss, dimensionless
E_R	recovery factor, dimensionless
F	formation resistivity factor, dimensionless
I	Amott-Harvey index, dimensionless
h	height, cm
J	flux, $\text{mol} \cdot \text{cm}^{-2} \cdot \text{s}^{-1}$
K	absolute permeability, m^2 ($1\text{D} = 9.87 \cdot 10^{-13} \text{m}^2$)
$k_{e,i}$	effective permeability of phase i, m^2 ($1\text{D} = 9.87 \cdot 10^{-13} \text{m}^2$)
k_{ri}	relative permeability of phase i, dimensionless
L	length, cm
M	mobility ratio, dimensionless
N	oil reserves, m^3
N_{Pe}	Peclet number, dimensionless
N_{Re}	Reynold`s number, dimensionless
N_{vc}	capillary number, dimensionless
P	pressure, bar
PV	pore volume, dimensionless

Q	flow rate, $\text{cm}^3 \cdot \text{s}^{-1}$
r, R	radius, cm
S	saturation, dimensionless
t	time, s
t_D	dimensionless time, dimensionless
u	darcy velocity, $\text{cm} \cdot \text{s}^{-1}$
V	volume, cm^3
WC	water-cut, dimensionless
X	measured concentration, $\Omega \cdot \text{m} / \text{count} \cdot \text{s}^{-1} / \text{cP}$
δ	depleted layer, cm
Δ	difference, dimensionless
γ	shear rate, s^{-1}
θ	contact angle, $^\circ$
λ	mobility, $\text{m}^2 \cdot (\text{cP})^{-1}$
μ	viscosity, cP
ρ	density, $\text{g} \cdot \text{cm}^{-3}$
σ	interfacial tension, $\text{N} \cdot \text{m}^{-1}$
τ	shear stress, Pa
φ	porosity, dimensionless

Subscripts

A	area
abs	absolute
b	bulk
BT	breakthrough
c	capillary
D	microscopic
dead	dead volume
e	end

eff	effective
i	component (phase)
i	irreducible
i	initial
i	concentration (NaI)
ineff	ineffective
j	concentration (NaCl)
o	oil
pol	polymer
p	pore
p	produced
r	relative
r	residual
rem	remaining
R	recovery
sp	spontaneous
tot	total
V	vertical
vol	volumetric
w	water
w	well

Abbreviations

2-D	two-dimensional
bbbl	oil barrel
CDC	capillary desaturation curve
CF	capillary force
CIPR	Centre for Intergrated Petroleum Research
CP	cone plate

DG	double gap
EOR	enhanced oil recovery
IOR	improved oil recovery
IPV	inaccessible pore volume
HPAM	hydrolysed polyacrylamide
PF	polymer flooding sample
PFA	perfluoroalkoxy
ppm	parts per million
R&D	research and development
rpm	revolutions per minute
UV	ultraviolet
VF	viscous force
WF+PF	waterflooding and polymer flooding sample

Table of Contents

ACKNOWLEDGEMENT	III
ABSTRACT	V
NOMENCLATURE	IX
TABLE OF CONTENTS	XV
1 INTRODUCTION	1
2 THEORY AND BACKGROUND	5
2.1 ENHANCED OIL RECOVERY	5
2.1.1 <i>Mobility</i>	8
2.1.2 <i>Residual and remaining oil saturation</i>	10
2.1.3 <i>Capillary number</i>	12
2.1.4 <i>EOR with polymers</i>	14
2.2 PETROPHYSICAL PROPERTIES	15
2.2.1 <i>Porosity</i>	15
2.2.2 <i>Permeability</i>	16
2.2.3 <i>Fluid saturation</i>	18
2.2.4 <i>Effective and relative permeability</i>	18
2.2.5 <i>Wettability</i>	19
2.2.6 <i>Wettability alteration</i>	21
2.2.7 <i>Capillary pressure</i>	23
2.3 SANDSTONE ROCK SAMPLE	25
2.4 POLYMERS.....	27
2.4.1 <i>HPAM structure</i>	28
2.4.2 <i>Rheology</i>	29
2.4.3 <i>Retention</i>	31
2.4.4 <i>Inaccessible pore volume and depleted layer</i>	32
2.5 MISCIBLE DISPLACEMENT	34
2.5.1 <i>Diffusion</i>	34
2.5.2 <i>Dispersion</i>	35

2.6	IMMISCIBLE DISPLACEMENT	39
2.6.1	<i>Drainage</i>	39
2.6.2	<i>Imbibition</i>	40
2.6.3	<i>Capillary end-effect</i>	42
2.7	UNSTABLE DISPLACEMENT.....	43
2.7.1	<i>Viscous fingering</i>	44
3	EXPERIMENTAL	45
3.1	PREPARATION OF THE POROUS MEDIUM	45
3.2	CHEMICALS	49
3.3	FLUIDS	50
3.4	2-D CORE SCANNER	52
3.4.1	<i>X-ray imaging</i>	55
3.4.2	<i>Image processing</i>	57
3.4.3	<i>Image filtration</i>	58
3.4.4	<i>Sources of error</i>	59
3.4.5	<i>Image quality and cutting limits</i>	61
3.5	PUMP AND ASSOCIATED EQUIPMENT.....	62
3.5.1	<i>Valves, fittings and tubing</i>	63
3.5.2	<i>Piston and measuring cylinders</i>	63
3.6	PROCEDURES	65
3.6.1	<i>Porosity and permeability measurements</i>	65
3.6.2	<i>Effluent dispersion test</i>	68
3.6.3	<i>Drainage and wettability alteration</i>	70
3.6.4	<i>Polymer solution</i>	73
3.6.5	<i>Viscosity measurements</i>	74
4	RESULTS AND DISCUSSION	77
4.1	POROUS MEDIA CHARACTERISATION	77
4.1.1	<i>Porosity and oil saturation</i>	77
4.1.2	<i>Effective permeability</i>	78
4.1.3	<i>Relative permeability and mobility ratio</i>	78
4.1.4	<i>Effluent dispersion tests</i>	80

4.2	THE WATER FLOODING AND POLYMER FLOODING SAMPLE (WF+PF).....	91
4.2.1	<i>Water injection</i>	91
4.2.2	<i>Polymer injection</i>	95
4.2.3	<i>Chase water injection</i>	99
4.2.4	<i>Recovery</i>	103
4.2.5	<i>Overall discussion WF+ PF sample</i>	106
4.3	THE POLYMER FLOODING SAMPLE (PF).....	107
4.3.1	<i>Direct polymer injection</i>	107
4.3.2	<i>Chase water injection</i>	110
4.3.3	<i>Recovery</i>	113
4.3.4	<i>Overall discussion PF sample</i>	115
4.4	COMPARISON AND SUMMARY OF RESULTS	116
4.5	CONCENTRATION AND RESIDUAL OIL SATURATION.....	118
4.6	IMAGE FILTRATION	127
5	CONCLUSIONS	129
6	RECOMMENDATIONS AND FURTHER WORK.....	131
7	REFERENCES.....	133
	APPENDIX A: DIFFERENTIAL PRESSURE – MAIN INJECTIONS	139
	APPENDIX B: DIFFERENTIAL PRESSURE – ABSOLUTE PERMEABILITY	142
	APPENDIX C: DIFFERENTIAL PRESSURE – RELATIVE PERMEABILITY.....	144

1 Introduction

The importance of oil in the world cannot be overstated, and methods for recovering oil will be the subject of much scientific and engineering research for many years to come [1]. Nations such as China and India, with over one third of the world's population, are growing economically faster than anyone could have predicted. This growth puts an enormous pressure on the world energy demand (*Figure 1.1*).

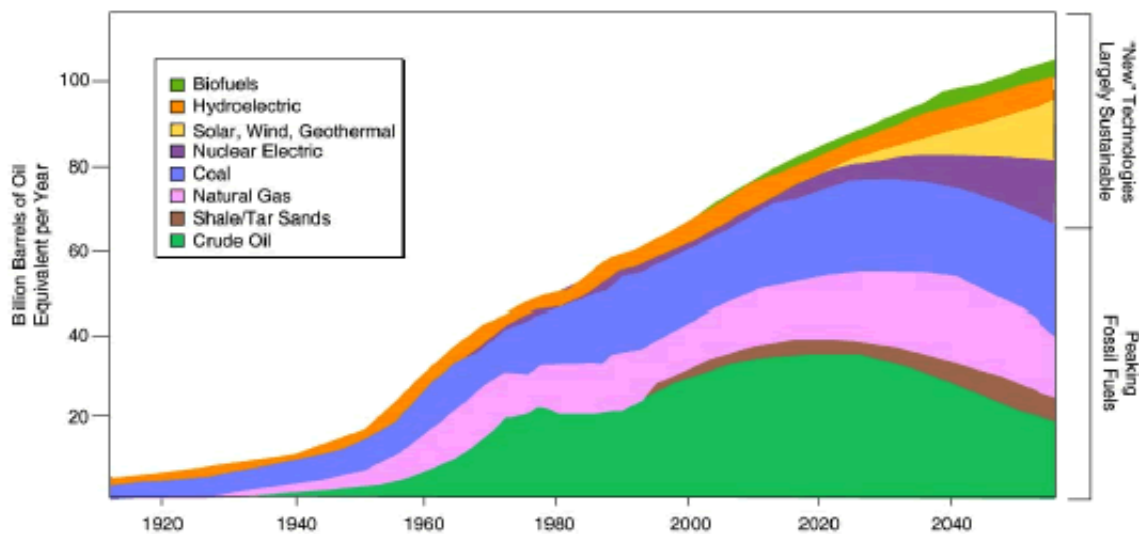


Figure 1.1 World energy demand for long term energy resources [4].

In order to meet the growing demand for energy, both renewable and non-renewable energy companies must continue to develop technology and increase efficiency. If renewable energy resources are to become sustainable and more cost efficient, funding from technology companies (e.g. the oil and gas industry) is required. To ensure investments in renewable technology, oil and gas companies need to profit from their own business.

However, the oil and gas industry faces new challenges as much of the large conventional oil and gas reserves is expected to already have been found and produced. This forces the industry to move into new areas with unconventional oil and gas resources, e.g. higher pressure, temperature and viscous to heavy oils, in addition to exploiting the maximum out of existing fields. The remaining hydrocarbon potential after the application of conventional oil recovery technology is so vast that the successful use of improved oil recovery (IOR) must remain a major industry goal [1].

Enhanced oil recovery (EOR) using polymers in injection water have been an area of investigation for many years. The main objective of polymer injection is to improve the problems with water injection, caused by high mobility ratio between oil and water, or because of reservoir heterogeneity. Polymers were first suggested in the early 1960's as a means of reducing the mobility ratio by increasing the injection water viscosity and therefore reducing the formation permeability [1]. On the Norwegian Continental Shelf (NCS), research on polymer injection was under investigation especially during the 80's and 90's, but the large decrease in oil price forced the industry to stop further research.

The focus on enhanced oil recovery has grown once again together with the increased price of oil, where high oil prices opens up new possibilities for oil and gas exploration as it allows for new technology to be applied. Recent research concerning polymer injection is emerging all over the world, and the most used type of polymer in enhanced oil recovery is HPAM, due to its availability and environmental benefits.

Polymers have commonly been applied in reservoirs containing oils with low to medium viscosity, but recently oil viscosities of several thousand centipoises are investigated. Numerous studies [5-7] which have appeared recently specifically targets the application of polymer injection in heavy oil reservoirs. These studies have shown a clear potential for polymer flooding in heavy crudes with viscosity as high as 10 000 centipoise (cP). It has also been reported that simple water injection performs well at unfavourable viscosity ratios, which is explained by capillary forces and imbibition in a water-wet context. Capillary pressure and imbibition become more important as the injection rates become low enough and capillary forces have time to act [8].

Even though polymer injection is thought to mostly improve the sweep efficiency and not reduce the residual oil saturation, some argue the opposite. A polymer injection can reduce the residual oil saturation of viscous oils if it is sufficiently high enough after water injection, but this effect diminishes with an increased degree of heterogeneity [9]. Some authors [10-12] argue that the reduction of residual oil saturation results from the viscoelastic behaviour that HPAM shows at high shear rates. At such shear rates, the HPAM molecules are stretched and become more elastic, i.e. viscoelastic. This viscoelastic behaviour of HPAM makes the solution displace immobile oil in dead-end pores, which was regarded as unable to produce.

Identifying mechanisms behind enhanced oil recovery is important experimental research, and The Centre for Integrated Petroleum Research (CIPR) has developed an experimental setup to specifically study viscous unstable displacements for both miscible and immiscible displacements by the use of a two-dimensional core scanner. The scanner has been used to investigate viscous unstable miscible fingering in both sandstone and carbonate material [2]. X-ray imaging of porous media allows for visual observations of frontal displacements, and can reveal such mechanisms in different types of porous material.

Because the mechanisms behind the injection of polymer into heavy oil reservoirs are poorly understood in virtue of high fluid complexity and the non-Newtonian flow behaviour, more research needs to be implemented. The two-dimensional core scanner at CIPR was used to investigate such mechanisms in Bentheimer material for heavy oil (7000 cP at 23°C) at both pore and core scale together with rheological measurements [3].

The two latter sections above form the basis of the work performed in this thesis, where Bentheimer material is used together with viscous oil (53 cP at 23°C) to investigate mechanisms behind the increased recovery in two similar samples, one with a primary and a secondary polymer injection. These investigations are performed by applying the two-dimensional core scanner together with rheological effluent fluid analysis.

2 Theory and Background

This chapter will review the theoretical aspects of this experimental thesis. Sufficient theoretical background material is intended to understand the different mechanisms during oil displacement by water and especially polymer.

2.1 Enhanced oil recovery

With a growing global demand for energy, leading to an increase in the oil price, new techniques are continuously being developed to extract more hydrocarbons from petroleum reservoirs. In this context, it means methods to improve recovery from existing fields and to maximise the recovery for future reservoirs. Such methods are known as EOR. The term EOR is narrower than improved oil recovery (IOR), and has mostly been used to describe the tertiary recovery methods. New research investigates the possibilities for primary and secondary recovery by EOR processes [13].

The definition of EOR is linked to the use of unconventional recovery methods, and is referred to as “*oil recovery by the injection of materials normally not present in the reservoir*” [14]. Examples of such materials can be polymers, surfactants or Low Salinity water (LowSal) to name a few. Recent research examines the possibilities of a combination of these methods, also known as hybrid EOR [15, 16].

Water injection is the most used secondary recovery method, cost are relatively low and the efficiency high. However, after water injection, a large amount of oil is still left in the reservoir (*Figure 2.1*). The oil is immobilised either by capillary forces, i.e. residual oil, or left behind as unswept oil.

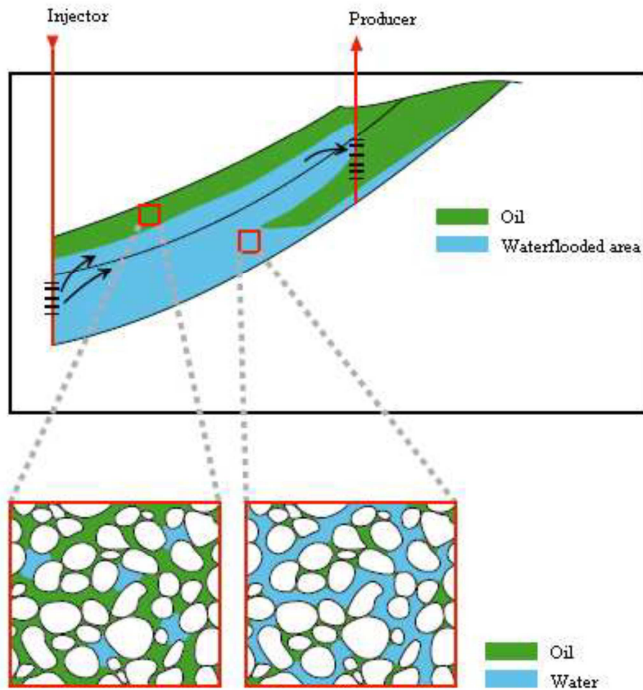


Figure 2.1 Oil distribution after water injection [17].

The injection of water into heavy oil reservoirs have been regarded as non-beneficial due to the unfavourable mobility ratio. This problem is currently under investigation [3]. A number of studies [5-7] have appeared recently which specifically target the application of polymer injection in heavy oil reservoirs. These studies have shown a clear potential for polymer flooding in heavy crudes with a viscosity as high as 10.000 cP. On the other hand it has been reported that ordinary water injection also performs relatively well at very unfavourable viscosity ratios [8].

In the 1980's and 90's a large number of Research & Development (R&D) projects were funded by the authorities and industry on the Norwegian Continental Shelf (NCS), investigating the possibility for polymer flooding. As a result of the high prices for chemicals, such as polymers, the EOR projects came to a sudden stop in the mid 90's, when the oil price plunged to about 10-15 USD/bbl [18]. Projects were abandoned over night and valuable competence was lost.

Since the 90's, the industry has recovered from the low oil price, the interests for EOR implementations has increased as a result of the decline in oil production and hence incline of the oil price.

The amount of oil which can be produced from a reservoir depends on the initial conditions (i.e. rock properties and fluid saturation distribution), production strategy and the will to adopt new technology.

The recovery displacement efficiency is defined as the ratio of produced reserves to reserves in place:

$$E_R = \frac{N_p}{N} = E_D \cdot E_V \cdot E_A = E_D \cdot E_{vol} \tag{Equation 2.1}$$

where E_R is the recovery efficiency, N_p are the produced reserves, N are the total reserves, and E_D , E_V , E_A and E_{vol} are the microscopic, vertical, area and volumetric displacement sweep efficiencies respectively. E_D and E_{vol} are defined as [18]:

$$E_D = \frac{\text{Volume of oil displaced}}{\text{Volume of oil contacted}} \tag{Equation 2.2}$$

$$E_{vol} = \frac{\text{Volume of oil contacted}}{\text{Volume of oil originally in place}} \tag{Equation 2.3}$$

Volumetric sweep efficiency is shown in *Figure 2.2* and is the product of vertical and area sweep efficiency.

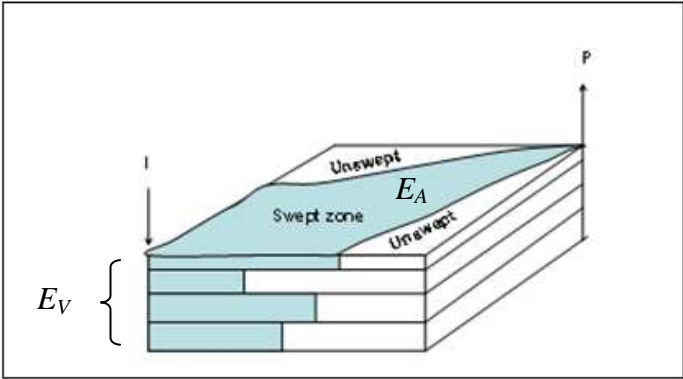


Figure 2.2 Vertical (E_V) versus area (E_A) sweep displacement efficiency [18].

The main objective for all EOR methods is to improve the volumetric sweep efficiency and enhance the microscopic displacement efficiency, or both compared to an ordinary water injection.

2.1.1 Mobility

Mobility is a measure of how easily a phase, i.e. water, oil or gas, flows through a porous medium in multiphase flow [18, 19]. It is given as the ratio between the effective permeability and the viscosity to the phase:

$$\lambda_i = \frac{k_{e,i}}{\mu_i} \quad \text{Equation 2.4}$$

where λ is the mobility, k_e is the effective permeability and μ is the viscosity of phase i .

The mobility ratio is defined as the ratio between the mobility of the displacing fluid (water) and the mobility of the displaced fluid (oil):

$$M = \frac{\lambda_w}{\lambda_o} = \frac{k_{rw} \cdot \mu_o}{k_{ro} \cdot \mu_w} \quad \text{Equation 2.5}$$

where M is the mobility ratio and k_{rw} and k_{ro} are the relative permeability for water and oil respectively. The term relative permeability will be discussed under chapter 2.2.4.

Mobility is often given in terms of end point relative permeability values:

$$M^0 = \frac{\lambda_w^0}{\lambda_o^0} = \frac{k_{rw,or} \cdot \mu_o}{k_{ro,iw} \cdot \mu_w} \quad \text{Equation 2.6}$$

where M^0 is the endpoint mobility ratio, $k_{rw,or}$ is the relative permeability for water at residual oil saturation (S_{or}), meaning that only water is flowing. $k_{ro,iw}$ is the relative permeability for oil at irreducible water saturation (S_{iw}), i.e. only oil is flowing.

Favourable conditions for stable displacement are achieved when the mobility ratio between water and oil is equal to or less than one ($M^0 \leq 1$). This implies that oil is nearly piston displaced by water through the porous media. If the mobility of the displacing fluid is greater than for the fluid being displaced, the mobility ratio is said to be unfavourable ($M^0 > 1$).

The mobility ratio can be made more favourable by lowering the viscosity of oil, or increasing the viscosity of water by reducing the relative permeability of water [18]. Development of microscopic displacement efficiency with dimensionless time/pore volume injected (t_D/PV) for different mobility ratios are illustrated in *Figure 2.3*.

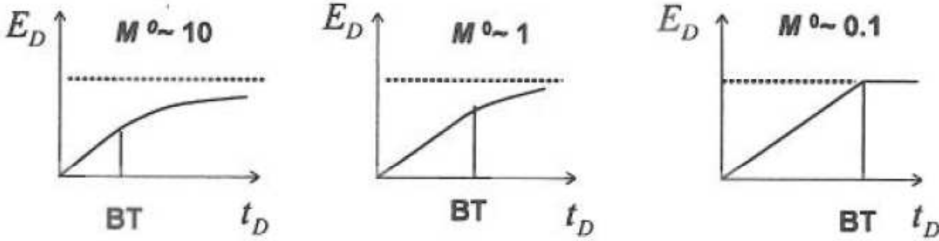


Figure 2.3 Relationship between endpoint mobility ratio (M^0) and microscopic displacement efficiency (E_D) as a function of dimensionless time (t_D/PV). The dashed line expresses the ultimate microscopic recovery efficiency, E_D^{max} [18].

However, no matter how low M^0 might be, the ultimate microscopic recovery is limited by the residual oil saturation:

$$E_D^{max} = 1 - \frac{S_{or}}{S_{oi}} \tag{Equation 2.7}$$

where E_D^{max} is the ultimate microscopic displacement efficiency, S_{or} is the residual oil saturation and S_{oi} is the initial oil saturation.

It is important to know that the mobility ratio is a Buckley-Leverett consideration, and is a shock-front description (piston-like displacement). This consideration is limited in a system with viscous fingering, hence the value calculated in such a system may not be entirely correct.

2.1.2 Residual and remaining oil saturation

The main intension for all oil production is to maximise the production, hence achieve the lowest possible oil saturation in the reservoir. Models have been made to describe the residual oil saturation after water injection. The two main mechanisms responsible for residual oil are snap-off and bypassing (pore doublet).

The residual oil is made immobile due to the surface tension between water and oil, i.e. the water pressure is unable to overcome the capillary pressure required to mobilise the oil [20]. In the pore doublet model, oil is trapped due to the capillary pressure and radii differences in two pores (*Figure 2.4*).

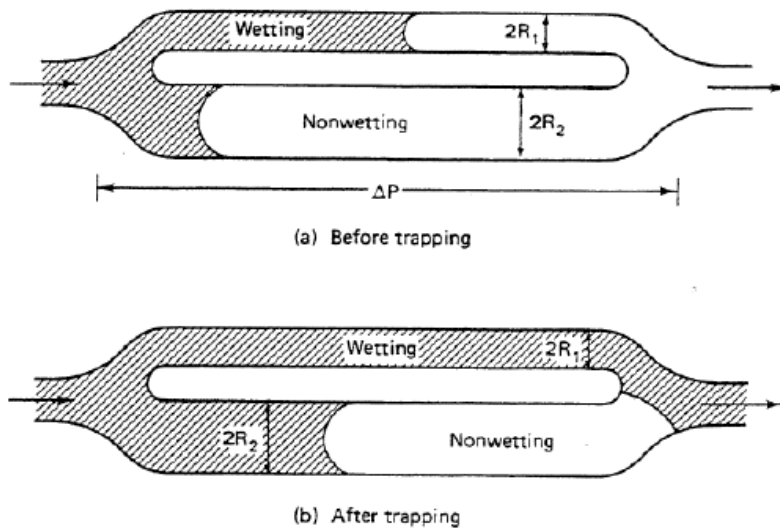


Figure 2.4 Pore doublet model. a) The wetting fluid intrudes the narrow channel quicker because of the capillary differences. b) Due to the capillary difference, the non-wetting fluid is left behind in the large pore [14].

In the snap-off model, residual oil is left behind because of water swelling around the oil until it snaps off in the pore throats and traps the oil in globules (*Figure 2.5*).

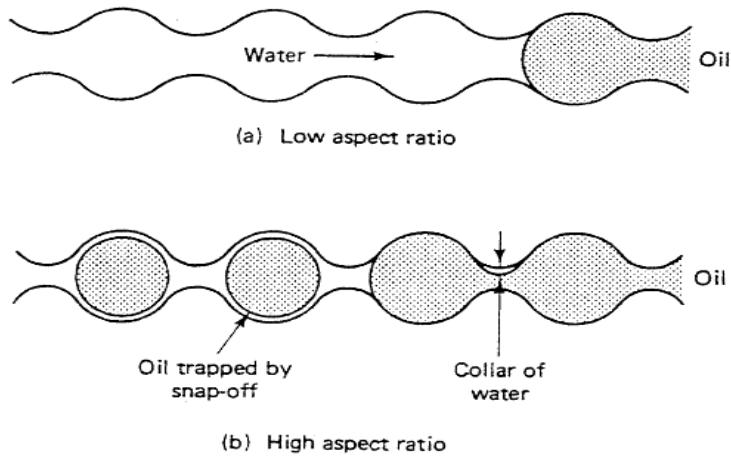


Figure 2.5 Different geometries of the snap-off model. a) Large pore throats. b) Small pore throats [20].

In any realistic porous medium, various combinations of both the pore doublet and snap-off model will occur. From detailed experimental observation in consolidated cores, it was determined that approximately 80% of the trapped non-wetting phase occurs in snap-off geometries, with the remaining 20% in pore doublet or in geometries that are combinations of both categories [20].

In a porous medium with unswept zones, e.g. a core sample, the known total oil saturation determined by material balance may be referred to as the remaining oil saturation ($S_{o,rem}$) and not the residual oil saturation.

2.1.3 Capillary number

The capillary number (N_{vc}), describes the dimensionless ratio between the viscous (VF) and capillary (CF) forces [21]:

$$N_{vc} = \frac{VF}{CF} = \frac{u \cdot \mu}{\sigma} \quad \text{Equation 2.8}$$

where u is the Darcy velocity of the displacing fluid, μ is the viscosity of the displacing fluid and σ is the interfacial tension (IFT) between the displaced and displacing fluid.

Studies [14, 20] show that the residual oil saturation correlates to the capillary number. To achieve as low residual oil saturation as possible, i.e. produce the maximum amount oil, the capillary number needs to be drastically increased. This can be achieved by adding polymers to the injection water in order to increase the viscosity. Darcy velocity can also be increased, but not significantly due to capacity and pressure limitations for the injection equipment.

Another definition of the capillary number is given below:

$$N_{vc2} = \frac{VF}{CF} = \frac{K \cdot \Delta P}{\sigma} \quad \text{Equation 2.9}$$

where K is the absolute permeability, ΔP is the pressure difference and σ is the interfacial tension between the displaced and displacing fluid. Subsequently, an increase in the absolute permeability or the pressure difference would increase the capillary number, as well as a reduction of the IFT.

Capillary desaturation curves (CDC) show the residual saturation as a function of the capillary number, as illustrated in *Figure 2.6* for different types of rock. It is a clear difference between the residual oil saturation for carbonate and well sorted sandstone. A bend in the curves occurs at the critical capillary number and the residual saturation starts to decrease. The region of low capillary number, where the residual saturation is constant, is called the plateau region. This is typically where traditional water flooding takes place [14].

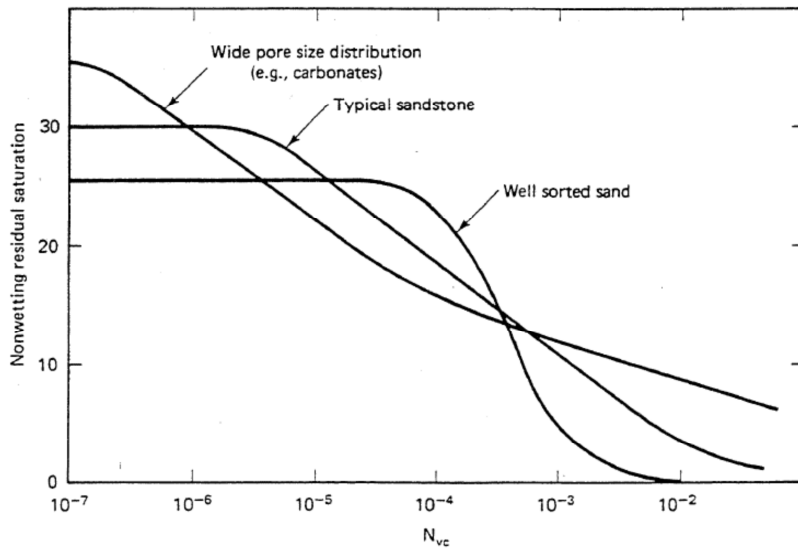


Figure 2.6 Relationship between the pore size distribution and capillary number [14].

The wettability of the rock affects the capillary desaturation curves [14]. The rock surface has a preference to the wetting phase and it is easier to mobilize the non-wetting phase. Therefore, a reduction in the residual saturation will occur at a lower capillary number than for the wetting phase (*Figure 2.7*).

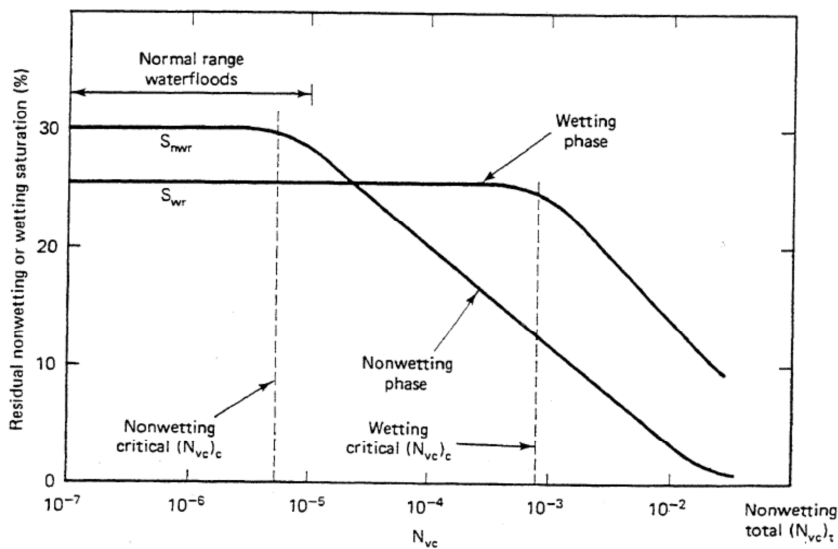


Figure 2.7 Relationship between the wettability and the capillary number [14].

2.1.4 EOR with polymers

Polymer injection will be favourable in reservoirs where the oil viscosity is high, or in reservoirs that are heterogeneous with oil bearing layers at different permeability [22]. The main intension with polymer injection is to improve sweep efficiency and accelerate production. Polymer injection is thought not to affect the residual oil compared to water injection. Residual oil is made up by disconnected oil which is immobilised as a result of capillary forces [23]. To mobilise the residual oil, the quantity of N_{vc} has to be increased by several orders of magnitude from the value it normally has in a waterflood ($N_{vc} \sim 10^{-6}$). The only realistic way to achieve this is by lowering the interfacial tension, σ_{ow} , between water and oil by adding for instance surfactants [1].

In the transition from water to polymer flooding, the viscous forces are usually considered to be increased by up to *one* order of magnitude, which is thought not to be sufficient to mobilise residual oil. Thus, the target for polymer flooding is considered to be any oil that is bypassed in the water injection and does not include in the residual oil [1].

However, recent studies [9] argues that a reduction in the residual oil saturation is possible. It was found that the impact of residual oil reduction by a polymer flood is more pronounced in reservoirs where residual oil saturations (S_{or}) are high at the start of a polymer flood. It was also shown that the impact of S_{or} reduction diminishes with increasing degree of heterogeneity.

Some authors [10-12], to name a few, argue that both sweep efficiency and S_{or} reduction may be caused by the viscoelastic behaviour of the polymer at high shear rates. This behaviour forces polymer molecules to stretch and become more elastic and hence displace dead-end pore oil, which is normally regarded as oil unable to produce.

2.2 Petrophysical properties

In oil recovery it is vital to make calculations to predict the quantity of oil that can be recovered from a reservoir. In order to understand fluid flow in porous medium, basic concepts and definitions of rock properties should be investigated.

2.2.1 Porosity

Porosity is a dimensionless parameter and is defined as the void part of the rock's total volume, unoccupied by the rock grains and mineral cement [24]. In the oil and gas industry porosity is referred to as a measure of the pore volume in the hydrocarbon reservoir. An example of pore volume is shown in *Figure 2.8*

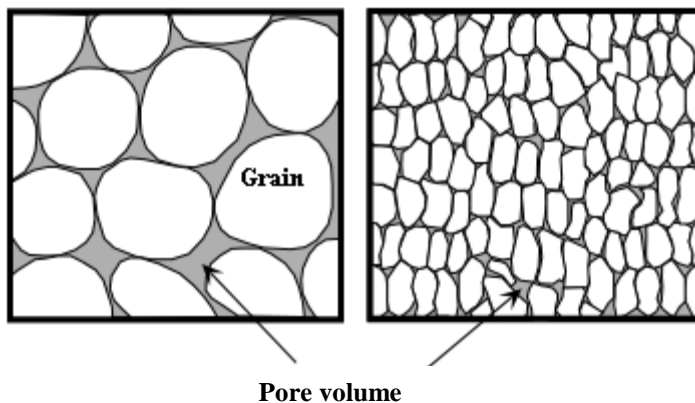


Figure 2.8 Illustration of pore volume.

The term porosity is divided into ineffective and effective porosity. Effective porosity is defined as the pore space which interconnects with other pores and allows fluid flow, whereas ineffective porosity includes the porosity which is closed for fluid flow.

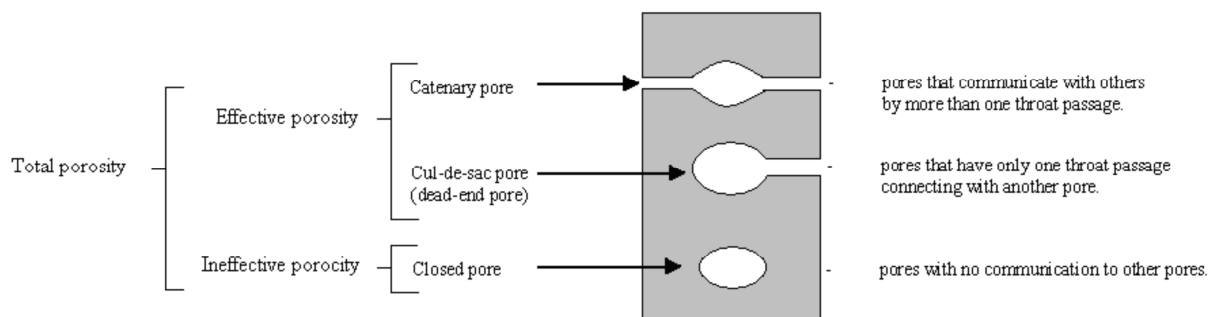


Figure 2.9 The three basic types of pores [25].

The three basic types of pores are shown in *Figure 2.9*. Cul-de-sac pores are also referred to as dead-end pores, and affect dispersion of tracer flow through the porous media. This will be discussed further under chapter 2.5.2.

Absolute porosity is the sum of effective and ineffective porosity:

$$\varphi_{\text{abs}} = \varphi_{\text{eff}} + \varphi_{\text{ineff}} \quad \text{Equation 2.10}$$

where φ_{abs} is the absolute porosity, φ_{eff} is the effective porosity and φ_{ineff} is the ineffective porosity.

However, there is no need in this thesis for the ineffective porosity, hence the equation above is reduced. Effective porosity can be defined as the ratio between the effective pore volume and the bulk volume:

$$\varphi_{\text{eff}} = \frac{V_{\text{p,eff}}}{V_{\text{b}}} \cdot 100\% \quad \text{Equation 2.11}$$

where $V_{\text{p,eff}}$ is the effective pore volume and V_{b} is the bulk volume to the rock.

Effective porosity depends on several factors, such as the rock type, grain size range, grain packing and orientation, cementation, weathering, leaching and type, content and hydration of clay minerals [24].

2.2.2 Permeability

Permeability of a porous medium is the medium's capability to transmit fluids through its network of interconnected pores. Permeability is described through Darcy's law, which for linear, horizontal flow is given by [24]:

$$Q = \frac{k \cdot A}{\mu} \cdot \frac{\Delta P}{L} \quad \text{Equation 2.12}$$

where Q is the volumetric flow rate, K is the absolute permeability, A is the cross sectional area, μ is the fluid viscosity, ΔP is the pressure difference over the medium and L is the length of the core sample.

The SI-unit of permeability is m^2 , but for practical purposes the much smaller unit Darcy ($1 \text{ D} = 9.87 \times 10^{-13} \text{ m}^2$) is commonly used. The permeability is often expressed in milliDarcy (mD). In reservoir rocks there is a wide range of the permeability, ranging from 0.1 mD to more than 30 D.

When the flow is vertical, gravity has to be taken into consideration and Darcy's law rewritten becomes:

$$Q = \frac{k \cdot A}{\mu} \left(\frac{\Delta P}{L} - \rho \cdot g \right) \quad \text{Equation 2.13}$$

where ρ is the fluid density and g is the gravity.

For radial flow (*Figure 2.10*), Darcy's law is defined as:

$$Q = \frac{2\pi \cdot h \cdot K}{\mu} \cdot \frac{P_e - P_w}{\ln(r_e/r_w)} \quad \text{Equation 2.14}$$

where h is the height of the sample, P_e is the pressure at the end of the sample, P_w is the pressure in the production well of the sample, r_e is the radius of the sample, and r_w is the radius of the well.

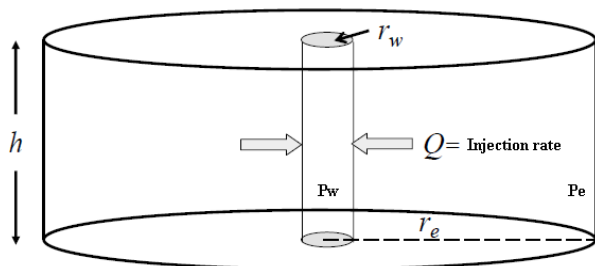


Figure 2.10 Radial flow toward a production well in a cylindrical shaped reservoir. Modified from Lien [26].

2.2.3 Fluid saturation

The amount of fluid contained in a porous medium is dependent on the porosity, but also on the saturation of a particular phase. A reservoir normally contains more than one fluid phase, e.g. oil, water and gas. The saturation of each phase is the volume fraction of the pore volume containing the respective phase:

$$S_i = \frac{V_i}{V_p} \quad \text{Equation 2.15}$$

where V_i is the volume of the fluid respectively, V_p is the pore volume and the subscript i denotes the phase.

The total saturation of the fluids is equal to one ($S_w+S_o=1$). Flow conditions are highly dependent on saturations when more than one fluid is present.

2.2.4 Effective and relative permeability

If more than one incompressible fluid is present in a porous medium, the permeability change drastically. Darcy's law when multiphase flow is present is changed and the permeability for each single phase is referred to as the effective permeability:

$$k_{e,i} = \mu_i \frac{L}{A} \frac{Q_i}{\Delta P_i} \quad \text{Equation 2.16}$$

Relative permeability is defined as the ratio between the effective permeability and the absolute permeability:

$$k_{r,i} = \frac{k_{e,i}}{k} \quad \text{Equation 2.17}$$

Relative permeability is strongly dependent on rock properties such as pore size distribution and wettability. Relative permeability for two phases (e.g. oil and water in a water-wet system) is schematically represented in *Figure 2.11*.

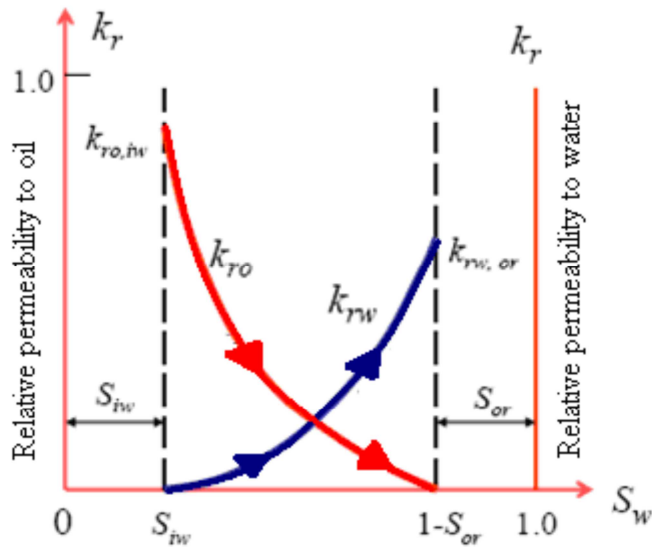


Figure 2.11 Relative permeability of an oil-water imbibition system [27].

The blue line in *Figure 2.11* represents the water phase whereas the red line represents the oil phase. $k_{ro,iw}$ and $k_{rw,or}$ are the endpoint relative permeability for oil and water, respectively. Note that oil is immobile at oil saturations lower than S_{or} , and that water is immobile at saturations lower than S_{iw} . S_{iw} is the irreducible water saturation.

2.2.5 Wettability

The wettability of a solid can be defined as the tendency of one fluid to spread on, or adhere to, a solid surface in the presence of another immiscible fluid [28]. The molecules of each fluid are to some degree attached to the molecules of an adjoining solid by an electrostatic force called adhesion. In a reservoir, where more than fluid is present, the most adhesive fluid sticks preferentially to the solid's surface is called the wetting fluid. The distribution of fluids in the rock pores reflects the balance between cohesive and adhesive forces [24]. The wettability of the pore walls depends on the chemical composition of the phases (e.g. the asphaltene content in the case of oil) and the mineral composition of the rock.

The wettability of a solid system is an important factor controlling the location, distribution and flow of fluids [29]. It has also been proven that changes in the wettability influence the electrical properties, capillary pressure, CDC, relative permeability, water flood behaviour and residual saturation [30].

The wettability of a reservoir rock can be estimated by measuring the angle between two liquids in the presence of a solid surface. This angle, called the contact angle, reflects the equilibrium between the interfacial tension of the two phases and their individual adhesive to the solid.

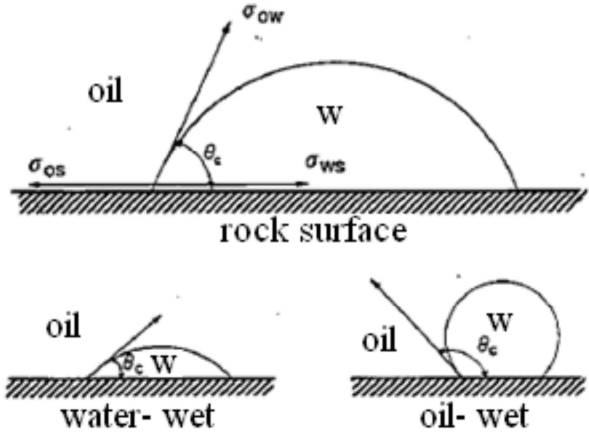


Figure 2.12 Contact angle and interfacial tension balance [30].

If the measured angle is less than 90°, the denser fluid is the wetting phase. If the angle is larger than 90°, the lighter fluid is considered to be the wetting phase. Most reservoirs are neither water nor oil-wet, but fall in between the two extremes. In an oil-water system the porous media can be classified according to the oil-water contact angle (Table 2.1).

Table 2.1 Wettability classification based on contact angle [29].

$0^\circ < \theta_{ow} < 75^\circ$	Water-wet
$75^\circ < \theta_{ow} < 105^\circ$	Intermediate-wet
$105^\circ < \theta_{ow} < 180^\circ$	Oil-wet

When the contact angle is around 90°, the rock is defined as neutral-wet. When a rock is neutral-wet it has no clear preference for either oil or water. Intermediate wettability is quite common in reservoirs [31].

2.2.6 Wettability alteration

The wettability of all reservoir rocks is initially water-wet pre-oil migration. When oil migrates into the reservoir, it starts to interact with the rock surface leading to an alteration of the wettability. The alteration is induced by the adsorption of polar compounds and/or the deposition of organic materials originally in the crude. The degree of alteration is determined by interaction of the oil constituents, the mineral surface, and the brine chemistry.

When performing core flooding experiments in the laboratory, wettability alteration is essential for the realism. If experiments are done with water-wet cores, the oil would solely be produced by spontaneous water imbibition, and an alteration in wettability is preferred.

The Amott-Harvey (I_{AH}) index is one way of measuring the wettability of porous media, and is defined as the water index (I_w) minus the oil index (I_o):

$$I_{AH} = I_w - I_o = \frac{V_{o,sp}}{V_{o,tot}} - \frac{V_{w,sp}}{V_{w,tot}} \quad \text{Equation 2.18}$$

where $V_{o,sp}$ is the volume of oil produced by spontaneous water imbibition, $V_{o,tot}$ is the total volume oil produced, $V_{w,sp}$ is the volume of water produced by spontaneous oil imbibition and $V_{w,tot}$ is the total volume of water produced. The Amott-Harvey index range from -1 to 1 (*Table 2.2*).

Table 2.2 Amott-Harvey index for wettability [30].

$0.3 < I_{AH} < 1$	Water-wet
$-0.3 < I_{AH} < 0.3$	Intermediate-wet
$-1 < I_{AH} < -0.3$	Oil-wet

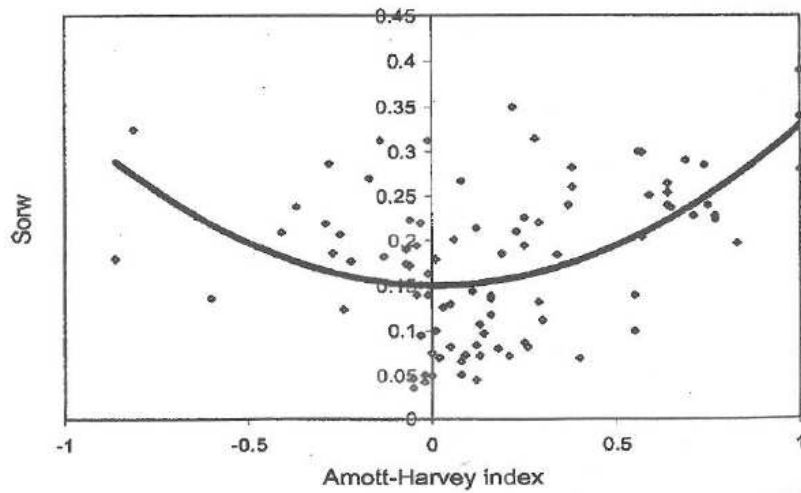


Figure 2.13 Residual oil saturation measured on cores from 30 different North Sea fields [18].

A large number of core analyses experiments on cores from the North Sea reservoirs have been carried out, and in *Figure 2.13* residual oil saturation for the cores in 30 fields have been measured. There are varying results, but the thick trend line show a smiling face shape and the lowest residual oil saturation (i.e. highest recovery) is obtained in the intermediate section of the scale.

2.2.7 Capillary pressure

Capillary pressure is defined as the molecular pressure difference across an interface in a capillary separating two immiscible phases at equilibrium. The pressure difference in this case results from the difference in both cohesive (internal) and adhesive (external) electrostatic forces acting upon the two fluids [24].

For the fluids and their interface to be at static equilibrium, a stronger pressure is required in the non-wetting phase due to wetting preference of the capillary. This can be illustrated in *Figure 2.14* where a capillary tube with radius r is suppressed in water and oil.

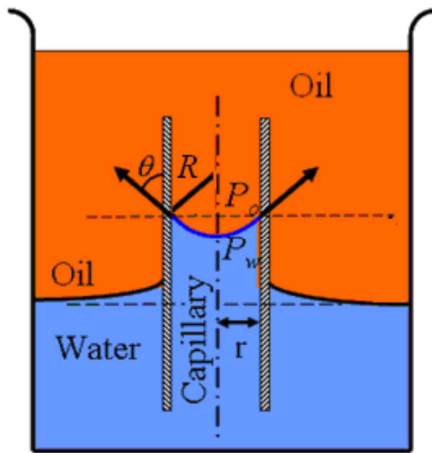


Figure 2.14 Capillary tube suppressed in water and oil [26].

The capillary surface is water-wet, so the force caused by interfacial tension forces the water to rise in the capillary tube. The interface of two immiscible fluids in a narrow cylindrical channel will normally be curved in the form of a meniscus. The curvature of a meniscus surface can be characterized by two radii, and its interface will always be convex towards the wetting fluid, whose internal pressure is greater.

The relationship between the capillary pressure and the curvature of the interface is given by the Young-Laplace equation [26]:

$$P_c = \sigma \left(\frac{1}{R_1} + \frac{1}{R_2} \right) \quad \text{Equation 2.19}$$

where $R_{1,2}$ are the two principal radii of curvature. If the meniscus is spherical, the two radii become equal ($R_1 = R_2 = R$). Following it is possible to write the latter equation as:

$$P_c = \frac{2\sigma}{R} \quad \text{Equation 2.20}$$

R can be described by the pore radius and contact angle, $R = r / \cos \theta$ (Figure 2.14). In this case, the former equation become a function of the pore radius and contact angle:

$$P_c = \Delta P = P_o - P_w = \frac{2\sigma_{ow} \cdot \cos \theta_{ow}}{r} \quad \text{Equation 2.21}$$

where P_o , P_w and P_c is the oil, water and capillary pressure, σ_{ow} is the interfacial tension between oil and water, θ_{ow} is the contact angle between oil and water and r is the radius of the capillary. The capillary pressure is the result of interfacial tension and pore wall wettability, and it is inversely proportional to pore radius. Therefore, P_c depends strongly upon the reservoir pore size distribution and is very sensitive to rock heterogeneity.

As proven above, P_c is the molecular pressure difference between the wetting and non-wetting fluid:

$$P_c = P_{nw} - P_w \quad \text{Equation 2.22}$$

where P_{nw} is the pressure to the non-wetting fluid and P_w is the pressure to the wetting fluid.

2.3 Sandstone rock sample

Sandstone is a common reservoir rock and a large percentage of the world's petroleum reserves are located in sandstone reservoirs. Sandstone is a sedimentary rock originating from breakdown of pre-existing rocks by weathering and erosion. The sand and sediments that form sandstone reservoirs tends to be carried long distances by rivers and currents before settling in sites such as deltas and beaches. Loose sediments are buried, compacted by the overburden pressure and bound together by the process of cementation. Grains are rounded by transport and sorted in size by depositional environment. Generally grains in sandstones are relatively well rounded, ranging in size from 1/16 mm to 2 mm [32].

Sandstone is much more homogeneous than carbonate rock. However, all sedimentary rocks are heterogeneous materials, meaning they have variations in their properties. The extent of heterogeneity varies for different types of rock. Regardless of rock type, heterogeneity is highly dependent on scale. A rock with elements of heterogeneity on micro scale might have fairly homogeneous properties on macro scale. Scale dependency of rock properties is very important when performing research, and essential in making a reservoir model.

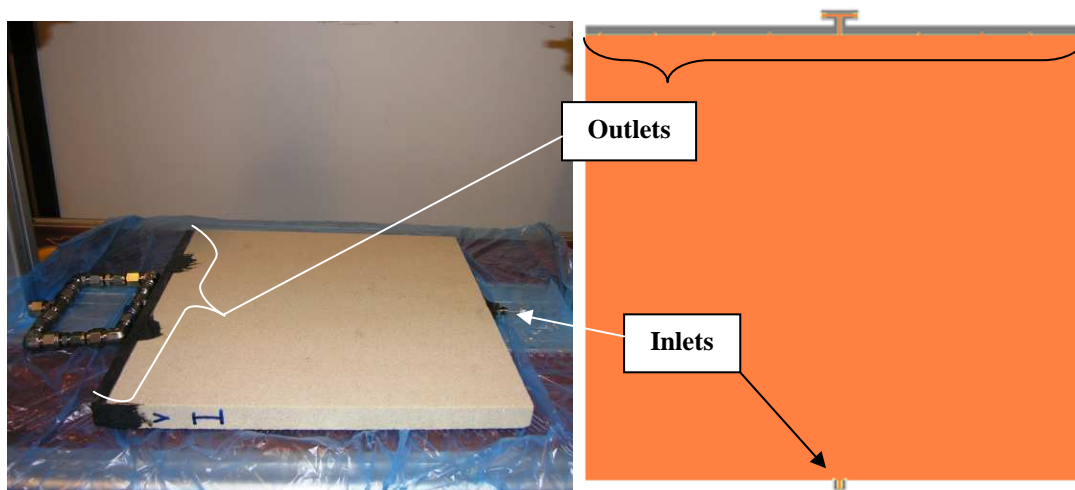


Figure 2.15 Left: Slab of Bentheimer sandstone used in this master thesis. Right: A model of the sample with inlet attached in the bottom and dispersion rail on top. Dimensions of the samples are approximately 30 x 30 x 2 cm.

The sandstone used in the experiments in this thesis is Bentheimer sandstone (*Figure 2.15*), which originates from a quarry in Germany. Bentheimer sandstone is quartz-rich, fine grained, rounded, well sorted and can be treated as a fairly homogeneous isotropic medium [33].

The porosity is in the area of $22 \pm 1\%$ and the permeability around 2.5 ± 0.5 D, i.e. relatively high-permeable. Bentheimer sandstone has overall good reservoir qualities and is very suitable for testing higher pressure without fracturing. However, for this thesis the epoxy coating limits high pressures (~ 2 bars).

2.4 Polymers

There are basically two types of polymers which are used in EOR applications, synthetic and biopolymers. The main type of synthetic polymers is Hydrolysed Polyacrylamide (HPAM) and for biopolymers, Xanthan is mostly applied.

Xanthan is produced in fermentation process by polymerisation of saccharide molecules. The structure is helical and rod-like and gives high yield of viscosity in water. Though Xanthan is quite tolerant in terms of salinity, it is susceptible to bacterial attacks. To prevent bacteria from degrading the polymer, biocides are added. Biocide is intended to kill living organisms and is harmful to the environment. In terms of price, Xanthan is more expensive than HPAM per unit amount, but when compared on a unit amount mobility reduction, particularly at high salinities, the costs are not so different.

HPAM is relatively resistant to bacterial attack and quite inexpensive, but is largely sensitive to brine salinity. Both classes of polymers tend to chemically degrade at elevated temperatures and shear rates [1]. In terms of fluid rheology, both Xanthan and HPAM changes from Newtonian to shear thinning behaviour with increasing flow rates. Over a certain point, HPAM exhibit elastic properties at high flow rates (*Figure 2.19*). Due to the bacterial aspect where biocide is added to protect Xanthan, HPAM is considered to be the most reliable and manageable polymer.

The type of polymer used in this thesis is HPAM. It is by far the most used type of polymer in oil recovery processes [1], due to its availability, price and environmental advantages compared to Xanthan. This was the main arguments for applying HPAM during a polymer injection at an offshore field [34]. Although HPAM had been used in other industries, it was the pioneering studies performed by several authors [35-38] in the 1960's which established this polymer as a potential mobility control agent in improving water injection.

2.4.1 HPAM structure

HPAM is a synthetic straight-chain polymer of acrylamide monomers, some which have been hydrolysed, as shown in *Figure 2.16*.

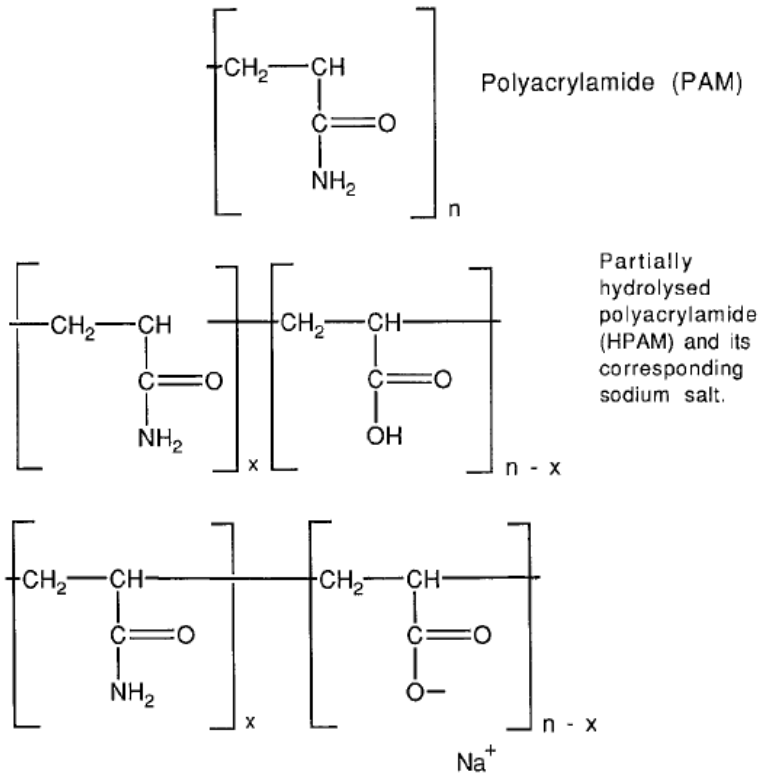


Figure 2.16 The primary chain structure of polyacrylamide (PAM) and partially hydrolysed polyacrylamide (HPAM) [1].

The HPAM molecule is a flexible chain structure sometimes known as a random coil in polymer chemistry. It is a polyelectrolyte, and will interact quite strongly with ions in solution. The effect the ionic strength has on the hydrodynamic size of the molecule is shown in *Figure 2.17*.

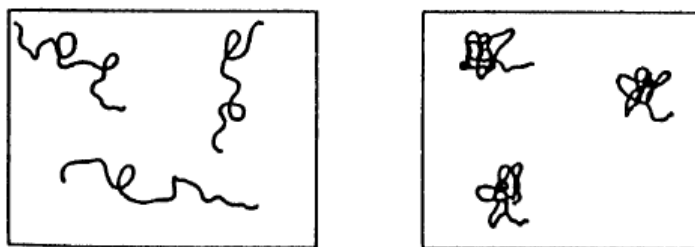


Figure 2.17 The effect of solution ionic strength on the conformation of flexible coil polyelectrolytes such as HPAM. Salinity is increased from left to right [1].

2.4.2 Rheology

Rheology is the study of flow of matter, primarily in liquid state, in response to an applied force [39]. Viscosity is a measure of a fluids resistance to deform when under the influence of an external force. It is not a fixed value, and it depends on the fluids nature, temperature and the amount of force applied. The viscosity is defined as the ratio between shear stress to shear rate:

$$\mu = \frac{\tau}{\dot{\gamma}} \quad \text{Equation 2.23}$$

where μ is the viscosity, τ is the shear stress and $\dot{\gamma}$ is the shear rate. The different parameters are illustrated in *Figure 2.18*.

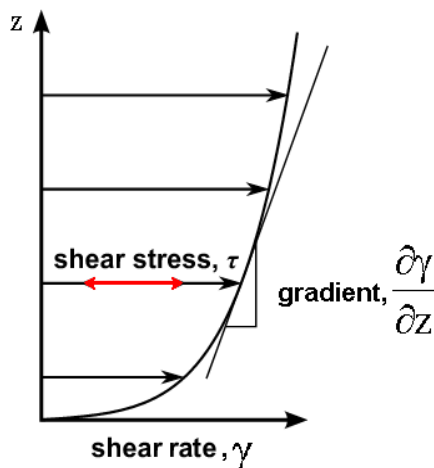


Figure 2.18 Modified figure of laminar shear flow [40].

Fluids can be divided into several classes based on their behaviour compared to the shear rate applied. A flow curve is a function of shear rate to shear stress, and can be used to determine which class a certain fluid belongs to. For Newtonian fluids the viscosity is independent of the shear rate, i.e. the viscosity is constant. A typical example of a Newtonian fluid is water. The majority of fluids are non-Newtonian. HPAM solutions are known to exhibit non-Newtonian behaviour during shear flow. This means that the viscosity is dependent upon shear rate [1]. *Figure 2.19* shows a typical flow curve for a dilute polymer solution with four distinct regions.

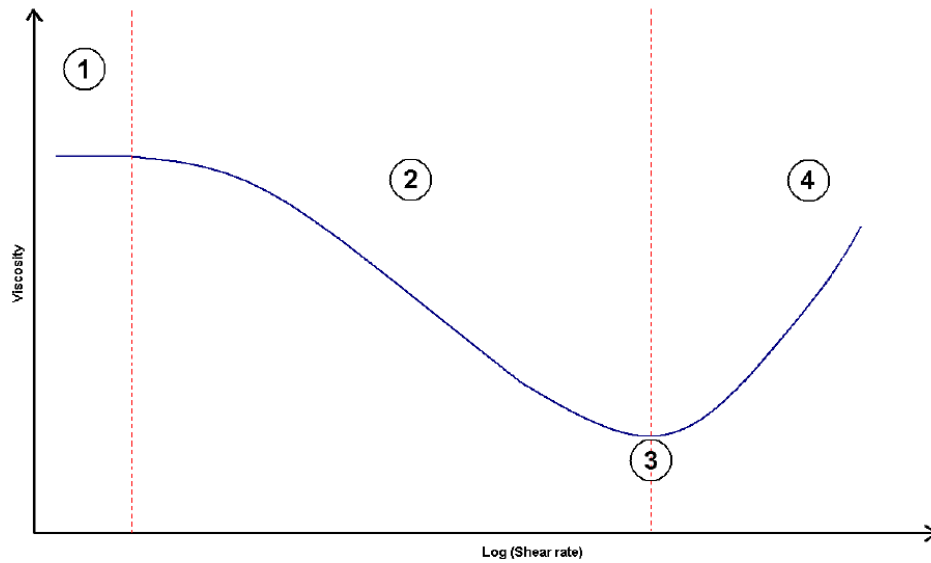


Figure 2.19 Schematic viscosity curve of a polymer solution as a function of shear rate where each number represents a specific region [41].

- 1) **Newtonian region:** Viscosity is constant, i.e. independent of the shear rate. This behaviour can be interpreted as the shear forces are not high enough to break the equilibrium structure of polymer molecules in the solution.
- 2) **Shear thinning region:** The viscosity decreases with increasing shear rate. Above a certain shear rate, the shear forces start to break up the equilibrium structure and un-coils the molecules, resulting in a reduced number of associations between the polymer molecules [42]. This results in a decreased viscosity as more molecules are un-coiled and aligned with the flow direction.
- 3) **Bottom point of shear thinning region:** The viscosity is at its lowest as the polymer molecules are at their most aligned conformation.
- 4) **Shear thickening/dilatant region:** Viscosity increase with increasing shear rate. This behaviour can be interpreted as elastic stretching and the following relaxation of the already aligned polymer molecules. This phenomenon is also known as the viscoelastic effect.

For a polymer flood the ideal scenario would be shear rates around region 3 in the near-injection area (i.e. good injectivity), and shear rates in the left part of region 2 during transport through the reservoir, as the flow rate decline away from the injector.

2.4.3 Retention

This study has focused on oil mobilisation at adverse mobility ratio, and polymer retention has not been measured. The present thesis aims to investigate the mechanisms behind the increased recovery. However, in the real world, economy is always essential for the implementation of a project. Retention is an important issue regarding the economics of a successful polymer flooding. Therefore a small introduction to the term retention is necessary to understand which variables influence retention.

When polymers are added to a displacing fluid, the objective is to increase its viscosity. However, there may be significant interactions between the transported polymer molecules and the porous medium. Such interactions will cause the polymer to be retained. Polymers experience retention in porous media due to adsorption onto solid surfaces or trapping within small pores [14].

Polymer retention varies with polymer type, molecular weight, rock composition, brine salinity, flow rate and temperature. Field-measured values of retention range from 7 to 150 μg polymer/ cm^3 of bulk volume, with a desirable value being less than about 20 $\mu\text{g}/\text{cm}^3$ [18]. Retention causes loss of polymer from solution and leads to a delay in the rate of the polymer and generated oil bank propagation. D_p is called the *frontal advance loss* and corresponds to the polymer slug size needed to satisfy the retention:

$$D_p = \frac{V_{\text{pol}}}{V_p} = \frac{A_{\text{pol}} \times \rho_s \times (1 - \phi)}{\phi \times C_{\text{pol}}} \quad \text{Equation 2.24}$$

where V_{pol} is the volume of polymer solution, V_p is the pore volume, A_p is the adsorption of the polymer, ρ_s is the solid density, ϕ is the porosity and C_{pol} is the polymer concentration in solution. D_p is useful as it expresses the retention in pore volume units which are consistent with slug size. In order to estimate the slug size needed in a practical field case application, the following formula has been suggested:

$$D_p^* = 1.3 \cdot E_{\text{vol}} \cdot D_p \quad \text{Equation 2.25}$$

where D_p^* is the practical frontal advance loss and E_{vol} is the volumetric sweep efficiency. As a rule of thumb, D_p has been increased by 30% in order to prevent breakdown of the polymer slug before breakthrough [18]. If the slug is followed by chase water, fingering may cause instability in the zone between water and polymer solution. E_{vol} is included in the formula since polymer can be retained only in the regions swept by the polymer slug.

2.4.4 Inaccessible pore volume and depleted layer

Inaccessible pore volume (IPV), originally reported in 1972 [43], consider the volume flooded by polymers in porous media. Due to the size of polymer molecules, the smaller portions of the pore volume will not be invaded by the polymer solution [1]. This forces the polymer front to advance through the porous media, hence the early breakthrough (*Figure 2.20*).

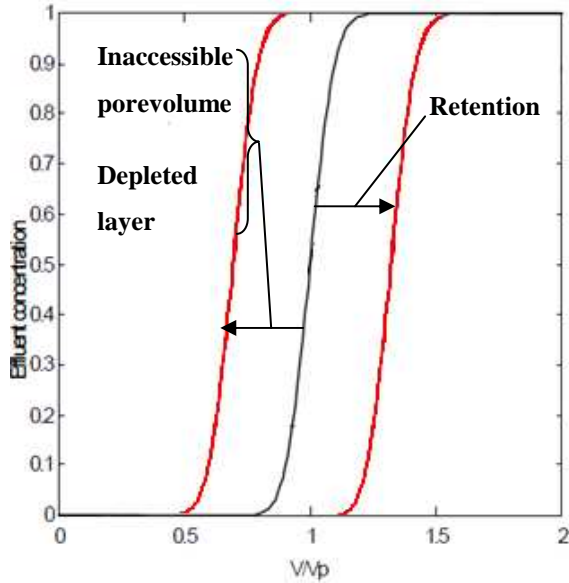


Figure 2.20 Fractional flow curve of polymer. Adsorption will decrease the front velocity, IPV and depleted layer will increase the front velocity. Modified from Moctezuma-Berthier [44].

Though IPV increase the front velocity of the polymer, retention will try to decrease the front velocity (*Figure 2.20*). Both HPAM and Xanthan may, under certain flow conditions, show depleted layer effects in their in-situ rheological behaviour during flow. Depleted layer develop because the centre of mass for a large polymer molecule is sterically unable to approach within a certain distance from pore walls.

If a layer of low-viscosity water comes between the pore wall and polymer, this presumably could lubricate flow for the polymer solution [1]. This will cause the polymer to advance through the porous media (*Figure 2.21*).

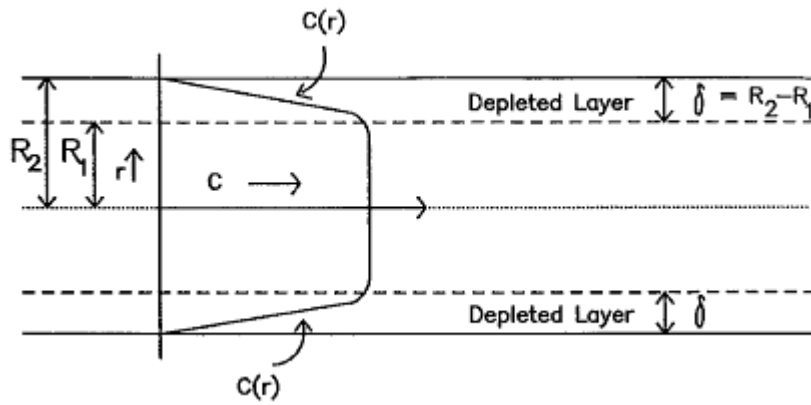


Figure 2.21 Schematic of polymer concentration profile, $C(r)$, due to depleted layer [45].

2.5 Miscible displacement

One of the earliest methods for producing additional oil is through the use of solvent injection; a displacement fluid which is miscible with the crude oil in the reservoir. This method for producing oil will not be discussed any further since it is not the case for this thesis. However, miscible displacement is important regarding characterization of a porous rock sample.

2.5.1 Diffusion

If two miscible fluids are in contact with a sharp interface, they will slowly diffuse into each other. Diffusion is the process where particles in regions with high concentration are transported to regions with low concentration through random motion, i.e. Brownian motion. The sharp interface between the two fluids will become a diffuse mixed zone from one pure fluid to another [46].

In general there are two types of diffusion which are known. Chemical diffusion is the transport of mass due to the presence of a concentration gradient, which always occurs in a non-equilibrium system. Self-diffusion is a spontaneous mixing of molecules taking place in the absence of concentration diffusion and can take place during equilibrium. The mixing caused by diffusion is described by Fick's first law [47]:

$$J = -D_0 \cdot \nabla c \quad \text{Equation 2.26}$$

where J is the flux, D_0 is the diffusion coefficient, c is the concentration of the diffusing substance.

Usually the diffusion coefficient, D_0 , is a function of mixture composition. Deriving this equation is quite complicated and data are generally lacking. However, it is often possible to get an adequate representation of the diffusive behaviour by selecting an effective average diffusion coefficient [46]. The continuity equation describes the transport of conserved mass:

$$\nabla \cdot J + \frac{\partial c}{\partial t} = 0 \quad \text{Equation 2.27}$$

where t is time.

Combining the continuity equation and Fick's first law gives Fick's second law:

$$\frac{\partial c}{\partial t} = D_0 \cdot \nabla^2 c \quad \text{Equation 2.28}$$

Fick's first law, which is also known as the diffusion equation, applies both to bulk diffusion and to diffusion in homogeneous and heterogeneous porous medium.

In a porous medium the molecules cannot diffuse freely. The molecular movements are restricted by the surrounding geometries [48]. The tortuous path which a diffusing molecule must travel in a porous medium must be accounted for if Fick's first law is to describe the diffusion.

An effective diffusion coefficient may be calculated from the equation [46, 49-51]:

$$\frac{D_e}{D_0} = \frac{1}{F \cdot \phi} \quad \text{Equation 2.29}$$

where F is the electric formation factor, D_e is the effective molecular diffusion coefficient and ϕ is the porosity. The effective molecular diffusivity D_e has been reported to be less than the molecular diffusivity D_0 [46].

2.5.2 Dispersion

When fluids flow through a porous medium, more mixing takes place in the direction of flow than from molecular diffusion alone. A convective mixing term must be added which results from flow paths caused by rock heterogeneities. Dispersion is used to describe diffusive processes which are not tied to molecular movement. It is an important transport property in displacement processes such as miscible displacements and gas injection.

The overall transport and mixing of fluids flowing through a porous medium is described by the diffusion-convection equation [52, 53]:

$$\nabla \cdot (D \cdot \nabla c) - v \cdot \nabla c = \frac{\partial c}{\partial t} \quad \text{Equation 2.30}$$

where v is the average velocity and D is the dispersion coefficient.

Dispersion in the direction of flow is called longitudinal dispersion while dispersion perpendicular to flow is called transverse dispersion. They arise from different mechanisms, and two separate coefficients are used to quantify them. Some has argued that the transverse dispersion coefficient is 24 times smaller than the longitudinal one [54].

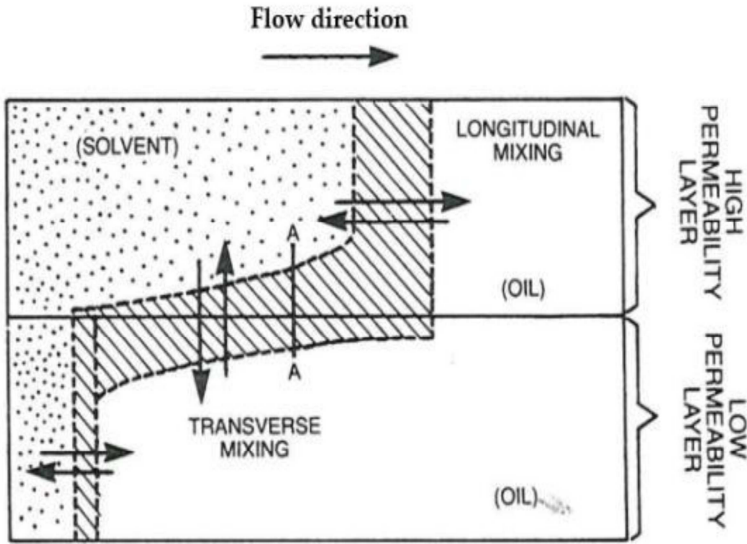


Figure 2.22 Mixing of solvent and oil by longitudinal and transverse dispersion [55].

Dispersion coefficients may be determined by experimental methods and analyses as described by several authors [46, 56, 57].

The effect of dispersion on a displacement process is often given by the Péclet number (N_{Pe}), which is given as the ratio of viscous to dispersive forces:

$$N_{Pe} = \frac{u \cdot d_p}{D} = \frac{u \cdot L}{\phi \cdot D} \tag{Equation 2.31}$$

where u is the velocity, D is the dispersion/diffusion coefficient, L is the sample length and ϕ is the porosity.

The parameter is analogue to the capillary number used in immiscible displacement. Interesting and complex behaviour occurs at high Péclet numbers (infinite Péclet number means that there is zero dispersion).

The Reynold's number (N_{Re}), also a dimensionless number, is given as the ratio of inertial to viscous forces:

$$N_{Re} = \frac{\rho \cdot u \cdot L}{\Phi \cdot \mu} \quad \text{Equation 2.32}$$

where ρ is the fluid density and μ is the viscosity.

Reynold's number is used to identify flow regimes. Laminar and turbulent flow are different with regards to flow patterns and as to which physical law that is valid. For low N_{Re} the flow is laminar and viscous forces dominate, whereas for high N_{Re} the flow is turbulent and inertial forces dominate.

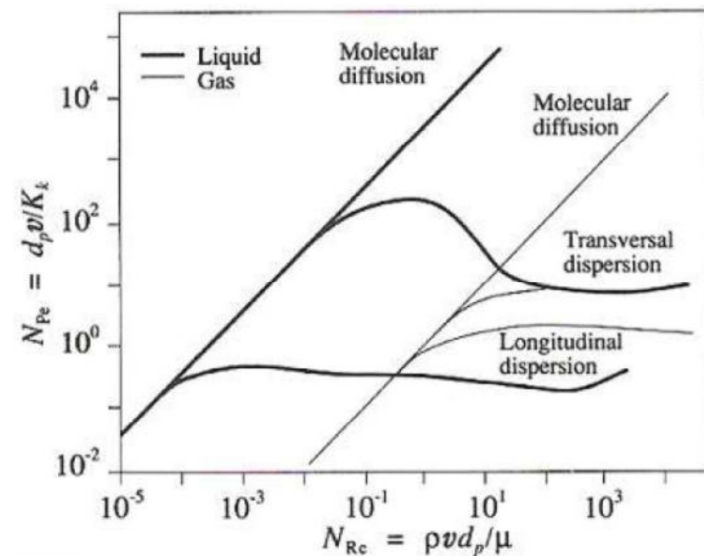


Figure 2.23 Wilhelm's illustration of longitudinal and transversal dispersion [58].

Figure 2.23 displays which forces are dominant depending on the characteristics of the flow. Transversal dispersion is more important for high values of Reynold's number and is unimportant for this thesis, because turbulent flow conditions are not likely to be encountered in a petroleum reservoir or in a rock sample at the laboratory.

Dispersion characteristics are commonly obtained by studying effluent concentration changes when tracer is injected in a miscible process. As shown that the mixing zone travels with the same speed as the injection rate [59]. This leads to the conclusion that the 50% concentration should occur at one pore volume injected tracer, if the medium is homogeneous and no

adsorption or ion exchange exist. However, for heterogeneous samples the 50% concentration is normally reached before one pore volume (*Figure 2.24*).

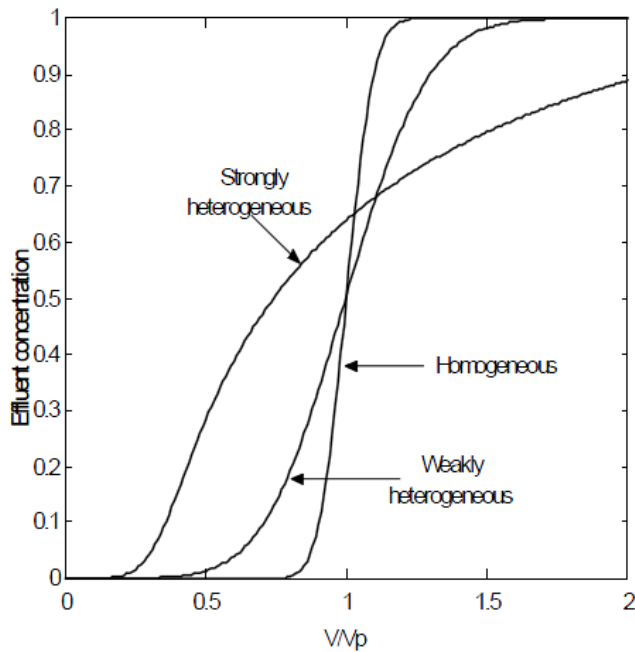


Figure 2.24 Dimensionless effluent dispersion curves are a signature of strong or weak heterogeneity [44].

Characteristics may also be affected by the sweep efficiency, as well as the distribution of dead-end pores (*Figure 2.25*). Both sweep efficiency and dead-end pores can lead to a tail production in the dispersion curve [60]. Dead-end pores, termed cul-de-sac pores [25] in geology, is pores where fluid flow is low or absent and diffusion is the only mixing agent (*Figure 2.25*).

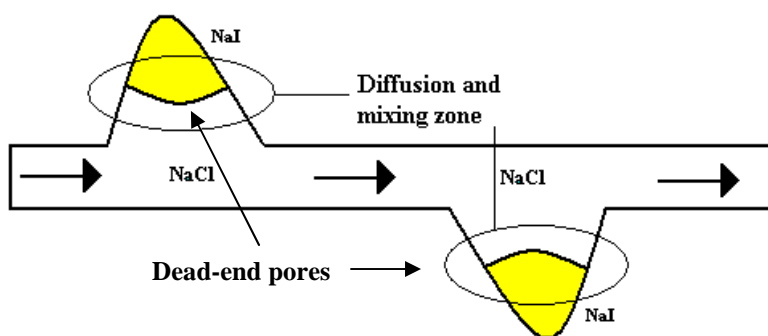


Figure 2.25 Dead-end pores and mixing during a brine-tracer miscible displacement. Tracer represents sodium iodide (NaI) and brine sodium chloride (NaCl).

In the figure above, brine displaces the tracer in the system. Due to dead-end pores, where fluid flow is lacking, diffusion is needed to totally replace the tracer. The situation of tracer-brine displacement is represented during the dispersion tests performed in this thesis. Also during a water-oil displacement, oil may be left behind in dead-end pores.

2.6 Immiscible displacement

Immiscible displacement of oil by seawater is the most common and cheapest way to maintain reservoir pressure and increase the recovery. The first immiscible displacement which happened in a petroleum reservoir though, was millions of years ago when oil migrated into it, a process called drainage.

2.6.1 Drainage

The process where a wetting fluid is being displaced by a non-wetting fluid is defined as drainage. Originally, most petroleum reservoirs are assumed water-wet and 100% saturated with water. The process where oil for the first time migrates into the reservoir and displaces the water is called primary drainage (*Figure 2.26*).

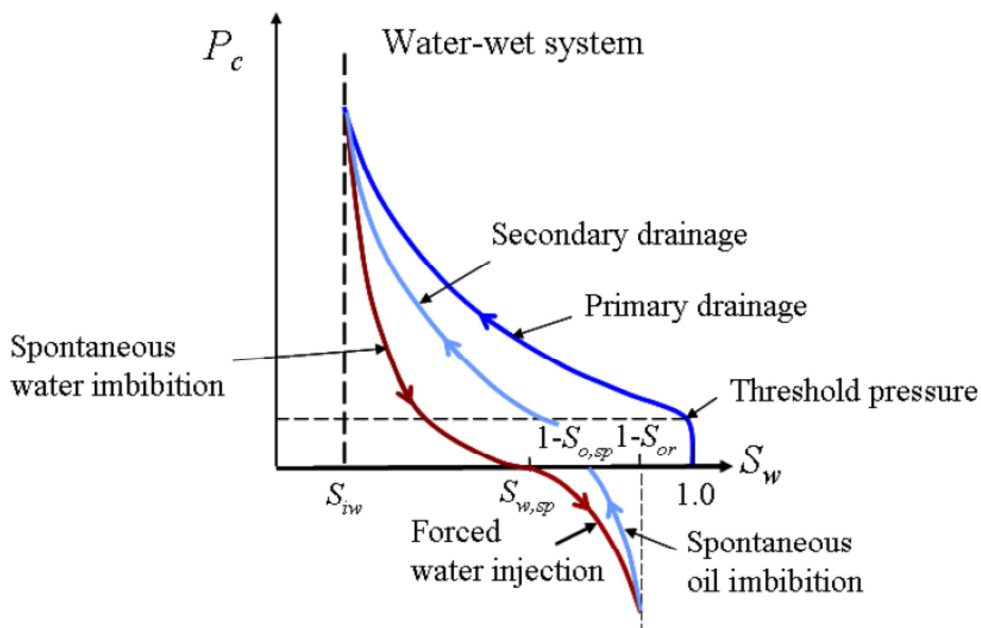


Figure 2.26 Capillary pressure curves [26].

In a porous media saturated with a wetting fluid, capillary forces prevent oil from entering spontaneously. Oil may enter the pore by applying an external pressure to the oil phase, such that the equilibrium is disrupted ($P_o - P_w > P_c$). Although a pore could be occupied by oil at a given capillary pressure, there are two reasons why the oil is prevented from invading this pore.

The first reason is that the particular pore may be inaccessible, for example if there are no neighbouring pores already filled with oil. An accessible pore is by definition connected to a previously oil invaded neighbouring pore.

The second reason is trapped water within the pore. Water is trapped in a pore if there are no continuous chains of water filled pores from the pore being filled and to the outlet of the porous medium (hydraulically disconnected). Drainage at the pore scale level can only occur through piston-like displacement (*Figure 2.27*).

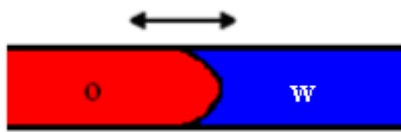


Figure 2.27 Piston-like displacement between water and oil in a pore [61].

2.6.2 Imbibition

In an imbibition process the wetting phase saturation is increasing. This occurs when the pressure difference between the non-wetting phase and the wetting phase is less than the capillary pressure ($P_{nw} - P_w < P_c$). The imbibition curve can be split into two distinct sections; one section where imbibition occurs spontaneously due to the wetting preference of the rock, and one section where imbibition must be forced by applying an external pressure (*Figure 2.26*).

Imbibition at the pore scale level can occur by piston-like displacement or snap-off. Piston-like displacement of oil by water is exactly the same as for drainage, except that the sign of the capillary entry pressure has changed.

The second displacement type, snap-off, is associated with the flow of the wetting phase through films which swell around the bulk phase (oil) in a pore. Continuous swelling of the water films forms a collar which eventually, at an appropriate pressure, causes the oil to snap-off. Isolated oil blobs left behind in this process are called residual oil since it is trapped and cannot move unless the viscous rather than capillary forces are changed (*Figure 2.28*).

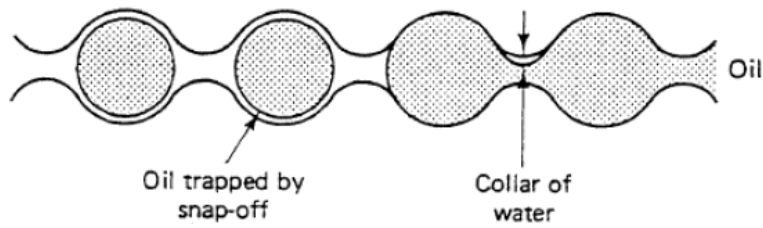


Figure 2.28 The snap-off effect [20].

The capillary pressure for snap-off is lower than for a piston-like displacement, approximately half the value. Piston displacements are preferred as long as the pore is accessible:

$$P_{c,\text{piston}} = \frac{2\sigma}{r} \geq P_{c,\text{snap-off}} = \frac{\sigma}{r} \quad \text{Equation 2.33}$$

where $P_{c,\text{piston}}$ is the capillary pressure for piston-like displacement and $P_{c,\text{snap-off}}$ is the capillary pressure for snap-off. The balance between piston like displacement and snap-off displacement depends on a range of factors such as pore size, pore geometry, connectivity of the pores and the presence of wetting films.

2.6.3 Capillary end-effect

The capillary end-effect or the holdup of a wetting phase at the outlet of a porous medium, have been studied by many authors [62-64]. A one-dimensional illustration of the end effect is shown in *Figure 2.29*.

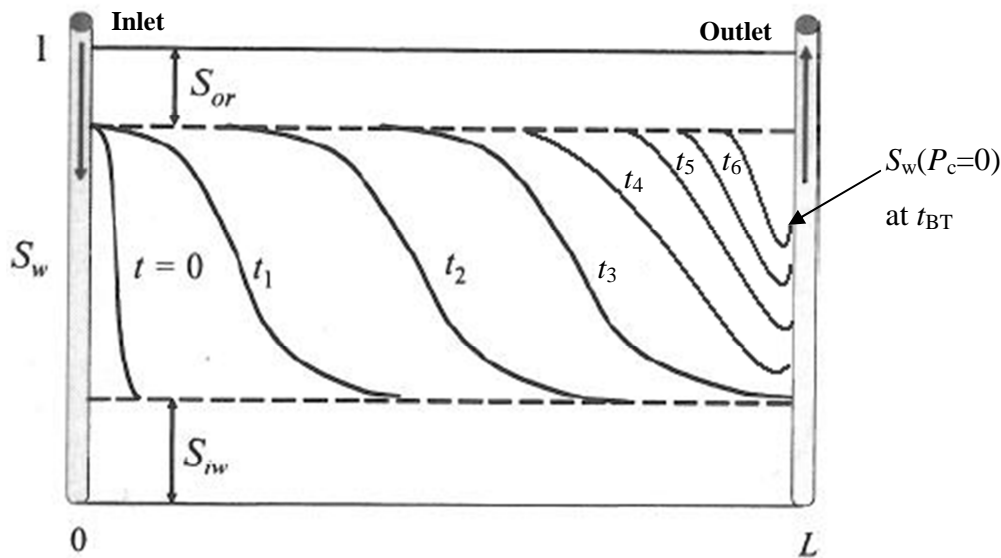


Figure 2.29 Illustration of the end effect. The front reach the outlet at (t_3), and production of water occur at $S_w(P_c=0)$ at t_{BT} . Modified from Lien [26].

The end effect occur because of the discontinuity in capillary pressure when the flowing fluids leave the porous medium and enters a region where no capillary pressure is present [64].

The discontinuity in capillary pressure makes it harder for the wetting phase than for the non-wetting phase to leave the porous media. Hence, there tends to be a build up of wetting phase at the outlet of the system (*Figure 2.29*).

A relation can be made to capillary pressure curve (*Figure 2.26*). Before the wetting fluid can flow out of the porous media and into a system with no capillarity, a certain saturation of the wetting fluid must be reached, i.e. capillary pressure reaches zero ($S_w(P_c=0)$).

2.7 Unstable displacement

The displacement of one fluid by another in a porous medium is an important aspect of reservoir engineering. The effects of gravity, viscosity, capillary pressure and heterogeneities could give frontal instabilities leading to an unstable displacement. Unstable flow is characterised by interface changes due to shift in relative forces. These forces include viscosity forces driven by adverse mobility ratio, gravity forces driven by fluid density gradients, capillary forces due to interfacial tension and dispersive forces caused by concentration gradients [65].

A typical instability phenomenon occurs in the displacement of a viscous fluid by a less viscous one, e.g. between viscous oil and water. A similar instability may occur in the vertical displacement, known as gravity segregation. Both miscible and immiscible displacements are subject to instabilities. In both cases, viscosity and density differences across the interface are the driving mechanisms of the instability. The instability phenomenon appears at many scales, but is most frequently studied through laboratory experiments [2, 66, 67].



Figure 2.30 Example of finger pattern during unstable miscible displacement at 0.1, 0.3 and 0.6 PV injected with the adverse mobility ratio, $M=11.63$ [68].

All miscible displacements with adverse viscosity ratio are inherently unstable (*Figure 2.30*). Even in homogeneous porous media instabilities will form, though reservoir rocks rarely are homogeneous. Hydrodynamic instabilities which occur on the fluids interface typically form patterns of penetrating fingers, also known as viscous fingers. The original linear instability analysis [66] considering viscous and gravitational forces and by [69] including the effects of capillary forces, established the foundation for theoretical analysis of unstable flow [70].

2.7.1 Viscous fingering

Viscous instabilities are associated with the displacement of a more viscous fluid by a less viscous one. The less viscous fluid tends to be the more mobile and can experience perturbations which finger through the system. This is known as viscous fingering or the Saffman-Taylor instability [66].

When a finger moves ahead of its average position it creates a path of low resistance which makes the more mobile fluid follow. When it has already occurred, the finger mechanism rapidly becomes dominant. Dispersive forces tend to smear out and dampen viscous fingers in miscible displacements, while capillary have the same effect on immiscible displacements.

Viscous fingering increase with an increase in mobility ratio, as shown in *Figure 2.31*. The initiation of fingers is often caused by small scale heterogeneities in the porous medium [71]. A criteria for conditions where perturbation might occur, is a mobility ratio greater than one [2]. Even though these conditions are valid for miscible displacements, other factors such as capillary pressure and relative permeability affect the initiation of fingers in immiscible displacements.

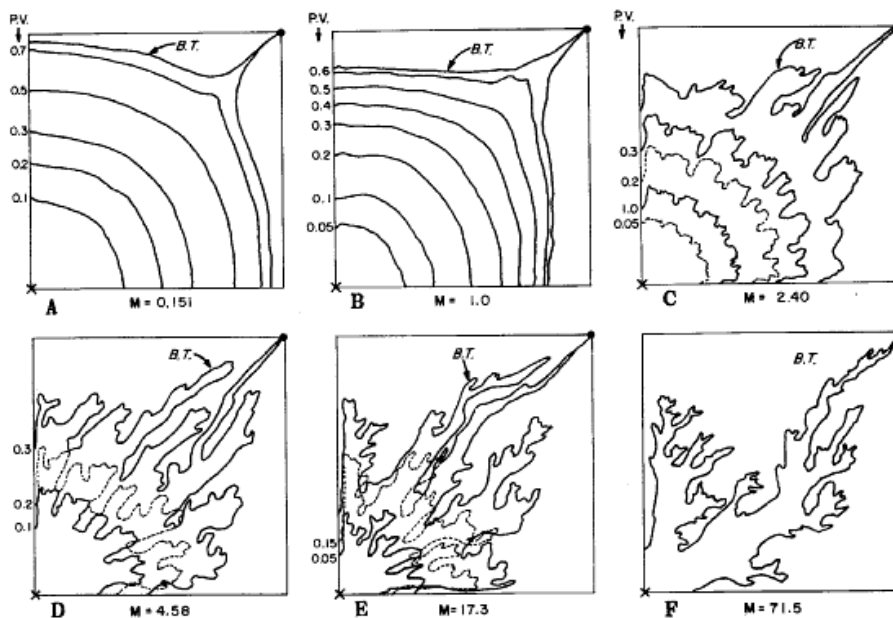


Figure 2.31 Displacement fronts for different mobility ratios and pore volumes injected in a quarter of a five-spot pattern [72].

3 Experimental

The theory and background chapters have hopefully provided the necessary knowledge to better understand the experimental approach. In this chapter, experimental methods are introduced, along with the instruments, tools and models used to interpret the results.

Two suitable rock slabs were chosen, where preparations and characterisation of both samples lasted for eight months before they unfortunately got destroyed. The epoxy detached from the rock surface during the ageing process, resulting in a by-pass area which could not be fixed.

It was discovered that the batch of epoxy had expired, with the margin of a couple of months. In combination with this fact, and that a heat curing process of the epoxy was not performed, it was concluded that these two reasons were most likely the mistakes which led to the destruction of the old samples.

The main tools used in this thesis are the two-dimensional core scanner, which provides in-situ high resolution imaging of displacement processes. The QUIZIX pump provides accurate flow control throughout the experiments, while the Rheometer by Anton Paar is used to measure the viscosity of the produced effluent.

3.1 Preparation of the porous medium

After discarding the destructed samples, two new slabs were prepared. The main intention for the first sample was to conduct a primary water injection followed by a secondary polymer flooding. As for the second sample, the main intension was a primary polymer flooding. Further on, comparisons between these two individual experiments were made (*Chapter 4.4*).

Instead of calling the samples Bentheimer 1 and 2, the experiments they are going to be exposed to will reflect the names. Bentheimer 1 is scheduled to be both injected by water and polymer, hence the name WF+PF. Bentheimer 2 is schedule to be directly polymer flooded, hence the name PF.

Table 3.1 Bentheimer sandstone slab dimensions.

Sample	Height [cm]	Width [cm]	Depth [cm]	Bulk volume [cm ³]
Bentheimer 1 – WF+PF	30.10 ± 0.05	30.10 ± 0.05	2.16 ± 0.01	1958.79 ± 0.05
Bentheimer 2 - PF	30.13 ± 0.05	30.03 ± 0.05	2.17 ± 0.01	1958.90 ± 0.05

The new samples were measured (*Table 3.1*), and kept in a heat cabinet at approximately 60 °C for a couple of days to remove any liquids.

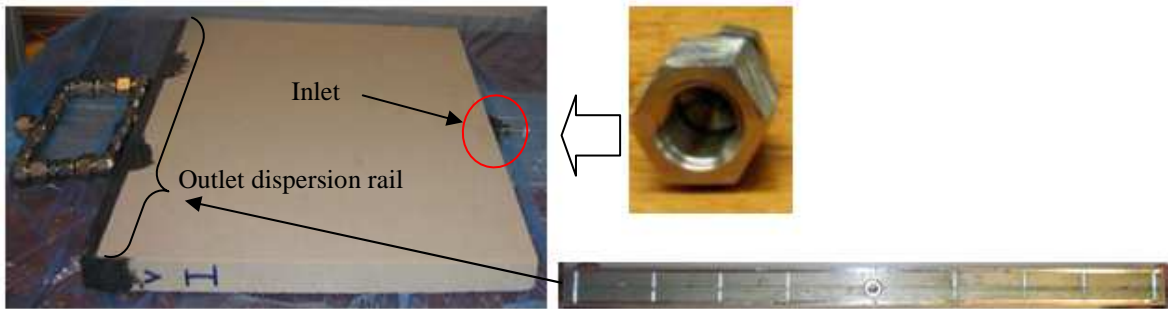


Figure 3.1 Inlet and outlet dispersion rail attached to the sample.

The next step was to find suitable inlets and outlets (*Figure 3.1*). The inlets, made by Swagelok, have a surface area of 59.45 mm². Dispensing rails distributors connected by a central port which distributes the liquid through a groove of dimensions 290 mm x 1.0 mm x 1.7 m, serve as outlet for the sample. The outlets and inlets were glued to the rock surface by epoxy applicable for metal surfaces (Axson A175/400).

After the inlets and outlets epoxy had dried for one day, the samples needed to be encapsulated in adhesive epoxy. Axson GC1 150 was used as resin and GC15 was used as hardener, with a 100 to 20 mixing ratio by weight.

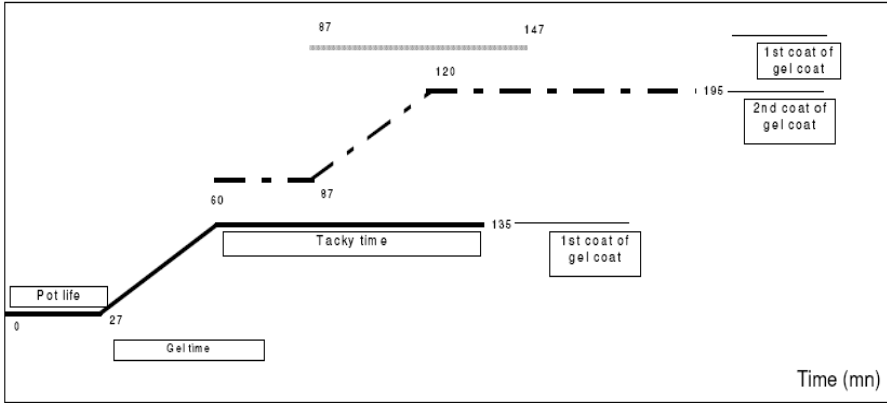


Figure 3.2 Application diagram for the epoxy gel from Axson technical datasheet.

As seen from the application diagram (*Figure 3.2*), the pot life of the epoxy mix serves as time were you have to apply the gel on the rock surface before it hardens. The gel coat is first applied on one side and then left to dry for approximately 30 minutes. The slab is turned 180°, and the first coat is applied on the other side. This is repeated on both sides within a time frame, ensuring that the first gel coat would still be in a tacky state (*Figure 3.2*), allowing a second coat to attach to the first layer.

A rack was used to keep the slabs in position when applying the epoxy and also allowing the slabs to be turned relatively easily (*Figure 3.3*).

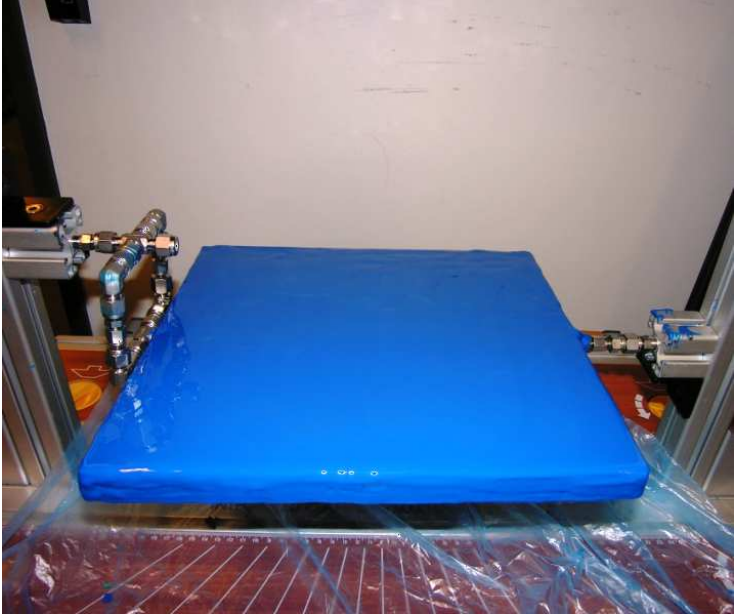


Figure 3.3 Epoxy covered slab mounted in rack.

After the epoxy had dried for one day, the sample was placed in a heat cabinet for the curing process (*Figure 3.4*). Starting at 40°C and leaving it for two hours, the process was repeated by increasing the temperature by 20°C every second hour until 100°C was reached. The process was completed by cooling the sample quickly down to 20°C again (*Figure 3.4*). This cycle would make the epoxy withstand high temperatures and make it more elastic.

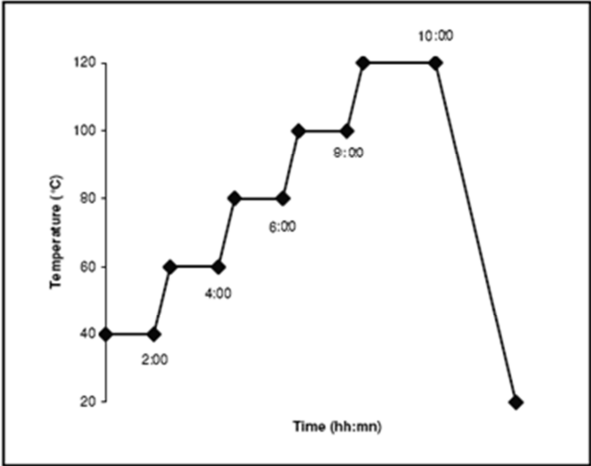


Figure 3.4 Curing cycle of the epoxy gel from Axson technical datasheet.

When the curing process was completed and the slabs had cooled down, brackets were attached on the sides on both samples with the Axson A175/400 epoxy.

Before conducting any experiments, the epoxy coated slabs were pressure tested with nitrogen at 2.5 bars to uncover possible leakages. Some leakages were found, especially around the brackets, and were patched with more epoxy. The slabs were pressure tested, once again, to be sure of no leakages. However, pressure limitation was not tested due to the risk of breaking the sample. Earlier experiments performed at CIPR report an injection pressure of 9.0 bars before leakage and 10.0 bars before breaking the sample [2]. To be sure that the worst case scenario would not occur one more time, a safety pressure of 5.0 bars was applied to the pump. However, pressures above 2.0 bars were never reached. Passing the pressure test, the slabs were mounted in the 2-D core scanner cabinet (*Figure 3.5*). The next step was to saturate the samples with an aqueous solution of sodium iodide (NaI).

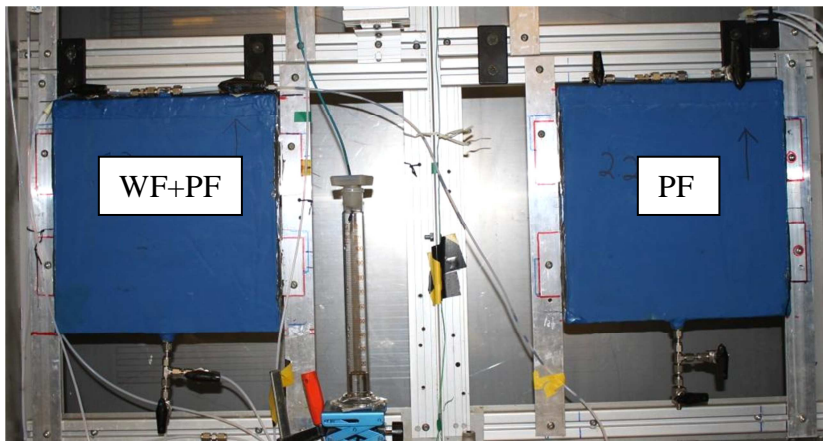


Figure 3.5 Slabs with valves and fittings mounted inside the 2-D core scanner cabinet.

3.2 Chemicals

Salts:

For preparation of saline polymer solutions and the corresponding brine solutions, sodium chloride and sodium iodide salts were applied. Properties of the salts are shown in *Table 3.2*.

Table 3.2 Properties of salt used for experimental solutions.

Type	Manufacturer	Purity [%]
Sodium Chloride	Sigma-Aldrich, Switzerland	≥99,5
Sodium Iodide	Sigma-Aldrich, Switzerland	>99

Polymer:

The polymer used in the experiments was the Flopaam partial hydrolysed polyacrylamide (HPAM) manufactured by SNF Floerger, France. The polymer was assumed to have 10% water content, i.e. a purity of 90%. The reason for applying this polymer was that it remained stable in a 10 wt% sodium iodide aqueous solution (tracer), used to saturate the samples in this experiment. All applied chemicals were used as received and the properties of the polymer are shown in *Table 3.3*.

Table 3.3 Properties of FLOPAAM HPAM polymer.

Product name	Appr.Molecular weight [MDa]	Hydrolysis degree [mole %]
3630S	20	25-30

3.3 Fluids

The salts were used to make their corresponding aqueous solutions (*Table 3.4*) for injection into the samples. Tracer is the synonym for sodium iodide (NaI), whereas brine is the synonym for sodium chloride (NaCl) in aqueous solution. Tracer is the fluid which attenuates X-rays most efficiently and therefore appears as dark-grey on the images. It was tested with different concentrations (3 and 5% by weight), but eventually 10% was found as the best option. The high salinity proposed problems with regards to the polymer solution, but it was tested out and found satisfactory for tracer (NaI). In order to avoid density differences, the brine had the same amount of NaCl salt (% by weight). The tracer and brine was made in 5 kg batches and stored in 5 L bottles at room temperature. A viscosity measurement is performed to identify differences between tracer and brine and the results can be seen in *Table 3.4*. The viscosity measurement procedure is described more in detail under *Chapter 3.6.5*.

The most common way to trace fluids in a water-oil system is to dope the oil with iododecane to be able to see the difference on X-ray images. In this thesis the resident water was doped with sodium iodide because there was lack of heavy oil, and the less viscous Heidrun oil had to be applied. The viscosity of the oil at 22°C was approximately 53 cP, and if it had been mixed with iododecane it would have been even less viscous and less fingering effect would probably appear. The Heidrun oil was put in flasks in a heat cabinet at 80°C for a couple of days to remove the lightest parts of the crude oil. This was done in order to avoid vaporizing of the crude during the ageing process.

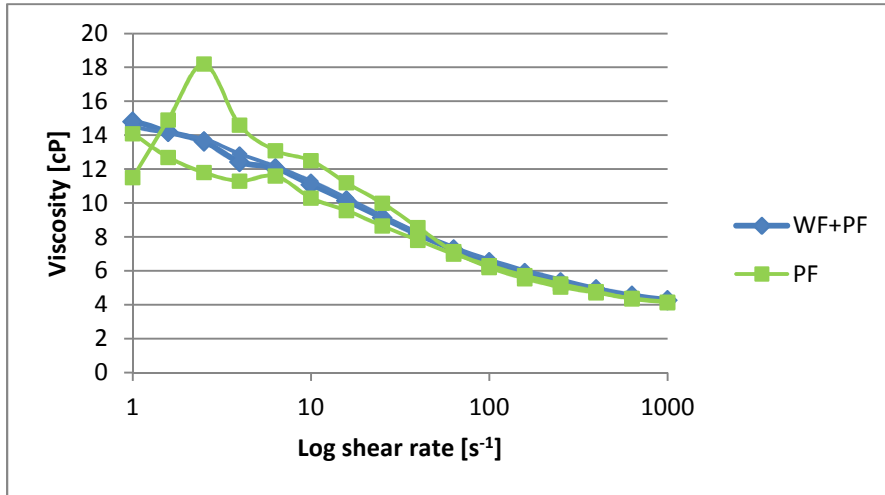


Figure 3.6 Viscosity for the WF+PF and PF polymer solutions at different shear rates.

Viscosity measurements of the polymer solutions show a decreasing viscosity as a function of increased shear rate (*Figure 3.6*), which is expected. The viscosities at 10 s^{-1} and 100 s^{-1} are shown in *Table 3.4*.

Table 3.4 Fluid properties.

Substance	Density [g/cm ³]	Salt [% by weight]	Viscosity at 10 s^{-1} [cP]	Viscosity at 100 s^{-1} [cP]
Brine (NaCl)	1.065	10	1.2 ± 0.2	1.2 ± 0.2
Tracer (NaI)	1.073	10	1.0 ± 0.2	1.0 ± 0.2
Heidrun Oil	< 1	-	53 ± 1.0	53 ± 1.0
WF+PF polymer	-	10	11.4 ± 0.2	6.6 ± 0.2
PF polymer	-	10	11.2 ± 1.6	6.3 ± 0.2

For reference viscosity measurements on the Rheometer, a polydimethylsiloxane solution manufactured by Sigma-Aldrich was applied. Note that the viscosity provided by the manufacturer is the kinematic viscosity (*Table 3.5*).

Table 3.5 Properties of reference fluid for viscosity measurements.

Type	Manufacturer	Viscosity [cSt]
PDMS200	Sigma-Aldrich, Switzerland	5 (25 °C)

3.4 2-D core scanner

The main tool for the experiments conducted in this thesis is the two-dimensional core scanner build by InnospeXion in Denmark, which allows for high resolution in-situ X-ray imaging and photon counting scan of epoxy coated rock slabs. The shielding scanner cabinet is suspended on a steel frame with two sliding doors which gives easy access to the interior of the scanning system (*Figure 3.7*). An inspection window gives visual access to the cabinet interior while scanning is performed.

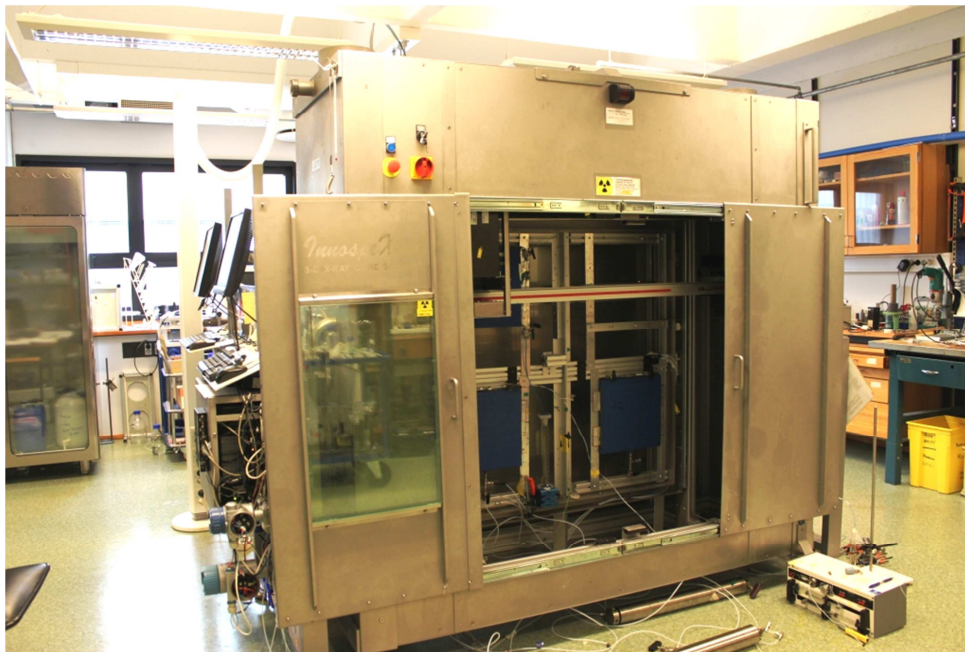


Figure 3.7 The 2-D rig placed inside the shielding cabinet made of lead. Two sliding doors provide access to the interior.

To minimize the risk of radiation outside the cabinet, a safety sensor makes it impossible to start scanning before the doors are properly closed. The entire system can be used in vertical or horizontal position, and rock samples can be mounted into a completely extractable tray while tilted to the horizontal position (*Figure 3.8*). The rig is based on quantitative attenuation and is applicable for samples up to 1 x 1 m. Two independent software programs, providing control of the scanning parameters, are used to perform photon counting scanning or X-ray image scanning. The instrumentation has numerous calibration options to tailor the system for specific flow experiments.



Figure 3.8 The rig can be tilted for horizontal flooding experiments. The shuffle provides easy access to the sample.

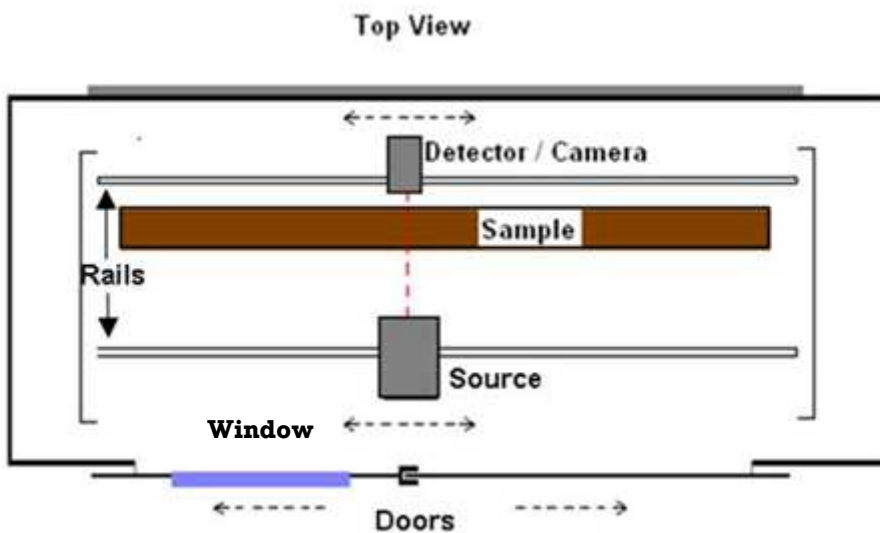


Figure 3.9 Schematic top view of the 2D rig. The source and detector/camera are moving on rails, with the sample placed in between.

The applied experimental setup is developed at CIPR, and the two-dimensional scanner is designed specifically for analysis of viscous unstable displacements for both miscible and immiscible processes [2]. The sources and detectors move simultaneously along the rails in horizontal and vertical direction, which is controlled by a computer connected to digital servomotors. Either an X-ray source or a low energy gamma-ray source is used to emit a narrow beam of electromagnetic radiation which is attenuated by a porous rock sample (Figure 3.9).

Gamma- and X-rays are distinguished by their origin. Gamma-rays are produced by radioactive gamma decay in a nucleus, while the X-rays are produced when fast moving electrons are retarded by a metal target. The interactions between electrons and target result in a conversion of kinetic energy into thermal energy and electromagnetic energy, i.e. X-rays.

The gamma source is a 7.4 GBq isotope Am^{241} (half-life = 433 years) emitting an energy of 59 keV. Am^{241} decays to Np^{237} emitting alpha particles of different energies. Because numerous of the resulting states are metastable, they emit gamma-rays with energies between 26.3 and 158.5 keV [73], but the main peak is at 59.7 keV. The X-ray source may be operated between 40 and 60 kV, at a maximum current of 0.4 mA. The ranges used in this experiment are 47 kV and 300 μA for the gamma scans, and 60 kV and 320 μA for image scans.

A NaI crystal scintillation photon counting detector and an X-ray camera measures the intensity of the attenuated beams (*Figure 3.10*). The amount of attenuation depends on the porous media and its composition together with the fluid it is saturated with. E.g. the higher the attenuations the darker the X-ray images get.

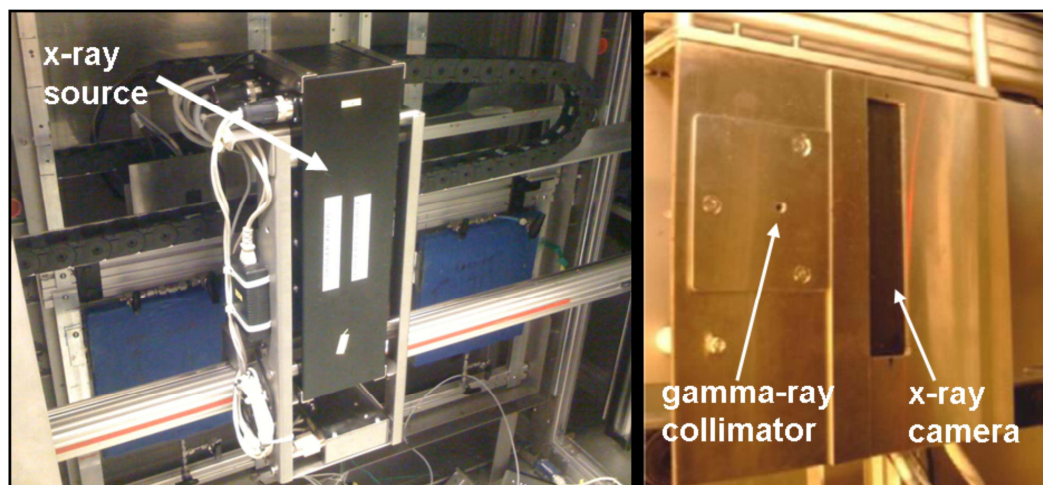


Figure 3.10 Left: X-ray source. Right: Gamma-ray collimator and X-ray camera.

The X-ray source is a Magnatek CS-60 unit with 0.3 mm x 0.5 mm focal spot and fan beam geometry and the X-ray camera is an AJAT SCAN 300F CdTe linear detector (*Figure 3.10*).

For the gamma-ray scans, a circular (5 mm diameter) detector collimator is used to filter a stream of rays so that only those travelling parallel in a specified direction are allowed through (*Figure 3.11*). The use of the collimator excludes secondary radiation caused by interactions like Compton scattering.

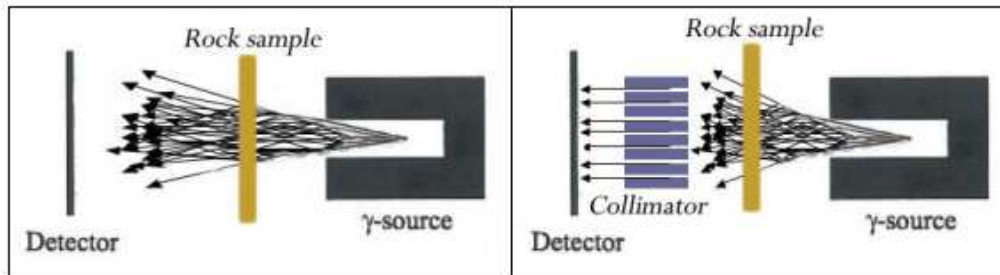


Figure 3.11 Schematic of photon counter. Left: Without collimator. Right: With collimator.

3.4.1 X-ray imaging

The X-ray camera, a linear array which moves across the sample simultaneously with the X-ray source, provides high resolution real-time imaging of miscible and immiscible displacements in porous rock samples. X-rays passing through the porous media are detected by the camera and outputted as X-rays images (*Figure 3.12*). The angle of X-ray emission used for image scan is typically 20° . The X-ray camera must be switched on some time before use and put on a warm-up sequence to reach operating temperature ($30 \pm 0.5^\circ\text{C}$). It takes about 15 minutes to stabilize the temperature.

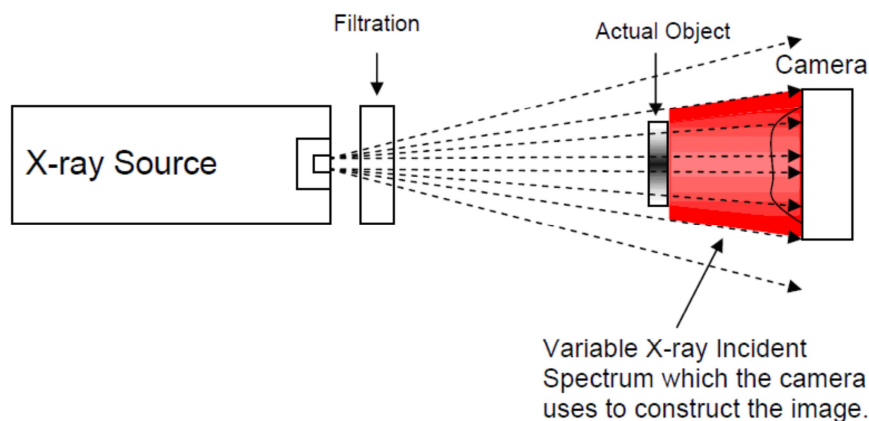


Figure 3.12 Schematic view of the X-ray camera setup.

The camera is approximately 12.5 cm tall and 6.5 mm wide and has no collimator in front. Each image strip is 64 x 1510 pixels. The strips are collated together to form the 1352 x 1510 pixels images which are stored. X-rays moves in a fan pattern towards the camera, and all rays are counted. The camera will count an area much faster than the photon detector, which makes it ideal to monitor rapid saturation changes. This technique is not as accurate as photon counting, but allows for real time attenuation images that can be correlated to actual flow patterns. Images obtained by the camera provide the shape and extent of the flowing front during a displacement. Fingering and unswept areas can be detected and observed qualitatively.

The whole 1 x 1 m available scanning area is divided into sub-areas of 9 x 9 matrix sectors, where each area can be scanned individually (*Figure 3.13*). Each sector is a square of approximately 11 x 11 cm, and the areas which are to be scanned are selected in the belonging computer software.

The images of each sector are saved on the computer hard disk during the scanning process, and the size of the 3 x 3 matrix (conducted in thesis) is approximately 60 megabytes (mb). Image resolution can be changed, but in this thesis the best resolution is used, which naturally require longer scanning speed (3 cm/s). An image scan for a 30 x 30 cm core sample require a 3 x 3 matrix (blue areas in *Figure 3.13*), and takes approximately five minutes to complete.

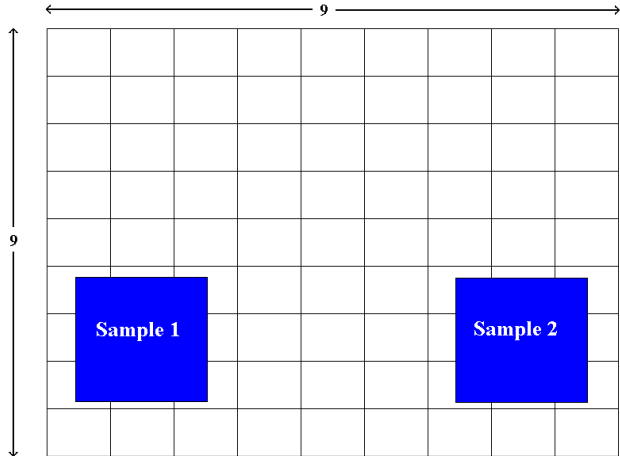


Figure 3.13 Scanning area of the 2-D core scanner.

Adsorption of radiation depends on the material it travels through. Intensity detected by the camera is a function of the porous media and the fluid it is saturated with. The different detected intensities are captured with varying grey levels ranging from black to white. To improve the contrast between fluids in oil- brine systems, one of the fluids is normally tagged.

The brine is most often tagged by iodide (i.e. tracer), which has a high level of attenuation, giving a darker grey colour of the displacing fluid on the X-ray image.

The raw data received from the X-ray camera is 16-bit unsigned data for each pixel, where each pixel has a value in the range 0-65535. A range is set by the software before each scan and the data is saved as jpg, tif and large.tif in a grey scale. The range was set from 0-3500 for all experiments, and intensities higher than 3500 is set to be white in the image. A limitation is that only a portion of the raw data is kept to save hard disk space. However, real-time saving of data would result in a rate of approximately 23 mb/sec. This would quickly occupy much storage if all data was saved.

3.4.2 Image processing

The image file stored in the computer is approximately 60 mb, and is the sum of all nine sectors scanned. Every sector has four elements, or files, which are automatically stored at the end of a scan. The four files are text, jpg, tif and large tif, where the text file contains information of threshold- and X-ray values (voltage and current). The three other files are image files, where jpg, tif and large tif are of different sizes in increasing order (*Figure 3.14*). Image sectors are put together to form a final picture, which is used in the thesis, and is performed by MATLAB. The MATLAB scripts are written especially for these tasks [55, 74].

One or more images are taken before every new flooding experiment to form an initial image. Every image taken during the flooding is retracted from the initial picture to form a difference image. It is possible to use all three types of sectors images, but the jpg format was used in this thesis.

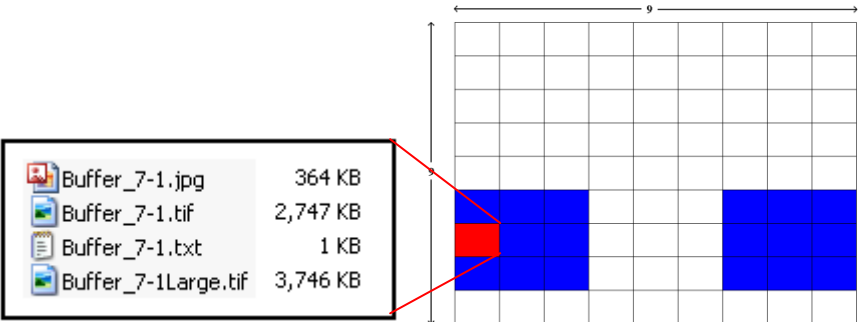


Figure 3.14 Example of type and size of the 7.1 sector file (marked in red).

A code in MATLAB is used to retract all images within a folder, e.g. all images for water injection, which is quite time saving. Mostly retracted images are used in this thesis, but original images which contain lots of noise are occasionally used.

3.4.3 Image filtration

The X-ray camera may cause noise in the original unmodified image. Images used in this thesis are mostly pictures which are retracted from one or more initial images taken before each experiment. There are mainly two reasons why retracted images are used: Firstly, the difference between the initial image and the rest of the images is useful during secondary and tertiary injections, where only the current injection is of interest. Secondly, retracting images from each other remove some noise, improving the quality of the images.

It is possible to remove more of the noise with tailor made filters in MATLAB. Such a filter has been applied to see how it can improve images. The filter code is developed by a PhD student at CIPR, and is still under construction and improvement.

Instead of jpg images, like in this thesis, large tif images are used. The original images taken by the X-ray camera has pixel intensity between 0-65000 roughly, which is reduced to range between 0-3000 because noise is normally in the higher range of the scale. The image size is reduced and retracted from the initial image and the new image is converted to a frequency domain instead of an image domain. The code looks for noise frequencies and suppresses these frequencies. A filter is applied in the end to smoothen the frequencies before the images are converted back to an image domain.

3.4.4 Sources of error

Image scans start from the top and scan each row before it moves down to the next row. The total scanning time for each rock sample for the 3 x 3 sector matrix is five minutes. A consequence of this is that more solvent is injected at lower sectors than captured on image, and displacement patterns may have changed during the scan (*Figure 3.15*).

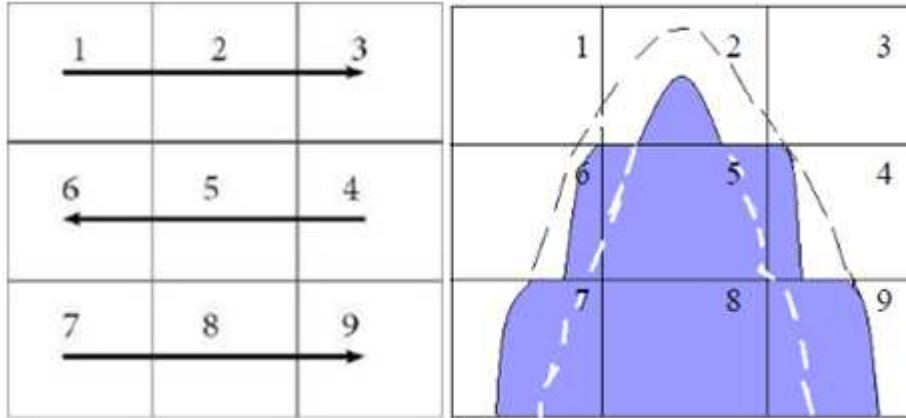


Figure 3.15 Left: Scan order of a 3 x 3 X-ray image sector matrix. Right: Exaggerated illustration of injection affected by X-ray camera delay.

The effect of possible changed patterns depends on the flow rate. Different rates are corresponds to the different types of injections and is shown in *Table 3.6*.

Table 3.6 Effects of injection rate to camera delay.

Type of injection	Rate [mL/min]	Volume injected per image [mL]	% of PV
Water and polymer	0.1	0.5	0.12
Chase water	1.0	5.0	1.16
Dispersion	2.0	10.0	2.33

Chase water injections and the effluent dispersion tests might be affected to some extent, but the standard injections of water and polymer are not so much affected. The original image file created at each scan registers the time the scan starts. When images are put together by MATLAB, this time is used to calculate the volume injected to each specific image. The X-ray camera delay may affect the calculated volume at the start of a scan, if 5 or 10 mL extra is injected during an image session, which might be 50 to 100% extra compared to the calculated volume.

The X-ray camera is 12.5 cm long, but the top and bottom of the sector images cannot be used due to noise and overlap. The overlap is fixed when the image sectors are put together by adding cutting values in the MATLAB code. Cutting values fix this by removing parts of the top and bottom of the images, resulting in a height of approximately 11 cm (Figure 3.16). From image sector 1 the rays detected above the cutting boundary is removed, and correspondingly from image sector 2 the rays detected below the cutting boundary is removed.

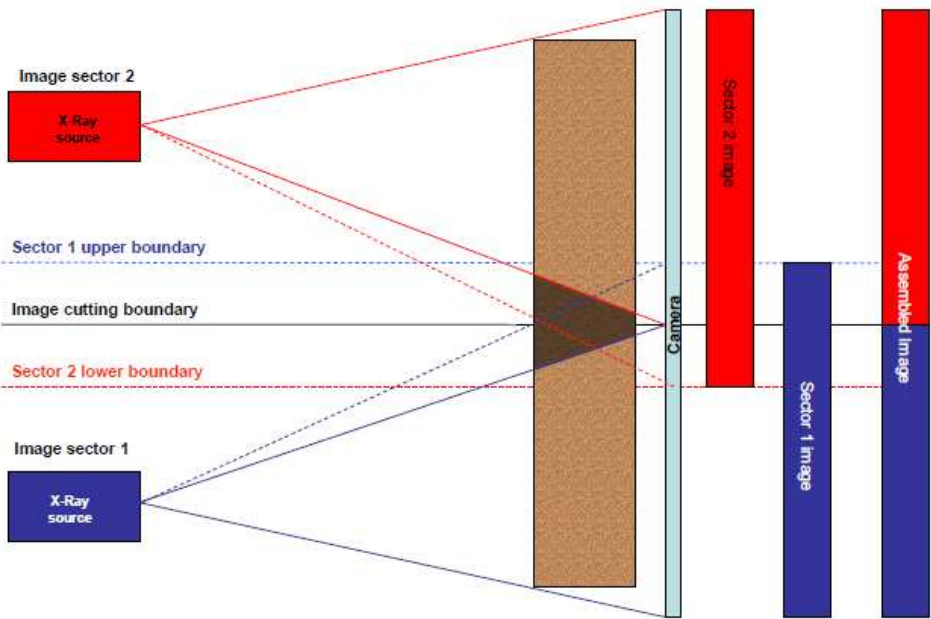


Figure 3.16 Outer boundaries of X-rays measured from two different source positions [55].

As shown in Figure 3.11, the radiation moves in a fan pattern towards the camera. Field strength of the X-ray source is weaker at the cone peripheral area than at the centre. This results in a non-uniform intensity along the camera, yielding less radiation towards the top and bottom edges of a sector than in the centre and results in a darker area on the images, i.e. higher saturation of a specific fluid. This was taken into consideration when performing image pixel counts.

3.4.5 Image quality and cutting limits

During the work of this thesis, the noise level of the images obtained by the X-ray camera had significantly increased. The water injection performed three months after the dispersion test, showed a decrease in image quality (*Figure 3.17*).

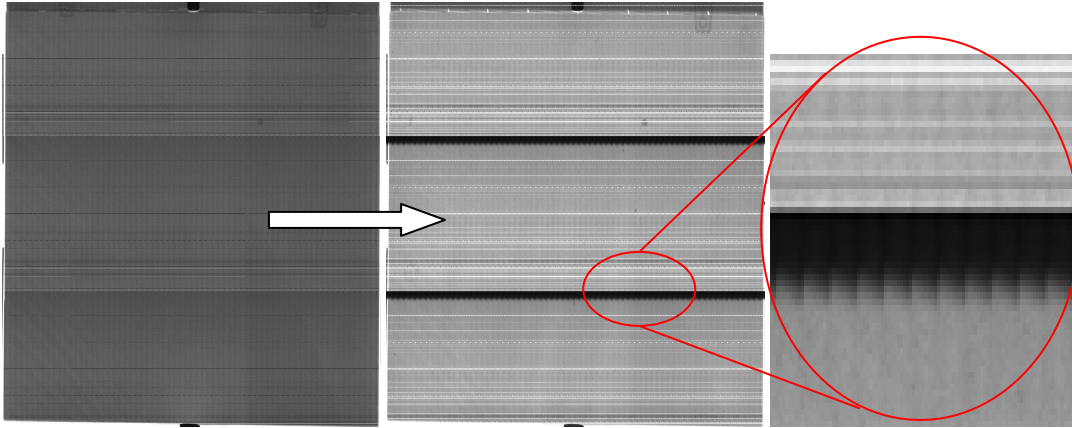


Figure 3.17 Example of decreasing image quality. Left: Initial image from effluent dispersion test. Middle: Initial image from water injection. Both images from the WF+PF sample. Right: Zoomed area of middle image.

A dark stripe is observed at the top of each row of sector images, blocking the view in certain areas of the image, leading to a reduction of information availability. The reason for the drastic change is unknown and several attempts to calibrate the X-ray camera was performed, without any improvement.

Cutting values for MATLAB was found by placing a key (*Figure 3.18*) between two image sectors and simply cutting pieces by pieces until satisfying boundaries were achieved. The exact shape of the key was however difficult to determine due to the black stripe between the images.

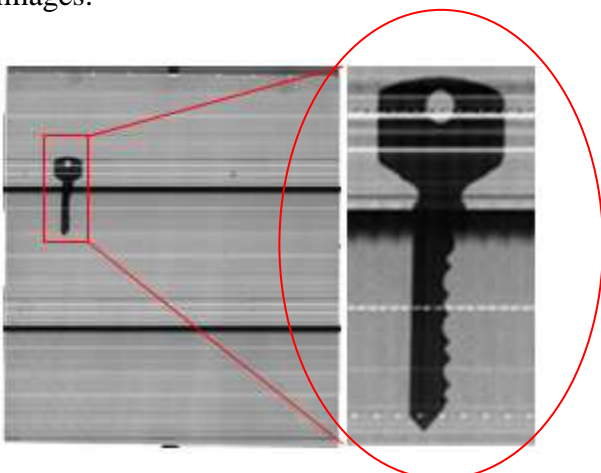


Figure 3.18 Cutting values are found by placing a key between two image sectors.

3.5 Pump and associated equipment

For every experiment involving a pump, QX-500 by QUIZIX is used. The QX-500 has many operational modes but in this experiment either constant rate or constant pressure mode is used. The pump has two 150 mL cylinders working together, assuring continuous flow. Maximum pressure is 34 bars, and the pump deliver rates of up to 500 mL/min (30.000 mL/h). Each cylinder is operated by a sprocket and a timing belt. One step on the belt displaces a volume of 0.000025 mL (25 nanoliters) and gives the outgoing rate an excellent resolution. The pump operation is controlled by a computer program, allowing recordings of cumulative volume injected. However, rate and outlet pressure are only displayed in real time and is not recorded.



Figure 3.19 Left: Quizix QX-500 pump. Right: FUJI FCX series differential pressure transmitter.

Measurement of the differential pressure over the rock samples have been carried out by FUJI FCX-Series differential pressure transmitter (DPT). There are two available DPTs to the core scanner, named dP-high with the range over 1000mbar and DP-Low with the range under 1000 mbar. Since the experiments in the present thesis will operate with pressures from 0-400 mbar, the dP-low DPT was chosen. The uncertainty is stated by the manufacturer to be $\pm 0.04\%$ of the measured value. It was calibrated before every experiment to ensure low uncertainty.

A problem occurred during the experiments, where the software stopped logging the pressure. This problem happened especially during night time, or in periods where the computer had been left unused, and resulted in no pressure monitoring.

3.5.1 Valves, fittings and tubing

The tubing setup is constructed of Swagelok 1/8" stainless steel valves, fittings and perfluoroalkoxy (PFA) tubing. To avoid any oxidizing iron ions in the system, all components should ideally be non-steel. However, this is a question of availability and practicality as the total flow through steel is minimal compared to that of through PFA. The PFA tubing is also very convenient when removing air from the system, since its transparency reveals air bubbles easily.

3.5.2 Piston and measuring cylinders

Piston cylinders were mounted in the circuit between the pump and the rock slabs. Two chambers are separated by a piston in a stainless cylinder, with valves at the in-and outlet (*Figure 3.20*). The piston assures no contact between the fluids as well as an output rate equal to the pump rate. The main reason for using piston cylinders is that the injection fluid can easily be switched between brine, oil or polymer without having to clean the cylinders inside the pump. Another important reason is that brine with high concentration of salt may cause corrosion of the pump components. For all experiments 1.0 L piston cylinders are used, which should be cleaned and dried as soon as possible after use to avoid oxidation.

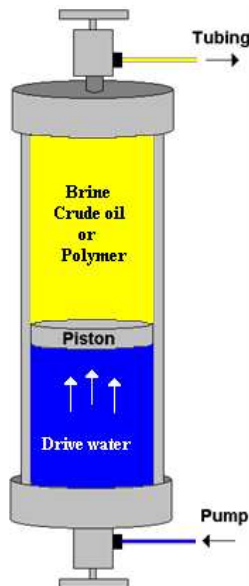


Figure 3.20 Piston cylinder used in all flooding experiments.

Note that piston cylinders which have been exposed to pressures above 1.0 bar must be handled with care. The pressurised air system used during this thesis holds 5.0 bars, and is used to push the piston in the cylinder back to the start position when emptied. Before unscrewing the outlet (tubing end) to refill the cylinder, it must be confirmed that the cylinder has been emptied for the pressurised air. This can be done by opening the valve at the end and letting the air out. A piece of paper towel is put in front of the outlet opening to catch any fluids that may be sprayed out due to the pressure. If the cylinder is not de-pressurised before unscrewing the outlet, it may pop off as a projectile and cause injuries to people and equipment.

Measuring cylinders are used to collect the effluent from the flooding experiments (*Figure 3.21*).



Figure 3.21 100 mL measuring cylinder from Brand Eterna, Germany.

Table 3.7 Different measuring cylinders used in experiments.

Measuring cylinders [mL]
250 ± 1.50
100 ± 0.80
50 ± 0.75
25 ± 0.38
10 ± 0.15

3.6 Procedures

The different procedures during the experimental work are described in this section.

3.6.1 Porosity and permeability measurements

Porosity:

The samples were first evacuated down to approximately 5 mbar by a vacuum pump (Figure 3.22). The amount of air left in the sample after evacuating it, corresponds to less than 1% of the total pore volume when the sample is returned to atmospheric pressure. An aqueous solution of sodium iodide was pumped into the sample until a preset pressure was reached.

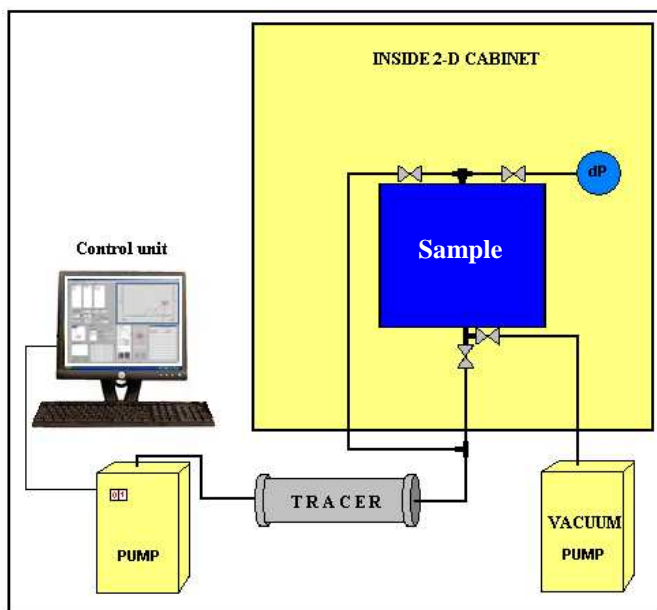


Figure 3.22 Setup for porosity measurement.

The pump was put in constant pressure delivery mode, with a constant pressure of 2.0 bars. This function enables the pump to adjust the rate automatically. The max rate is set to 50 mL/min which is reduced to 10 mL/min when the pressure reaches 1.0 bar. This is done to reduce the shocks that may occur when rates shift rapidly from 0 to 50 mL/min. The porosity calculation is based on the amount of liquid which is used to saturate the core with respect to the bulk volume of the whole sample, measured by the pump. Because it is impossible to saturate closed pores, the porosity calculated will be the effective porosity. Due to the difficulty of moving the samples out of the 2-D core scanner cabinet, which could also change the position, the comparison of weighing the samples before and after is not performed.

Permeability:

Tracer is pumped through the sample and the differential pressure is measured for the different rates (Figure 3.23), which is quite linear (Figure 3.24). The permeability is calculated by the use of Darcy's law. Due to the different inlet and outlet areas, two methods are used to calculate the permeability.

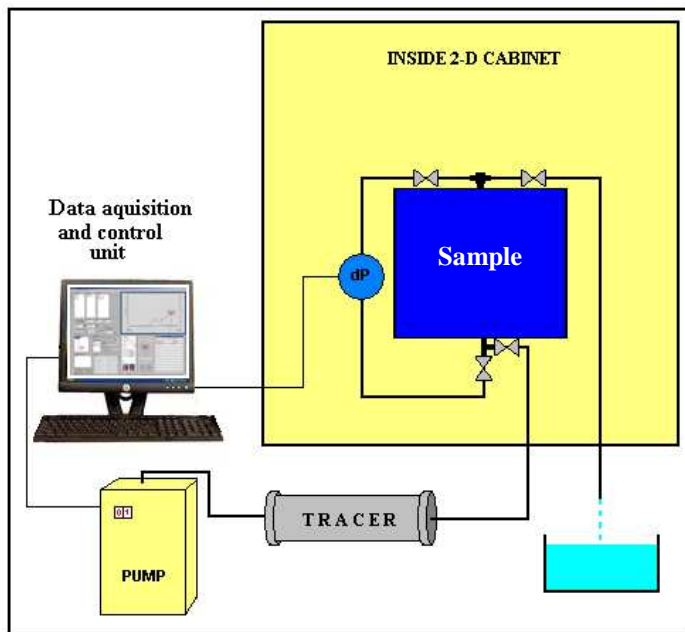


Figure 3.23 Setup for permeability measurement.

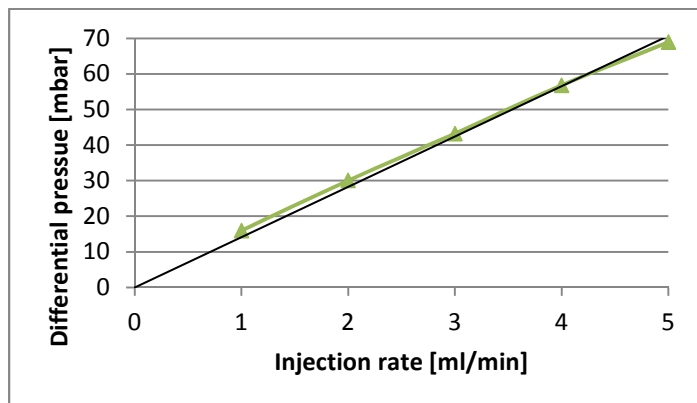


Figure 3.24 Example of differential pressure as a function of injection rate.

Method 1: Assume equal area at inlet and outlet, $A=60 \text{ cm}^2$.

Method 2: Assume radial flow:

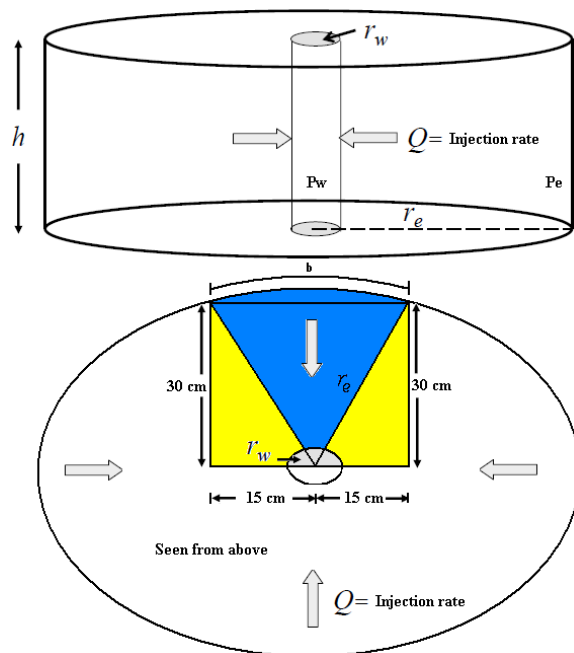


Figure 3.25 Radial flow model in cross sectional view and from above.

Assuming the flow is radial in a sector (blue part of *Figure 3.25*) of a circle the permeability can be calculated. Unknown parameters like the radius, r_e , arc length of the blue sector, b , and the angle of the blue sector has to be calculated. From the dispersion experiment (*Figure 3.26*) when brine displaces tracer, it seems as if brine has a coning behaviour towards the producer.

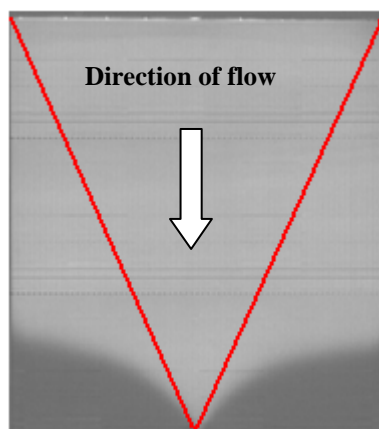


Figure 3.26 Image of brine displacing tracer from *Figure 4.5* at 0.85 PV.

Ideally the shape should be more like the blue area of *Figure 3.25*.

Pore volume injected (PV) is calculated by the following formula:

$$PV = \frac{Q \cdot t}{V_p} \quad \text{Equation 3.1}$$

where Q is the flow rate, t is time and V_p is the samples pore volume.

3.6.2 Effluent dispersion test

Previous tracer effluent tests have been performed using UV spectrometry after injection of brine with 4-fluoro benzoic acid as tracer. However, for the effluent dispersion tests performed in this thesis, the tracer (sodium iodide) concentration at the outlet was found by measuring the electrical resistivity to the fluid over a measuring cell (*Figure 3.27*).

A new method was tested simultaneously with the resistivity test. By measuring the gamma radiation through a cell (*Figure 3.27*), the transition from one fluid to another can be monitored. There are two independent programs controlling both the counting scan and the image scan. It is not possible to use both programs at the same time, e.g. a numbers of measurements are preset, and it is required to manually switch between the different programs.

Because the viscosity of the oil was low (53 cP), it was not possible to dope (trace) the oil as it would further decrease the viscosity. The samples were initially saturated with aqueous tracer and the test started by injecting brine. Tracer has a higher electrical conductivity and attenuation than brine, and the effluent dispersion curve in the transition between the different fluids is obtained by measuring the resistivity and gamma rate, which is recorded and saved to a computer connected to the apparatus. During the effluent dispersion test, the fluid front will also be monitored by images. When the 2-D rig cabinet is closed, the temperature rises, especially when the source is nearby the measuring cell. An increase in temperature makes the measured resistivity decrease. This can be seen in the various effluent dispersion curves under *Chapter 4.1.4*.

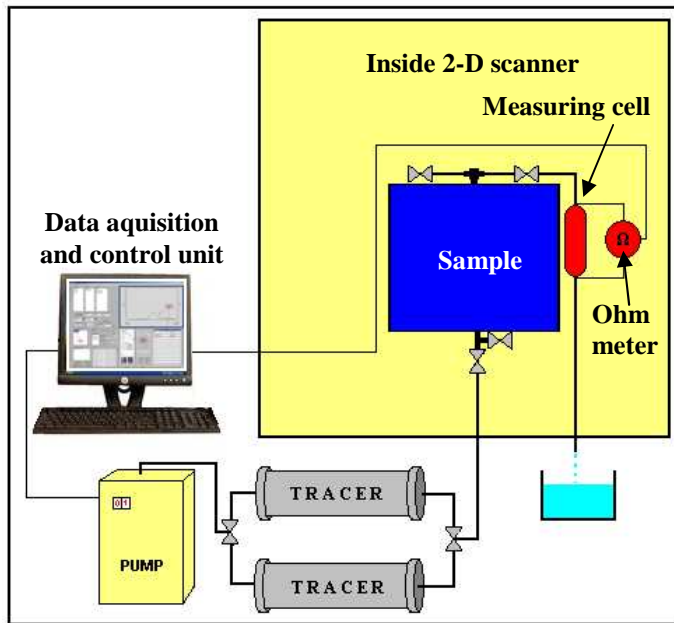


Figure 3.27 Setup for effluent dispersion test during tracer injection.

The resistivity method is more favourable compared to the UV spectrometry as it prevents adsorption, and increase the amount of data points significantly. The total analysis time is also reduced. Results are displayed in graphs where the relative concentration of tracer (C/C_0) is a function of pore volume injected. The resistivity method measures the resistance of an electric current through the measuring cell while the gamma count method measure the amount of radiation which passes through the cell. The relative concentration for both methods is found by dividing a measured concentration by a known initial concentration [75]:

$$\frac{C}{C_0} = \frac{\ln(X) - \ln(X_i)}{\ln(X_j) - \ln(X_i)} \quad \text{Equation 3.2}$$

where X is the measured concentration (both resistivity and gamma rate) during two phase flow, X_i is the concentration during one phase flow of aqueous solution with sodium iodide and X_j is the concentration during one phase flow of aqueous solution with sodium chloride. Normalising of the data enables results from both resistivity measurement and gamma counting scans to be displayed in the same graph. All effluent dispersion tests were started at 100% tracer saturation and run until 100% of the brine concentration was reached. Due to the shape of the sample, and the difficulty of sweeping the corners, 100% concentration occurred at approximately 4.0 PV (just under 2 L, which is two cylinders of tracer or brine).

3.6.3 Drainage and wettability alteration

Drainage:

The slabs are drained with North Sea oil originating from the Heidrun field. The viscosity ratio during this immiscible displacement is 53:1, and hence it is supposed to be a stable injection. Injection rate is set to 0.25 mL/min to avoid unstable displacement, and to get the lowest S_{wi} as possible. Because the Heidrun oil is lighter than water (*Table 3.4*), it is injected on top to utilize the gravitational forces. The drainage shown in *Figure 3.28* is from the broken samples, but used as an illustration.

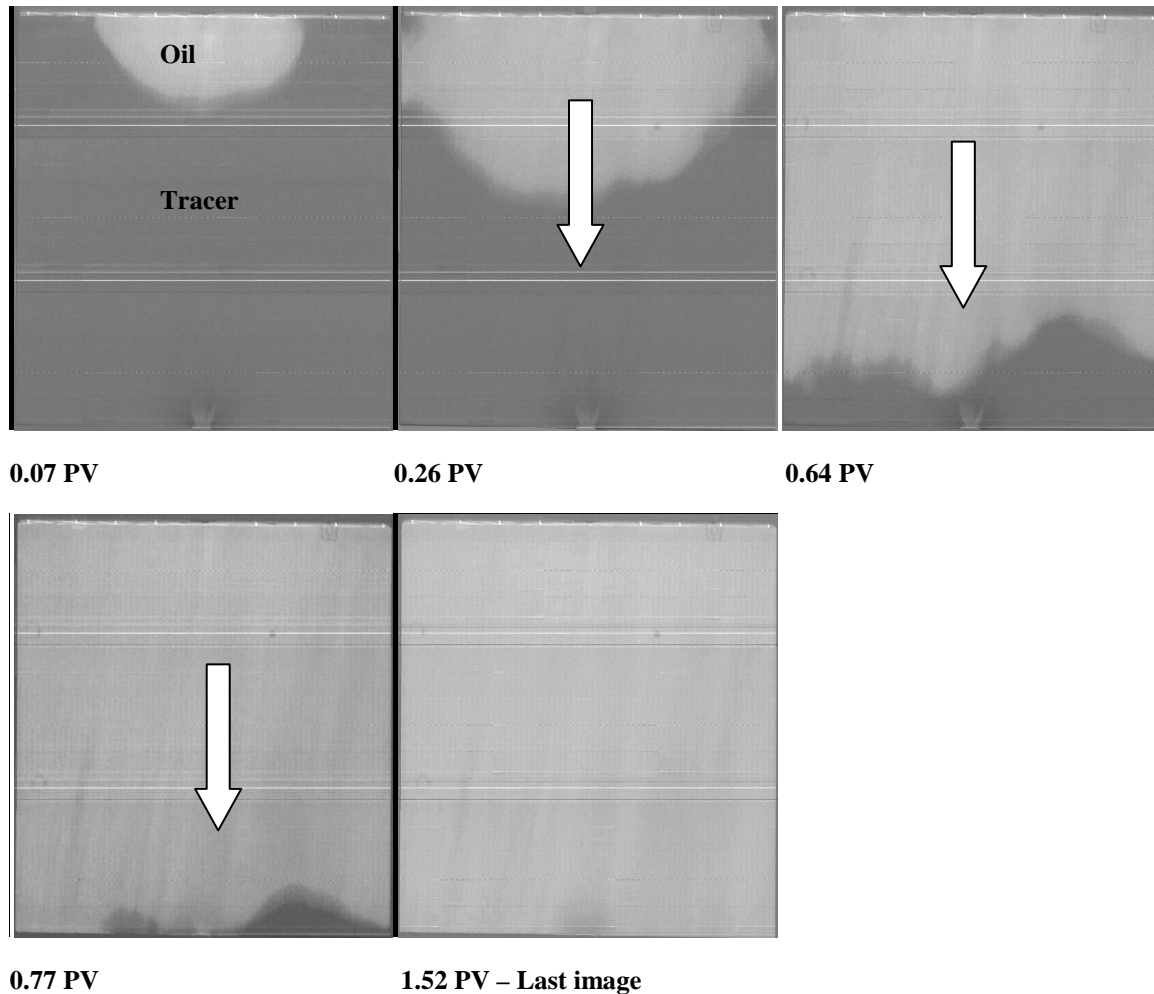


Figure 3.28 Drainage in the broken WF+PF sample at different *PV*.

From the images in *Figure 3.28* it is observed a capillary end-effect, which is to be expected in a drainage process [64]. There was observed a snap-off effect at oil breakthrough, and little water was produced after. By material balance the initial oil volume was found (V_o), and the irreducible water saturation (S_{wi}) is calculated along with the initial oil saturation (S_{oi}). The PF sample was drained exactly by the same procedure as the WF+PF sample.

Wettability alteration:

After the slabs had been drained, they were put in a heat cabinet at 70°C, connected in series to a cylinder with fresh oil in one end and a cylinder which would receive oil in the other end. The pump was connected to the cylinder with oil, and the rate was set to 0.03 mL/min (*Figure 3.29*).

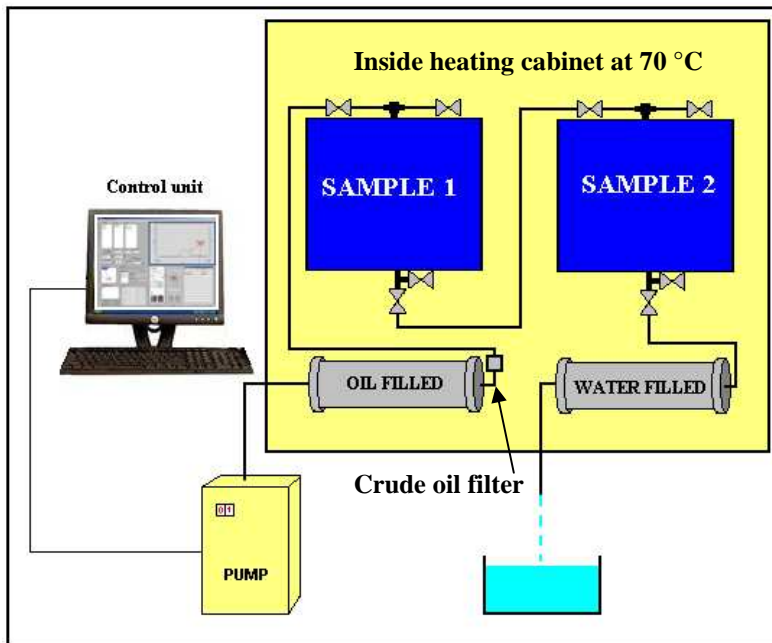


Figure 3.29 Setup for wettability alteration.

In theory, the oil-containing cylinder should be emptied in one week and the oil filter should be removed and the direction changed. It was planned to repeat this process of changing the direction two more times. Unfortunately, the preset pressure limitation forced the rate to be decreased, which occurred because the pump was set to a constant delivery rate mode with pressure limitations. The slab was not directly pressure monitored inside the heat cabinet, but the outlet pressure of the pump was used to set the limitations. In fear of breaking the samples one more time, the pressure limitation was set to 2.0 bars, but outlet pressure of the pump rose to 2.0 bars in less than one day. The pump, which was set to constant delivery mode with pressure limitation, reduced the rate correspondingly to stay below the limit.

It soon became obvious that the injection rate of the oil was low, and it was believed to be caused by the plugging of the crude oil filter by heavy components and particles in the oil. The filter was changed, but the problem persisted. Six weeks later after the ageing process started, the volume of oil injected was only 200 mL. It was concluded, after consulting with other researchers, that 70°C during a six week period was sufficient to change the wettability, despite the lack of oil flow through the samples. The dilemma of time consumption was also a reason to stop the ageing process and continue with the rest of the experiments. The slabs were put back into the 2-D core scanner and they were ready to start the water and polymer injections.

3.6.4 Polymer solution

The polymer solutions of HPAM were prepared by mixing dry polymer granulate with tracer (10% NaI) solution. To assure sufficient stirring, a Heidolph rack mounted overhead mixer was used instead of a magnetic stirrer (*Figure 3.30*). The mixer propeller was custom made by the polymer manufacturer, with rounded blades to avoid unwanted shear. The concentration for a solution was 1000 ppm, and was prepared by a CIPR modified SNF procedure:

- 1) HPAM granulate and the 10 wt% NaI solution was weighed in separately onto a weighing tray and 800 mL beaker respectively.
- 2) The beaker was placed on jack plate and placed under the Heidolph mixer and the propeller should be centred in the beaker, approximately 2.5 cm above the bottom. The mixer was set to 600 rpm, and a vortex without stagnant air bubbles should appear.
- 3) HPAM granulate was poured slowly into the vortex without contacting the propeller shaft. A quantity of approximately 0.5 g of granulates per minute proved to be adequate.
- 4) The mixer ran for 12 to 24 hours mixing at 600 rpm. A Parafilm seal on top of the beaker was applied.



Figure 3.30 Right: Heidolph mixer. Left: Mixing of HPAM solution.

Prior to an experiment, the solutions were gravity filtered through a 40 μm filter to remove precipitations and/or microgels. After filtration the solution was poured into a piston cylinder.

3.6.5 Viscosity measurements

The viscosity measurements were performed with a modular compact rheometer, the Physica MCR300 by Anton Paar (*Figure 3.31*). The MCR300 features two measurement geometries. The cone plate geometry (CP-75) is preferred for samples with a presumed viscosity higher than 10 cP (e.g. polymer solutions) consisting of a sample plate stator and a slightly coned plate rotor (*Figure 3.31*). For samples with a presumed viscosity below 10 cP (e.g. diluted solutions, brines and tracers) the double gap geometry (DG-26.7) is preferred. However, there will be several transitions from tracer/brine to polymer solution in both slabs and the cone plate geometry is assumed as the best choice to cover the large range of viscosities in the experiments.

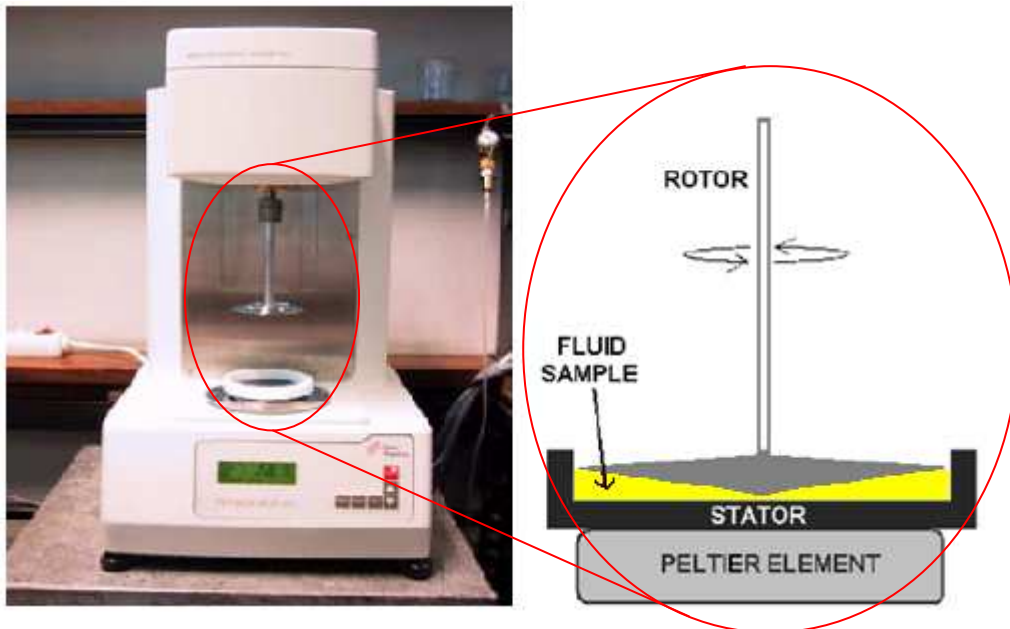


Figure 3.31 Left: MCR300 Rheometer by Anton Paar. Right: Cone plate measuring geometry.

The Rheometer measures the rotor speed, and can calculate the shear rate by multiplying with a known constant C_1 . Similarly, the shear stress is given by the torque multiplied with a constant C_2 . The viscosity is then calculated as the shear stress divided by the shear rate. C_1 and the C_2 constants are unique for each measuring system. For temperature control, both stators are mounted on a Peltier apparatus with water cooling and electric heating. All experiments are carried out at $22 \pm 0.1^\circ\text{C}$. Periodically and if the geometry is changed, the Rheometer has to be checked for erratic behaviour. This is done by measuring the viscosity of the Newtonian fluid PDMS200.

Before each measurement, all parts that are in contact with the sample fluid were thoroughly cleaned and dried. First with soap and water, then rinsed 3-5 times with distilled water and finally dried with clean pressurized air. Before any measurements can be done, the Rheometer and corresponding software must be turned on and initialized. The sample cup or plate is fastened in the holder and levelled with a tubular spirit level and the fluid sample is carefully dispensed with a pipette onto the plate or cup. The volume required is 4.1 mL for the DG and 3.0 mL for the CP. After the Peltier apparatus has been set to the desired temperature, one should wait a few minutes with the rotor placed in measuring position to let the heat distribute through the sample. During measurements a Plexiglas cover is put over the Rheometer to protect the sample from air fluctuations.

For both geometries, the measurement procedures starts with five minutes of temperature equilibration, thereafter the software starts the measurements automatically when the temperature has been constant at $22 \pm 0.1^\circ\text{C}$ for ten seconds. The measurement starts with 21 measuring points with logarithmic increase in the shear rate range of 0.1 to 1000 (1/s). Finally, the same points are measured again with decreasing shear rate. The measuring time for each point varies logarithmically from 10 seconds for the highest shear rate, and up to 30 seconds for the lowest. After the viscosity measurements, the data is transferred to Excel sheets in order to make proper graphs of the measured samples.

4 Results and Discussion

In this chapter the results are presented in chronological order. Sample characterisations such as porosity, permeability measurements and dispersion tests are reported. The main scope of this thesis is to investigate the mechanisms behind enhanced oil recovery by studying the high resolution images provided by the 2-D core scanner, supplemented by figures, curves and tables of effluent analysis. Final images (retracted) were put together by MATLAB and if unmodified images are used, it will be specified in that section. The differential pressure measurements during all main experiments are displayed in Appendix A.

4.1 Porous media characterisation

Basic parameters such as porosity and permeability are calculated, and dispersion tests are performed to characterize the porous medium with regards to heterogeneities.

4.1.1 Porosity and oil saturation

Porosity:

From the cumulative pump volume, the slabs seem to be quite similar in terms of porosity (*Table 4.1*). The porosity of 22% is as expected (from Chapter 2.3).

Table 4.1 Pore volume and porosity for the slabs.

Sample	V_{dead} [mL]	V_p [mL]	ϕ_{eff} [%]
WF+PF	6.0 ± 0.5	431 ± 4	22 ± 1
PF	5.5 ± 0.5	430 ± 4	22 ± 1

Oil Saturation:

The slabs are drained with viscous oil (53 cP) and the volume of water from the measuring cylinders is calculated. Drained volumes are shown in (*Table 4.2*). The samples are quite identical in terms of S_{wi} values, which were expected because the samples were from the batch.

Table 4.2 Drainage values of the WF+PF and PF sample.

Sample	V_o [mL]	S_{wi} [%]	S_{oi} [%]
WF + PF	354 ± 3	18	82
PF	350 ± 3	19	81

4.1.2 Effective permeability

Calculating the permeability of the samples is not straight forward. In Darcy's law it is assumed that the surface area of the sample is known. The problem for these samples is the different surface areas between inlet (0.59 cm^2) and outlet (60.0 cm^2). It has been calculated in earlier experiments that Bentheimer sandstone has an average absolute permeability of around $2.5 \pm 0.5 \text{ D}$ [3, 55] and comparisons will be made to these known values. Two specific methods have been used to find suitable permeabilities for the two slabs. The results from permeability measurements are shown in *Table 4.3*.

Table 4.3 Calculated permeabilities of the WF+PF and PF sample.

Sample	Permeability method 1 [D]	Permeability method 2 [D]
WF + PF	0.58 ± 0.04	2.9 ± 0.2
PF	0.52 ± 0.04	2.7 ± 0.2

It seems that this method 1, where equal inlet and outlet area are assumed, underestimate the permeability. This is to be expected as the assumed surface is much higher than in reality, and the pressure should be much lower if this was the case. The values calculated for method 2, radial flow, seem to match the expected values and may be regarded as satisfactory.

The permeability of the PF sample seems to be lower than for the WF+PF sample. The reason for that will be investigated later on during the effluent dispersion tests.

4.1.3 Relative permeability and mobility ratio

After the assumed wettability alteration, the effective oil permeability at irreducible water saturation was measured for both samples using the same equipment as for absolute permeability measurements. For the WF+PF sample, the effective water permeability ($k_{e,w}$) was measured after water injection at remaining oil saturation.

Table 4.4 Endpoint values of relative permeability.

Sample	$k_{ro,iw}$ [-]	$k_{rw,or}$ [-]	M^0 [-]
WF + PF	2.1	0.13	3.2
PF	2.7	-	-

By the calculated values in *Table 4.4* it can be made some assumptions about the wettability alteration. The relative oil permeability for both samples are higher than 1, something which is not stated in theory. However, in practice this occurs frequently and the reason for this is that in a water-wet porous medium the oil will be located in the middle of the pore. If no wettability alteration has happened, the oil will still be situated in the same location as before. When measuring oil permeability during these conditions, the oil has no contact with the tortuous rock walls. This enables a gliding effect for the oil, and thus higher oil permeability is correctly measured. It can be concluded that the slabs are not strongly oil-wet.

Relative water permeability for the WF+PF sample is quite low, which indicates a water-wet case. It is not possible to state that the samples are strongly water-wet either due to the uncertainty of the inlet and outlet configuration.

The endpoint mobility ratio for the WF+PF sample is calculated to $M^0 = 3.2$, not as high as expected. However, the mobility ratio calculated for the WF+PF sample might not be so reliable. The relative endpoint water permeability is measured in a system with both fingering and unswept zones, and since the mobility ratio is a Buckley-Leverett consideration it may affect the calculated value.

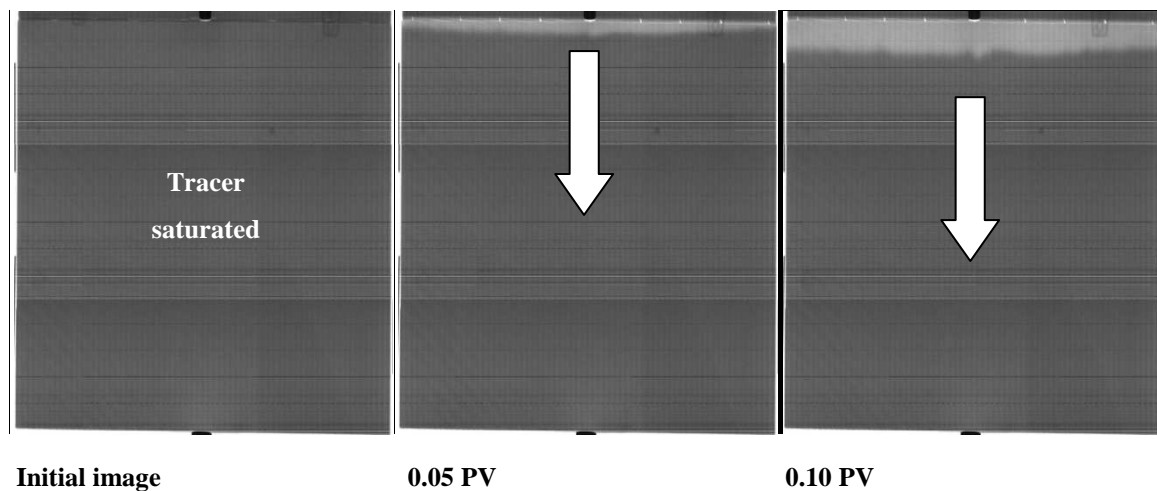
4.1.4 Effluent dispersion tests

WF+PF sample:

To identify heterogeneities in the porous medium, a dispersion test is used. The viscosity ratio during the miscible displacement, i.e. dispersion test, is 1:1, and should accordingly be stable. The samples are initially saturated with tracer. Brine is slightly lighter than tracer (*Table 3.4*), and will be injected from the top of both samples. When the brine has fully replaced the tracer, tracer will be reinjected from the lower injection point, and by time displace all brine in the sample.

The dimensionless number, pore volume injected (*PV*), is calculated by MATLAB when the images are put together. *PV* is calculated at the start of every image taken, which is written to the original image file. One image takes about five minutes to complete, and the MATLAB calculated pore volume injected is therefore slightly uncertain.

The injection rate is set to 2 mL/min for all dispersion experiments. All images shown in *Figure 4.1* are drawn from an initial image, which means that only differences from an initial image are captured.



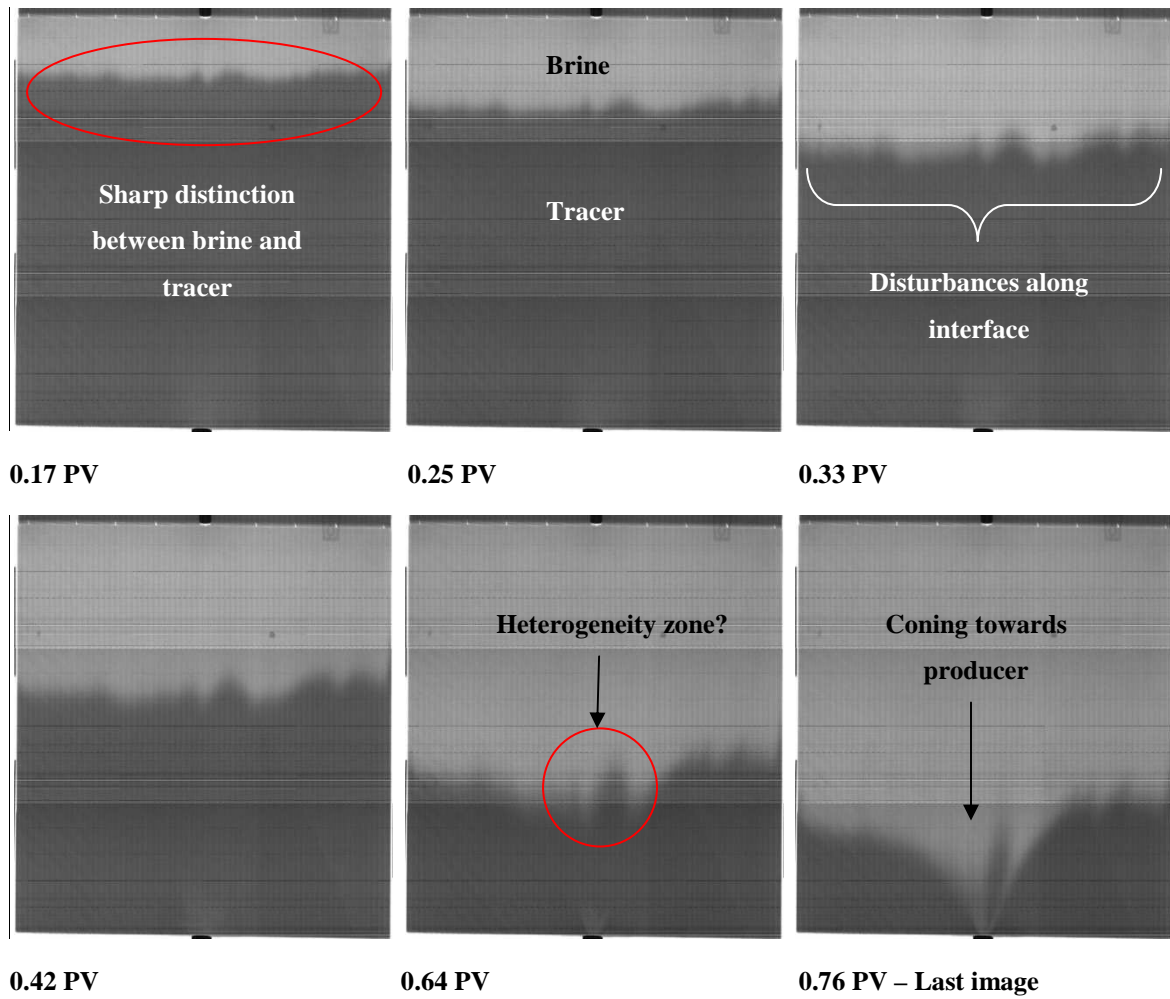


Figure 4.1 Brine displacing tracer in the WF+PF sample at different PV.

A sharp interface between brine and tracer is observed in addition to some disturbances (*Figure 4.1*). The rest of the images indicate a heterogeneity zone and coning behaviour towards the producer at the end of the injection.

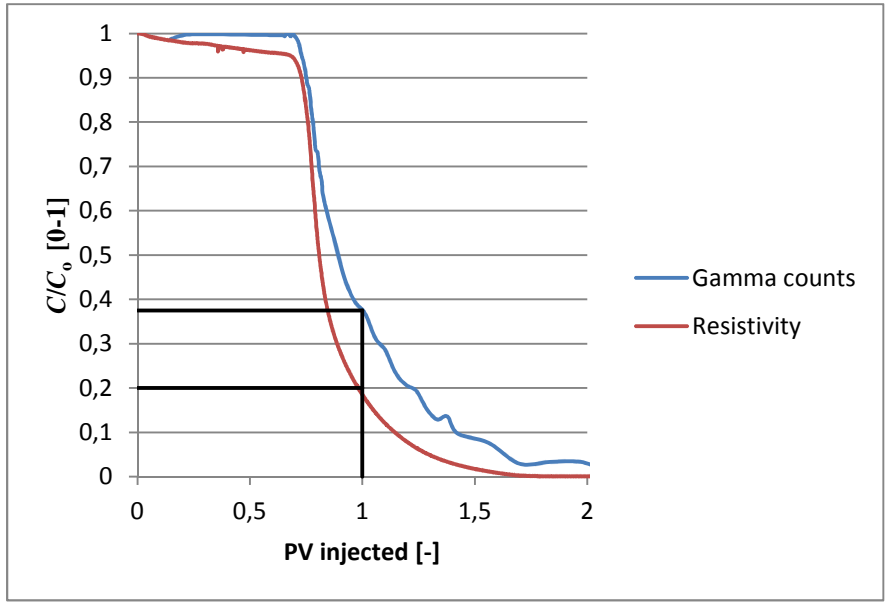


Figure 4.2 Effluent dispersion curve for brine displacing tracer in the WF+PF sample.

The shape of the curve (*Figure 4.2*) above is not symmetric around 1 PV. This most likely due to the coning shape in the end of the flow and the area sweep efficiency.

Table 4.5 C/Co of tracer at 1 PV of brine in the WF+PF sample.

Method	C/C _o at 1 PV
Resistivity	0.20
Gamma count	0.38

The values from *Table 4.5* indicate that the front arrives before an ideal scenario, and is affected by the fingering coning shape of the front. At 1 PV the resistivity measurement shows 20% tracer concentration instead of the ideal 50% tracer concentration for no fingering, retention and dead-end pore volume. The gamma count is different and displays a concentration of 38% at 1 PV. It is not speculated any more in the difference between gamma and resistivity measurements. When the brine injection is completed, tracer can be reinjected into the sample as shown in *Figure 4.3*.

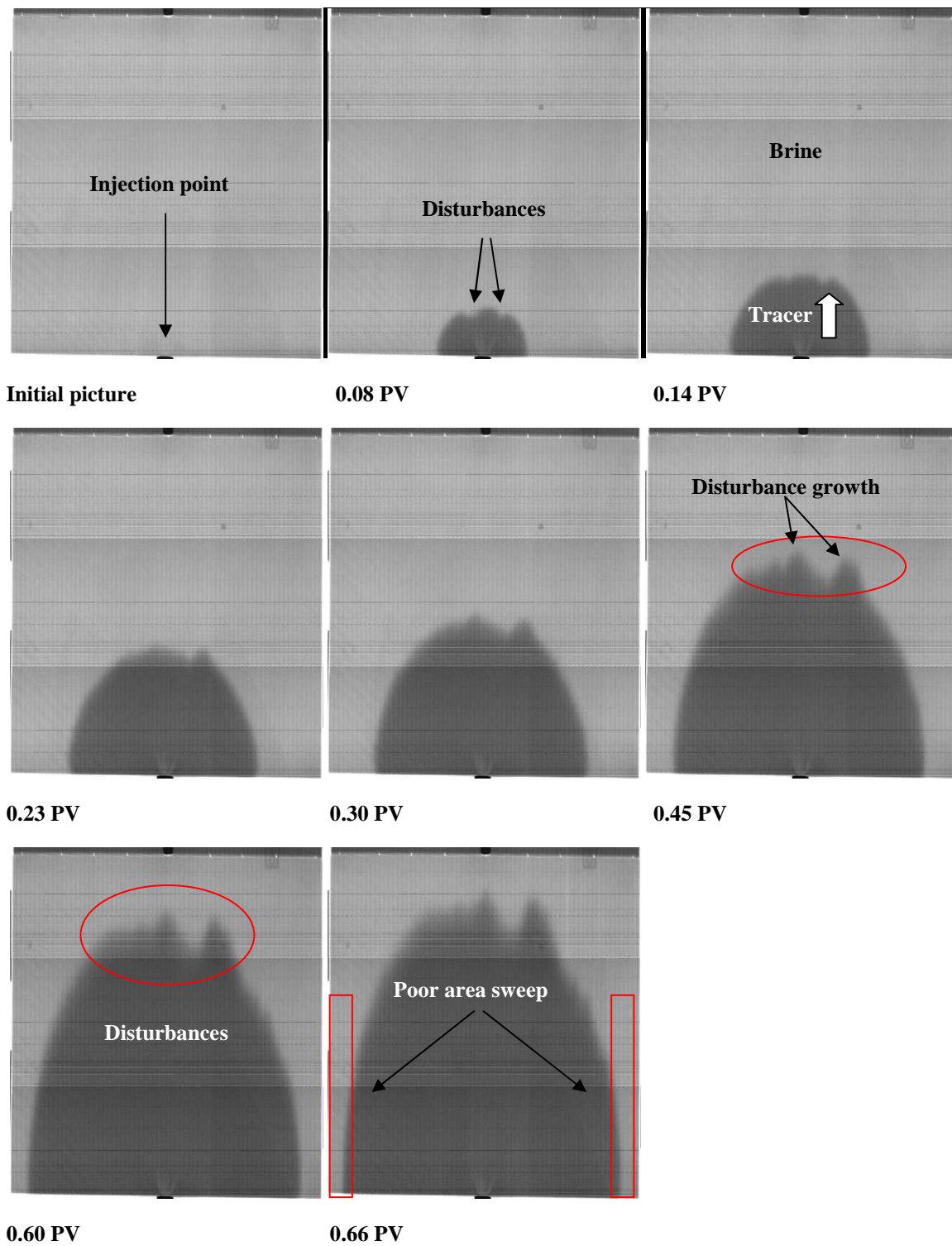


Figure 4.3 Tracer displacing brine in the WF + PF sample at different PV.

The reinjection of tracer confirms the heterogeneity zones in this sample. *Figure 4.3* at 0.66 PV shows a poor displacement at the sides of the sample. This may have a connection with the fact that the ratio of the area of the injection point (0.6 cm^2) and the outlet dispersion rail (60 cm^2) is quite large.

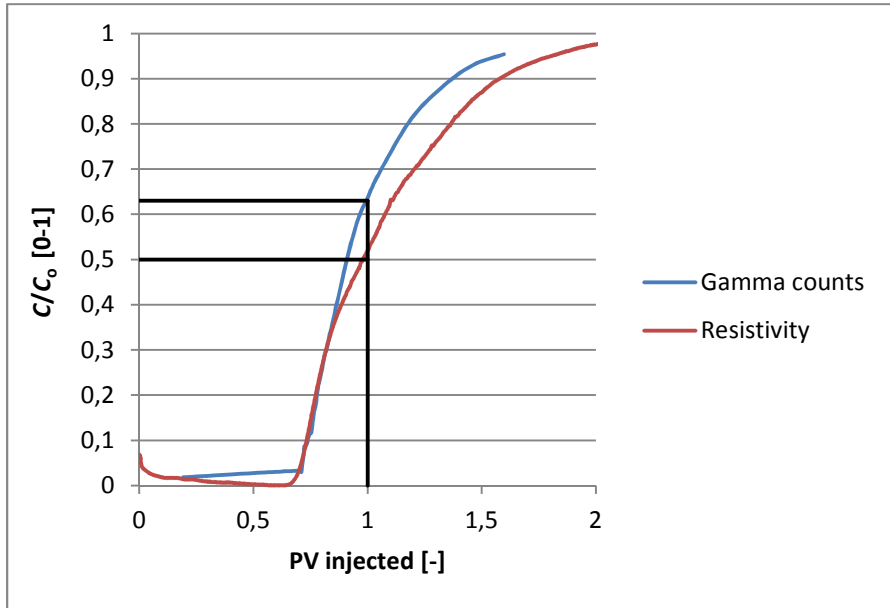


Figure 4.4 Effluent dispersion curve for tracer displacing brine in the WF + PF sample.

The shape of the curve in *Figure 4.4* is not symmetric around 1 PV and is most likely caused by the sweep efficiency.

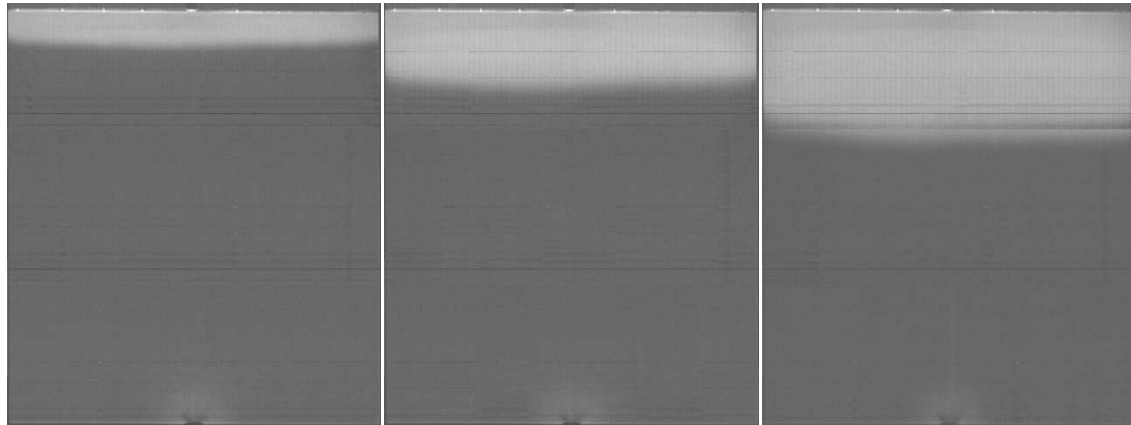
Table 4.6 C/Co of tracer at 1 PV of tracer in the WF+PF sample.

Method	C/C ₀ at 1 PV
Resistivity	0.50
Gamma count	0.63

At 1 PV (*Table 4.6*) the concentration of tracer is 50%, which indicates a piston displacement and little dead-end pore volume. The gamma counts deviates from the resistivity measurement at 50% tracer concentration.

PF sample:

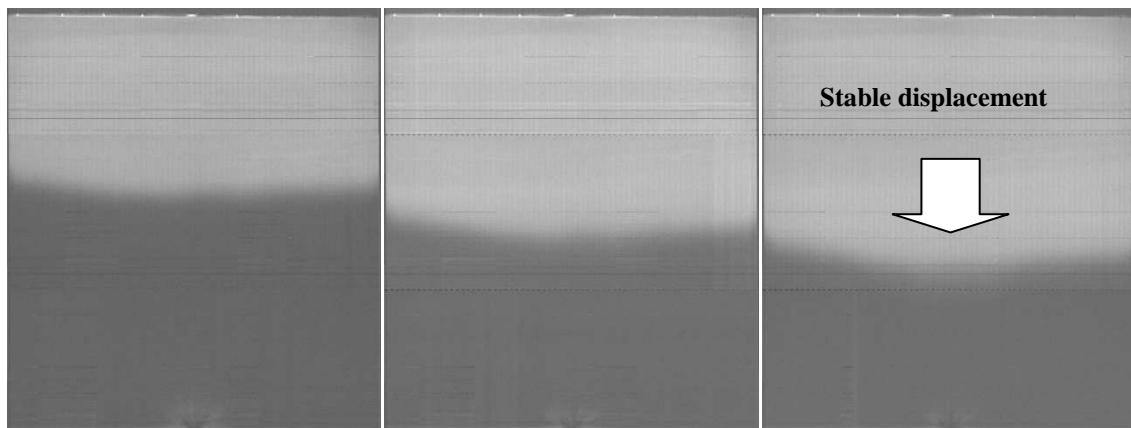
The dispersion test is performed in the polymer flooding sample. At first, the injection of brine into the sample is performed with an injection rate of 2 mL/min.



0.10 PV

0.20 PV

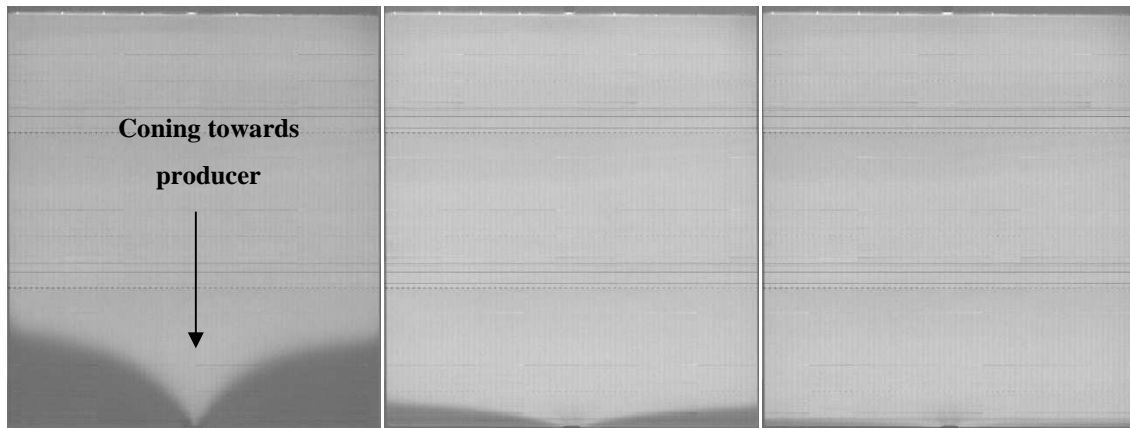
0.31 PV



0.43 PV

0.53 PV

0.61 PV



0.85 PV

1.30 PV

1.84 PV

Figure 4.5 Brine displacing tracer from top in the PF sample.

It can be observed from the images in *Figure 4.5* that the PF sample seems more homogeneous than the WF+PF sample. The same coning behaviour observed in the WF+PF sample, also occurs in the PF sample.

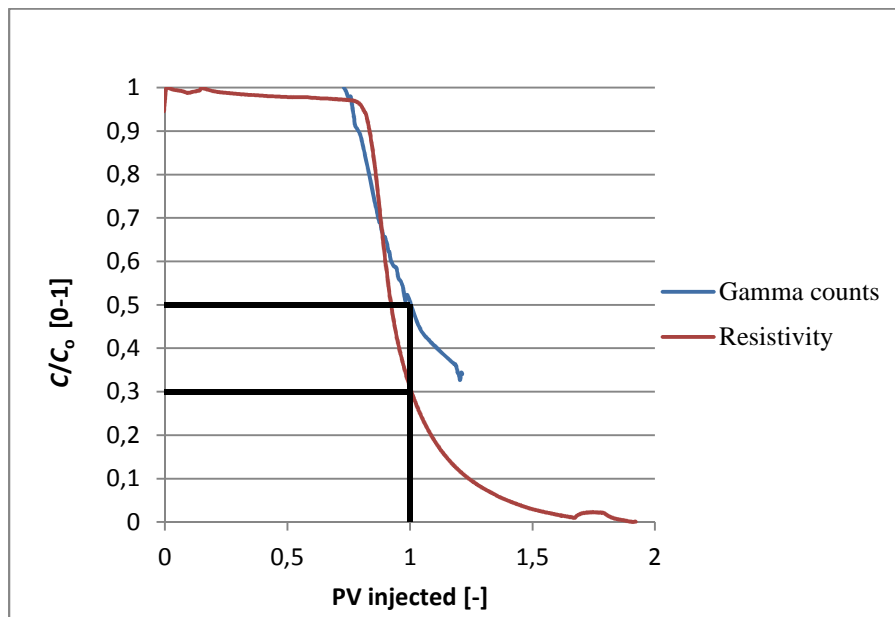


Figure 4.6 Effluent dispersion curve for brine displacing tracer in the PF sample.

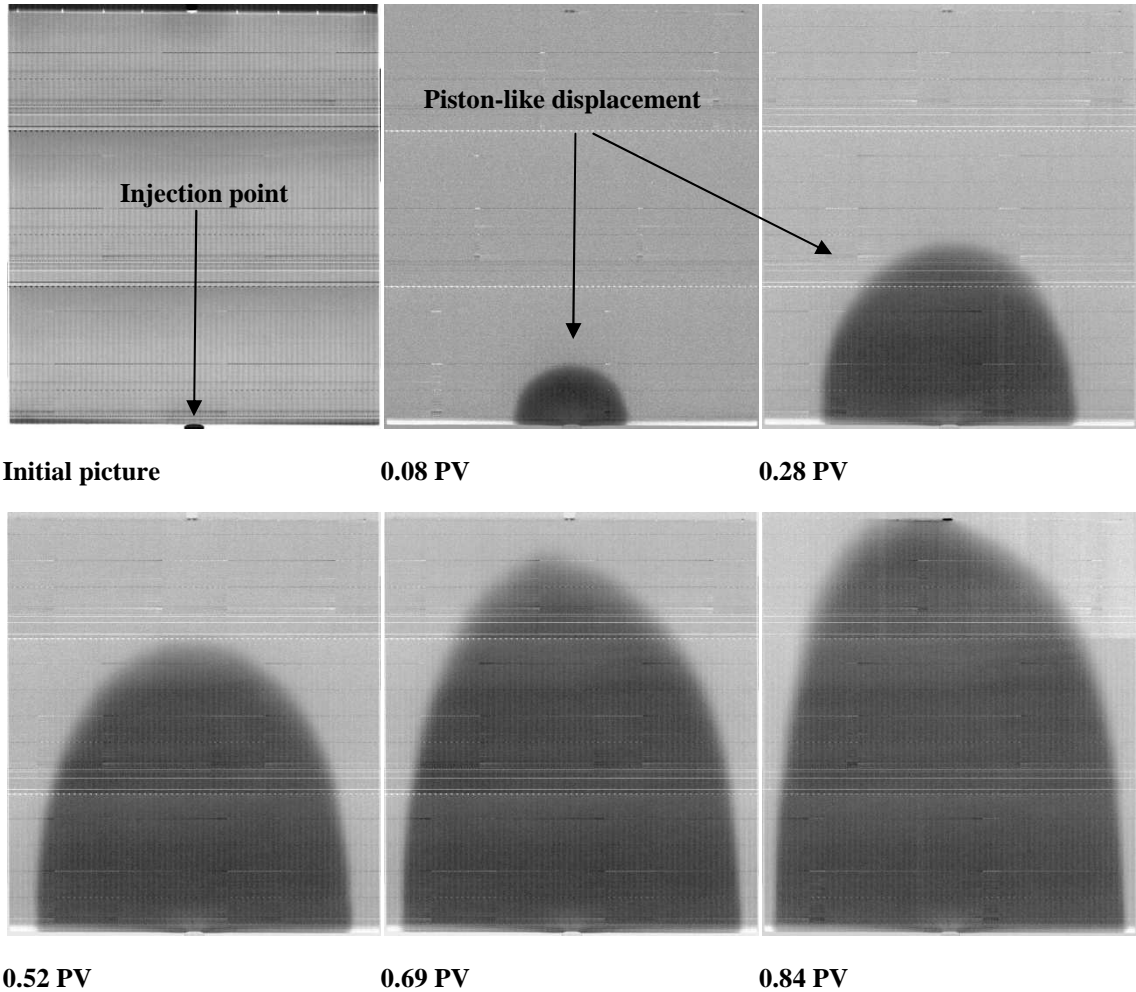
Figure 4.6 is not symmetrical around *PV* injected. This is most likely, as for the WF+PF sample, caused by the sweep efficiency.

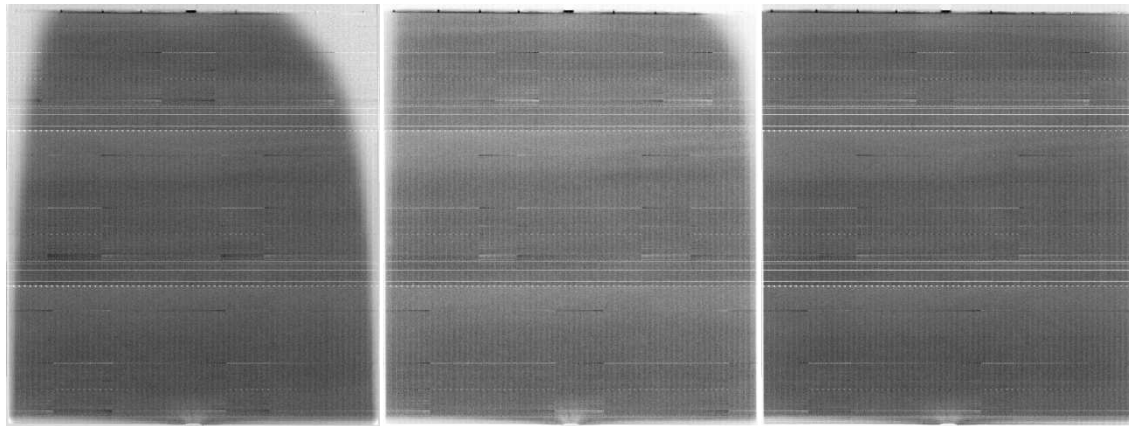
Table 4.7 C/C_0 of tracer at 1 *PV* of brine in the PF sample.

Method	C/C_0 at 1 <i>PV</i>
Resistivity	0.30
Gamma count	0.51

As for the WF+PF sample, the 1 PV value of tracer is lower than 50%. The injection front has the same fingering coning shape as the WF+PF sample, which is probably the reason for the early breakthrough. The measurement of gamma count is not satisfactory, due to its deviating values and lack of measurements.

When the brine injection is stopped, tracer is reinjected into the sample (*Figure 4.7*). Note that the initial picture is not drawn from another picture, it is unmodified. That is the reason why noise is more visible than in the other images.





1.16 PV

1.65 PV – Injection stop

21 hours after injection stop

Figure 4.7 Tracer displacing brine in the PF sample at different *PV*.

From the images (*Figure 4.7*) a stable front is observed and the sample seems quite homogeneous. Note that the front has reached the outlet at $0.84 PV$ and it takes an additional $0.81 PV$ to a total of $1.65 PV$ to improve the sweep. However, when the injection is stopped, in the upper right corner at $1.65 PV$ a small area is still unswept. The sample is left still for 21 hours, and as expected diffusion corrected for the lack of sweep. Effluent dispersion curve of the injection is shown in *Figure 4.8*.

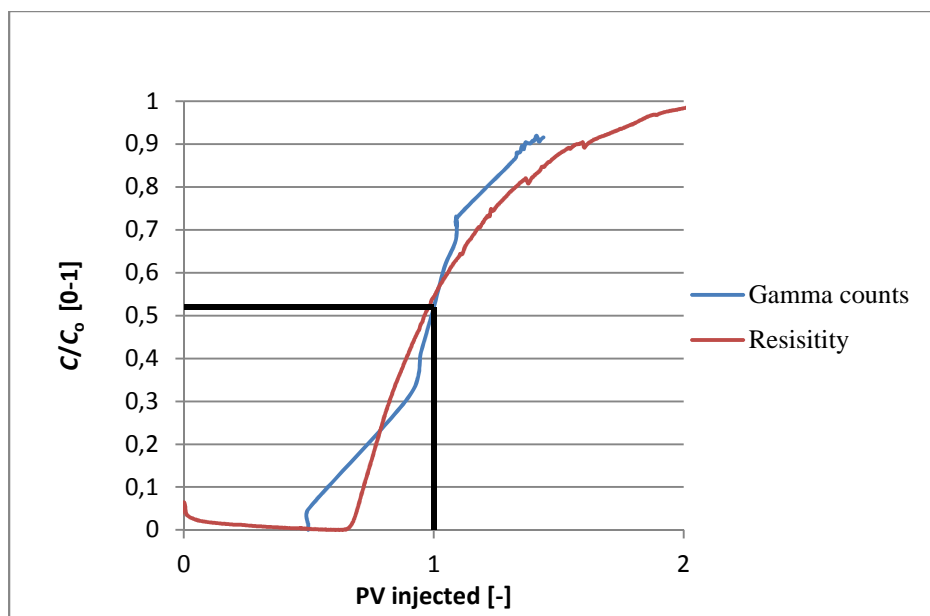


Figure 4.8 Effluent dispersion curve for tracer displacing brine in the PF sample.

Figure 4.8 is not symmetrical around $1 PV$ injected, which is most likely due to the sweep efficiency.

Table 4.8 C/C_0 of tracer at 1 PV of tracer in the PF sample.

Method	C/C_0 at 1 PV
Resistivity	0.52
Gamma count	0.52

The tracer concentration at 1 PV is just above 50%, which indicate little dead-end pore volume and relatively piston-like displacement. The gamma count coincides with the resistivity method at 1 PV, but deviate at all other points.

Summary of effluent dispersion tests:

Effluent resistivity measurements are compared between the two samples, whereas gamma counts are left out due to the poor data quality of the measurements.

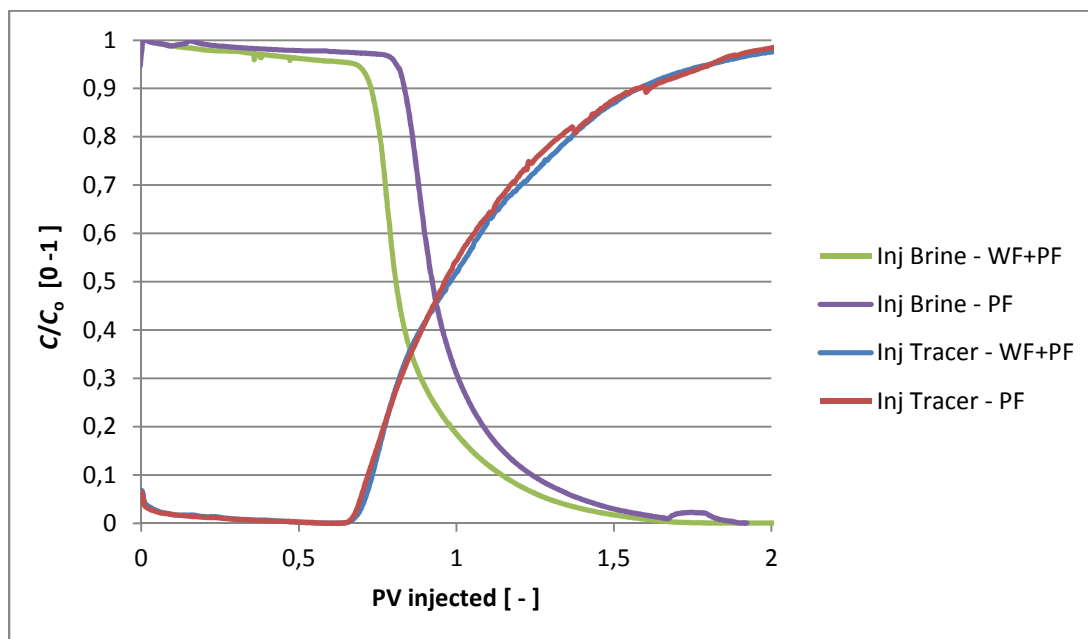


Figure 4.9 Comparison of effluent resistivity measurements for the WF+PF and PF sample.

From *Figure 4.9* it is observed a difference between the brine injections. The front of brine is faster for the WF+PF sample compared to the PF sample, whereas the tracer injections are quite similar. The most likely reason for the earlier breakthrough of brine in the WF+PF sample is because of the enhanced coning behaviour due to the heterogeneity of the sample. The injection of tracer is more stable, and hence the curves overlap.

WF+PF sample:

The images from both the brine and tracer injection and the effluent dispersion curves indicate a heterogeneity zone in this sample (images in *Figure 4.1* and *Figure 4.3*). The effluent dispersion curves show tail production (unsymmetrical around 1 PV), and the most likely reason for this is that it takes time to sweep the whole area of the sample.

PF sample:

Both the images and the effluent dispersion curves indicate a relatively homogenous porous medium. The curves show signs of tail production, and a possible and most likely reason for this is that it takes time to sweep the whole area of the sample, which is the same conclusion as for the WF+PF sample.

Based on the images and effluent dispersion curves, the PF sample seems to be more homogeneous than the WF+PF sample.

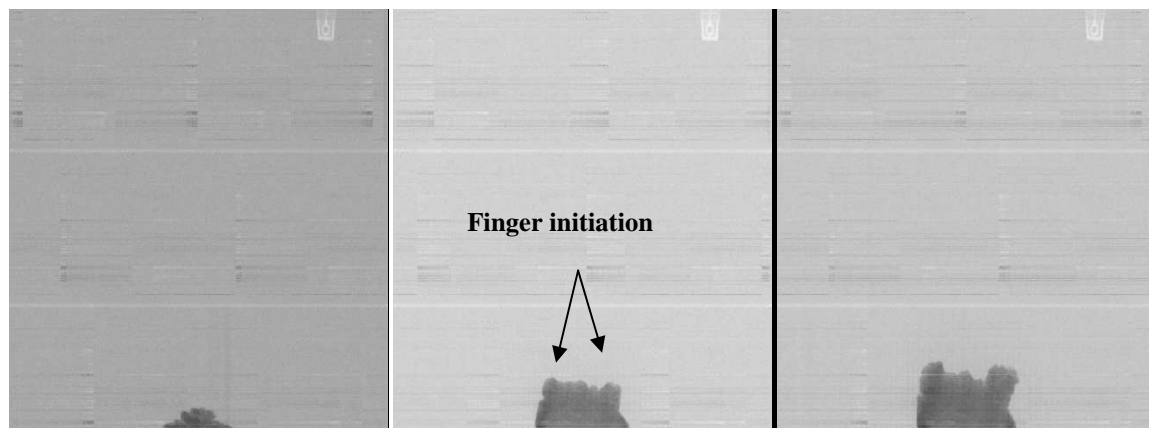
The gamma count scan test was not satisfactory, especially not for the PF sample. It was an experiment to see the possibility for a new method for measuring effluent concentration, which proved invaluable. The reason for this is most probably the lack- and quality of the measurement, compared to the resistivity method.

4.2 The water flooding and polymer flooding sample (WF+PF)

The main experiments for each sample are run individually to obtain the best image monitoring possible. The WF+PF slab is going to be exposed to a primary water injection and subsequently by a secondary polymer injection. The interesting and realistic next step will be to inject chase water and observe how it will flow behind the polymer.

4.2.1 Water injection

The viscosity ratio during this immiscible water/oil displacement is 1:53, and hence it is an unstable injection. The injection is monitored in-situ by the 2-D core scanner. This water is referred to in the dispersion test as tracer, because it is doped with iodide. It is the same water which is injected in this experiment, but here it is simply called water. The injection rate is set to 0.1 mL/min and the water injection went on continuously for four days. Lack of measurements and images has its natural reason of no night-time monitoring. Five initial pictures were taken before the flooding started.



0.0065 PV

0.02 PV

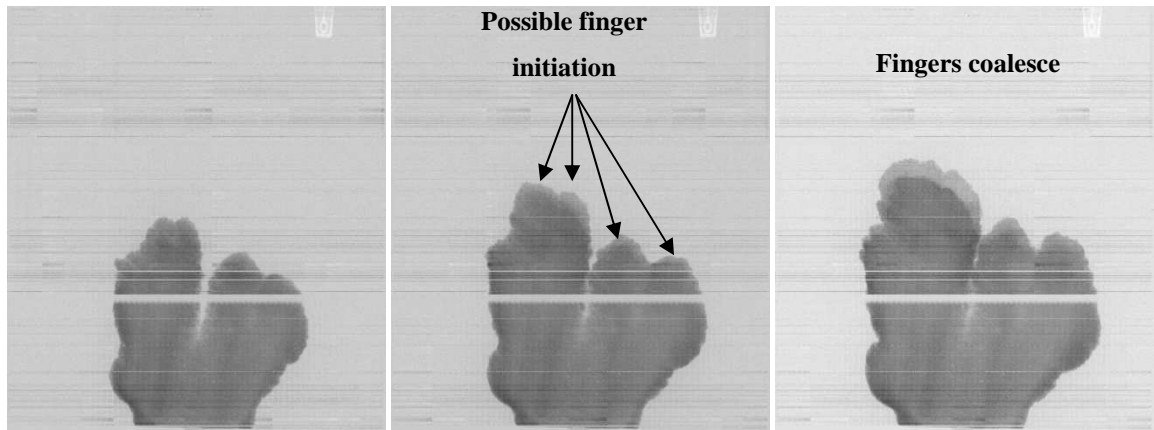
0.03 PV



0.04 PV

0.07 PV

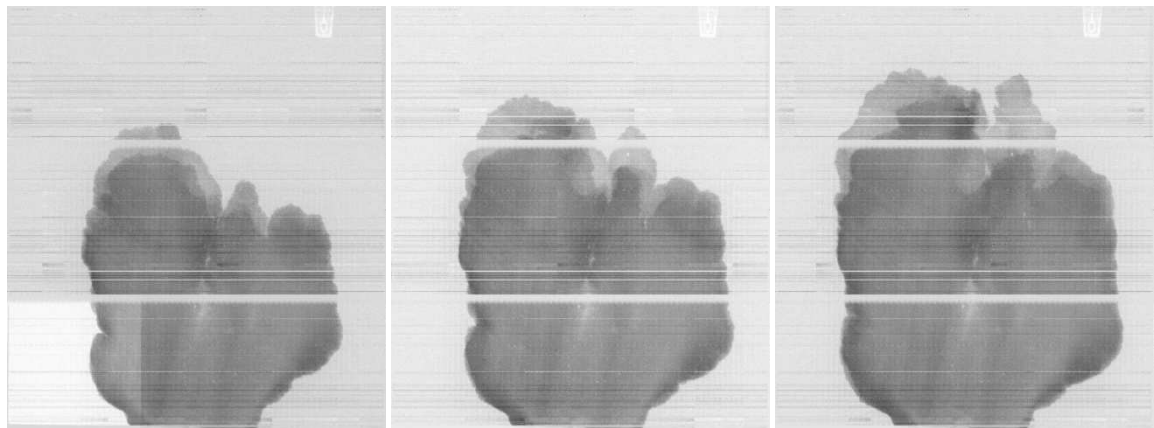
0.09 PV



0.13 PV

0.17 PV

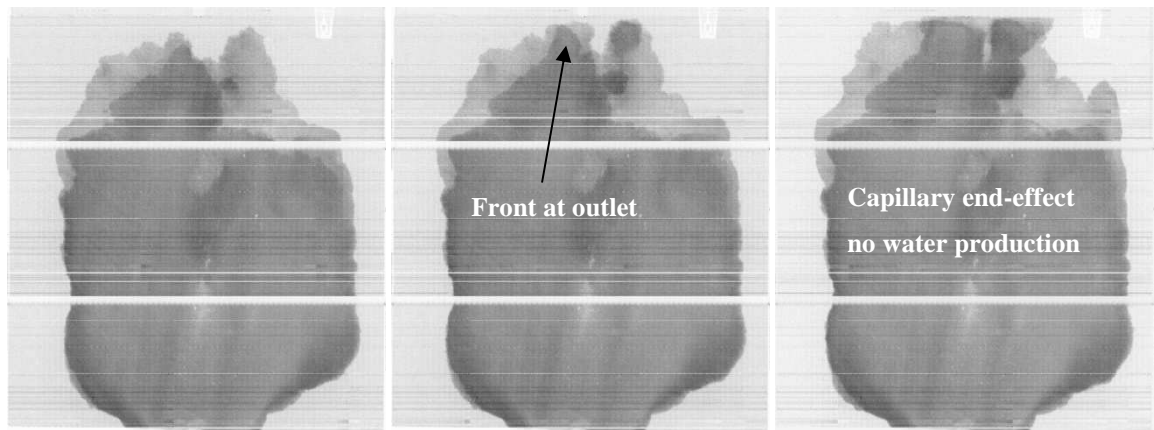
0.21 PV



0.25 PV

0.31 PV

0.36 PV



0.42 PV

0.44 PV

0.47 PV

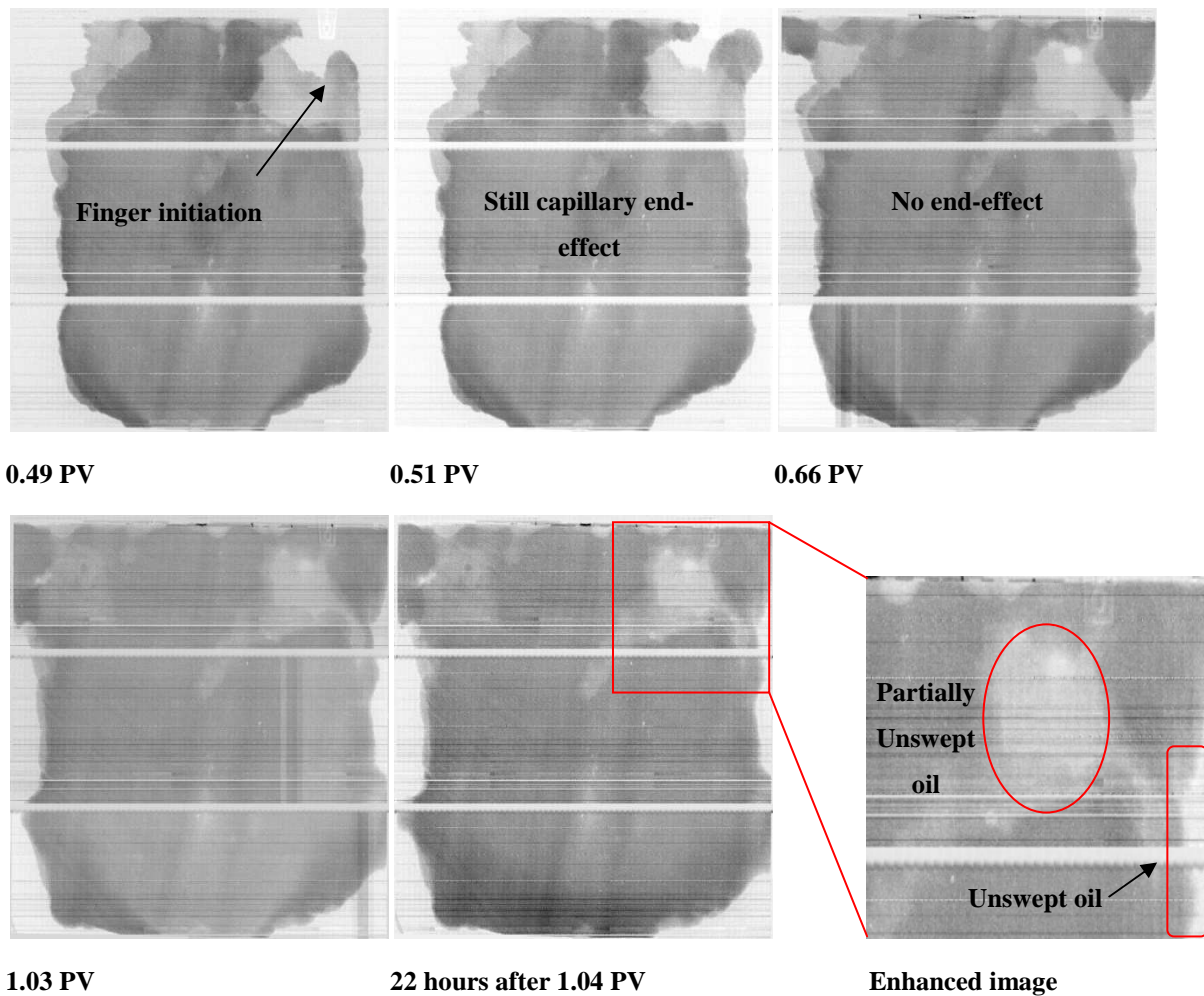


Figure 4.10 Water injection in the WF+PF sample at different PV.

There was less fingering than anticipated and it looks like finger initiation is dampened in the front of the injection (*Figure 4.10*). Behind the fingering zone, there is just water which flow without instabilities. This situation is similar to the numerical simulations performed by Riaz and Tchelepi [76] in *Figure 4.11*, where the front is exposed to instabilities and behind the front the flow is piston-like.

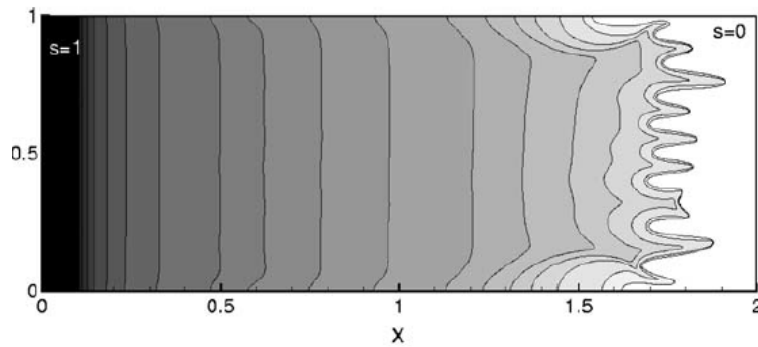


Figure 4.11 Numerical simulation of fingering in front and Buckley-Leverett behind the instabilities [76].

Initiated fingers grew together during the displacement, and from the different images it looks like the area sweep efficiency is quite good (*Figure 4.10*). The reason for the good recovery is most probably due to the high permeable porous medium (i.e. low capillary forces). The unswept areas at the sides of the sample and the residual oil saturation in the swept area remain target for the polymer injection.

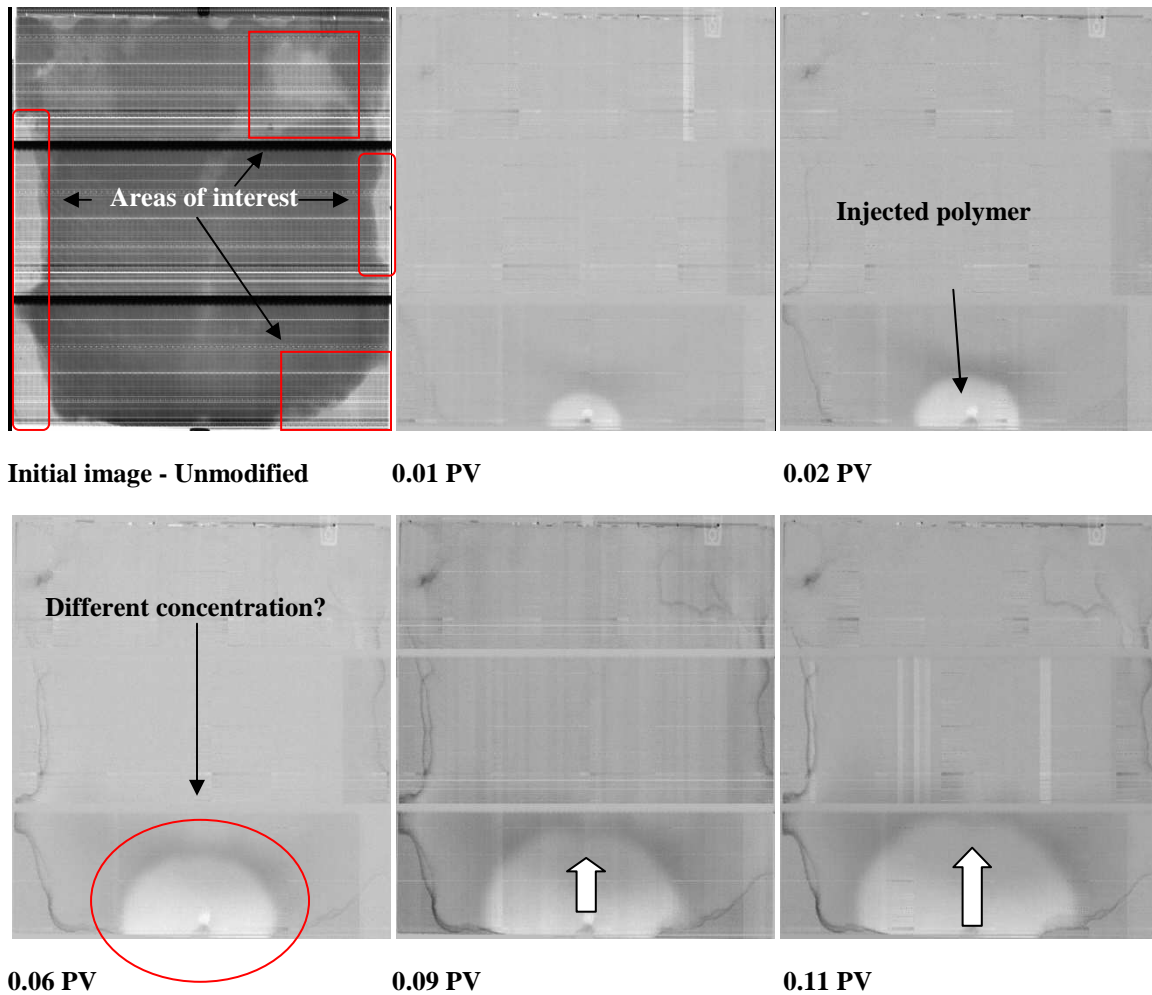
The sample suffers from capillary end-effects between 0.44 *PV* to 0.66 *PV*, where the water front reaches the end of the sample, but no water is produced before $S_w(P_c=0)$. With regards to *Figure 4.10* at 1.03 *PV* and 1.04 *PV* (21 hours later) it can be seen that little or no diffusion has occurred towards the unswept areas. During the time scale at this level, diffusion can be neglected.

The enhanced image (*Figure 4.10*) has some interesting areas. The darker the degree of grey colour, the higher the concentration of tracer. Down to the right in the enhanced image, a zone which is almost white is unswept and still contains oil. The zone which is called partially unswept has a grey scale in between white and grey. This indicates that the area has been partially swept in distinct layers. The latter can also be observed in previously images in *Figure 4.10*. Porous media may experience layers with variation in permeability which will affect the front velocity, and hence the vertical sweep efficiency (E_v).

4.2.2 Polymer injection

During the polymer injection there are three different fluids present in the sample, which means that polymer pushes on both the water and oil. The viscosity ratio during the polymer/oil displacement is approximately 11:53, which makes it a more favourable injection than water but still unstable. Viscosity ratio between polymer and water is approximately 11:1, and hence it is a stable displacement.

The polymer solution is injected with a rate of 0.1 mL/min. Three initial pictures were taken before the flooding started and put together as one average. The areas of interest are shown below in the initial image of *Figure 4.12*. The rest of the images are retracted from the initial image, showing only the difference (i.e black colour).



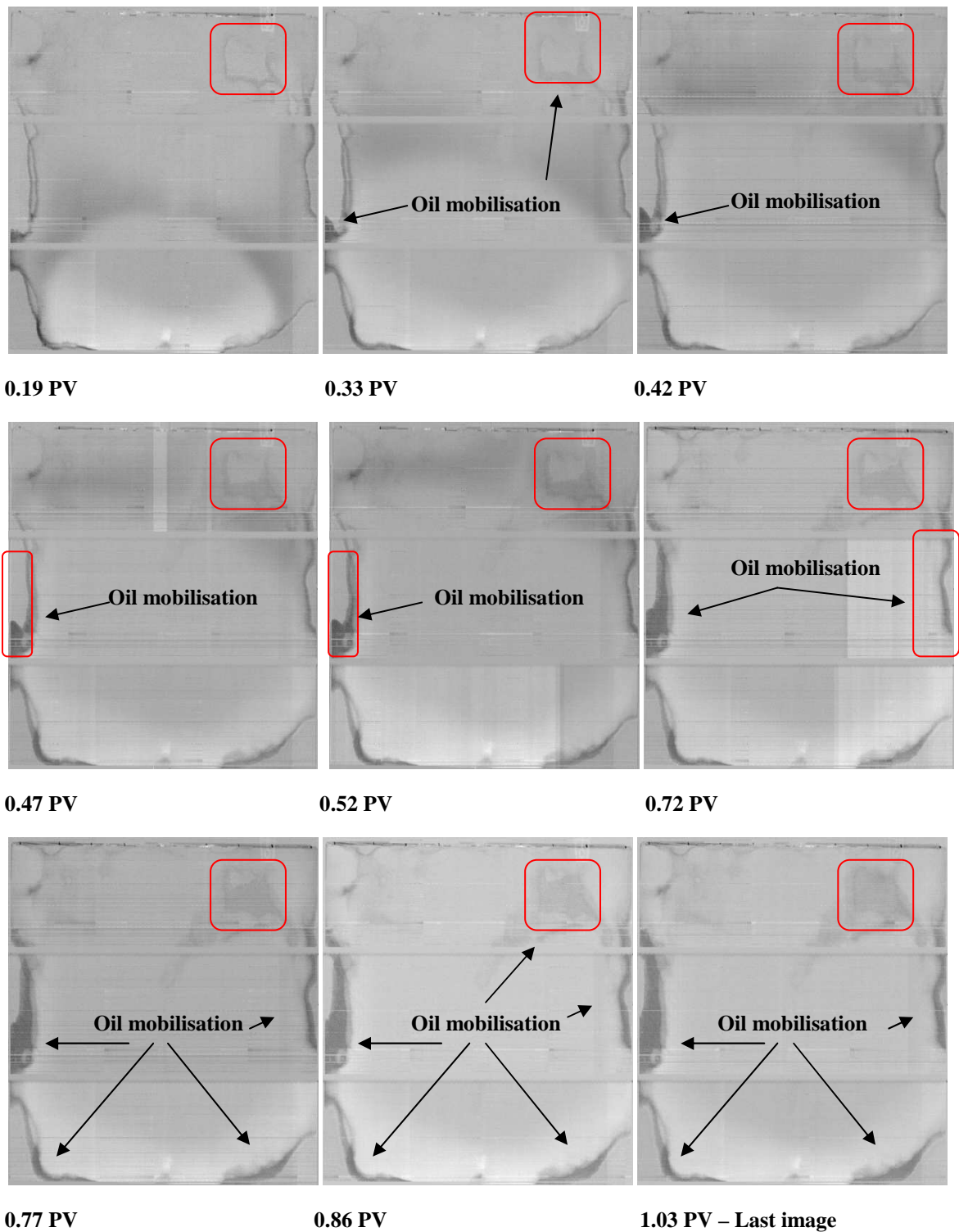


Figure 4.12 Polymer injection in the WF+PF sample at different PV.

From the images it is observed that the oil mobilisation happens mostly at the volumetric level, at both sides and some in the red square in the upper right corner (*Figure 4.12*). The effluent is collected in different sizes of measuring cylinders and analysed for viscosity. Viscosity is measured for each measuring cylinder and is shown in *Figure 4.13*.

The samples are displayed both at 10 s^{-1} and 100 s^{-1} to see the difference the shear rate do to viscosity measurement.

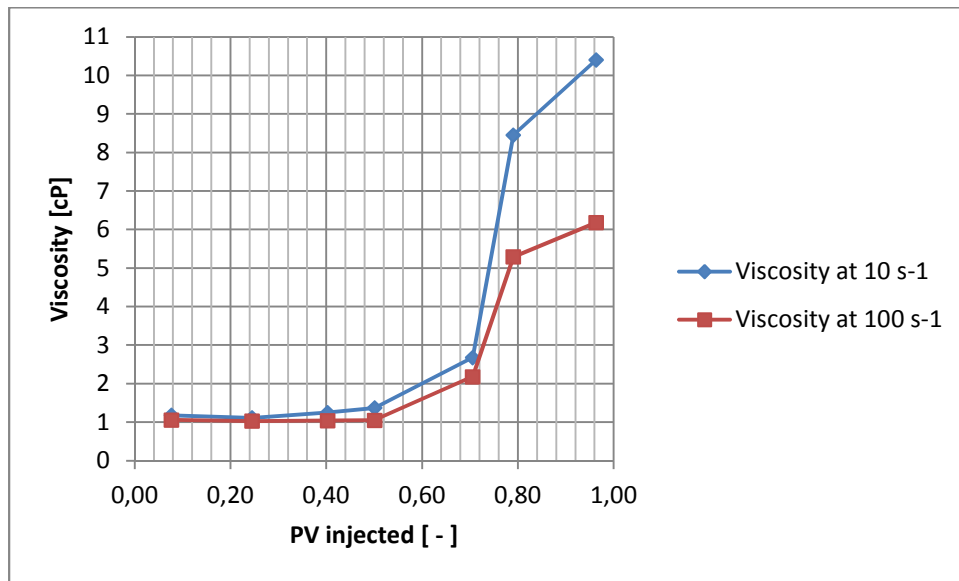


Figure 4.13 Viscosity measurement of effluent from polymer injection in WF+PF sample at different shear rates.

Somewhere between 0.50 PV and 0.71 PV the polymer front breaks through judging by the images and the effluent viscosity measurement (*Figure 4.13*). In the end of the injection the polymer solution viscosity is measured to be approximately 10.5 cP for the 10 s^{-1} measurement and 6 cP for the 100 s^{-1} measurement. Comparing original unused polymer with the produced polymer effluent, the difference is 1 cP , probably caused by shear rate and some water mixing into the polymer solution. The reduction is not of any large significance, which is typical for practical cases [77].

Comparing the effluent profile of the polymer injection with corresponding dispersion test for the sample may yield useful information about what kind of flow mechanisms the polymer is exposed to in the porous medium. When the polymer is injected into the sample it does not flow in the whole pore volume of the sample. The pore space occupied by oil has to be taken into consideration, which means that the pore volume where the polymer flows is the effective pore volume (PV_{eff}).

The effective pore volume is found by:

$$PV_{\text{eff}} = PV \cdot (1 - S_{\text{o,rem}}) \quad \text{Equation 4.1}$$

Effluent from the polymer injection together with the effluent dispersion test is normalized by the use of *Equation 3.2*, calibrated to effective pore volume and compared in the same graph (*Figure 4.14*).

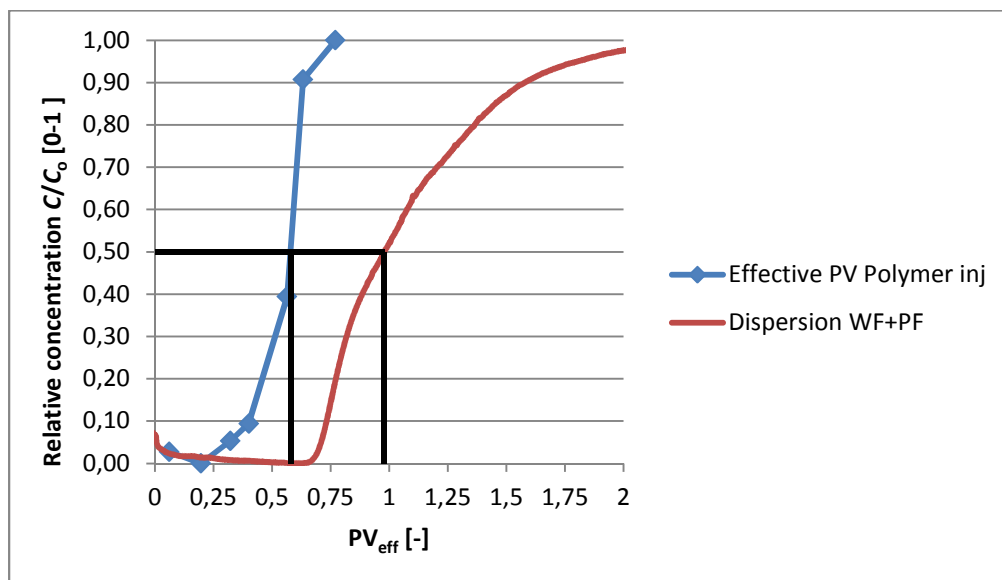


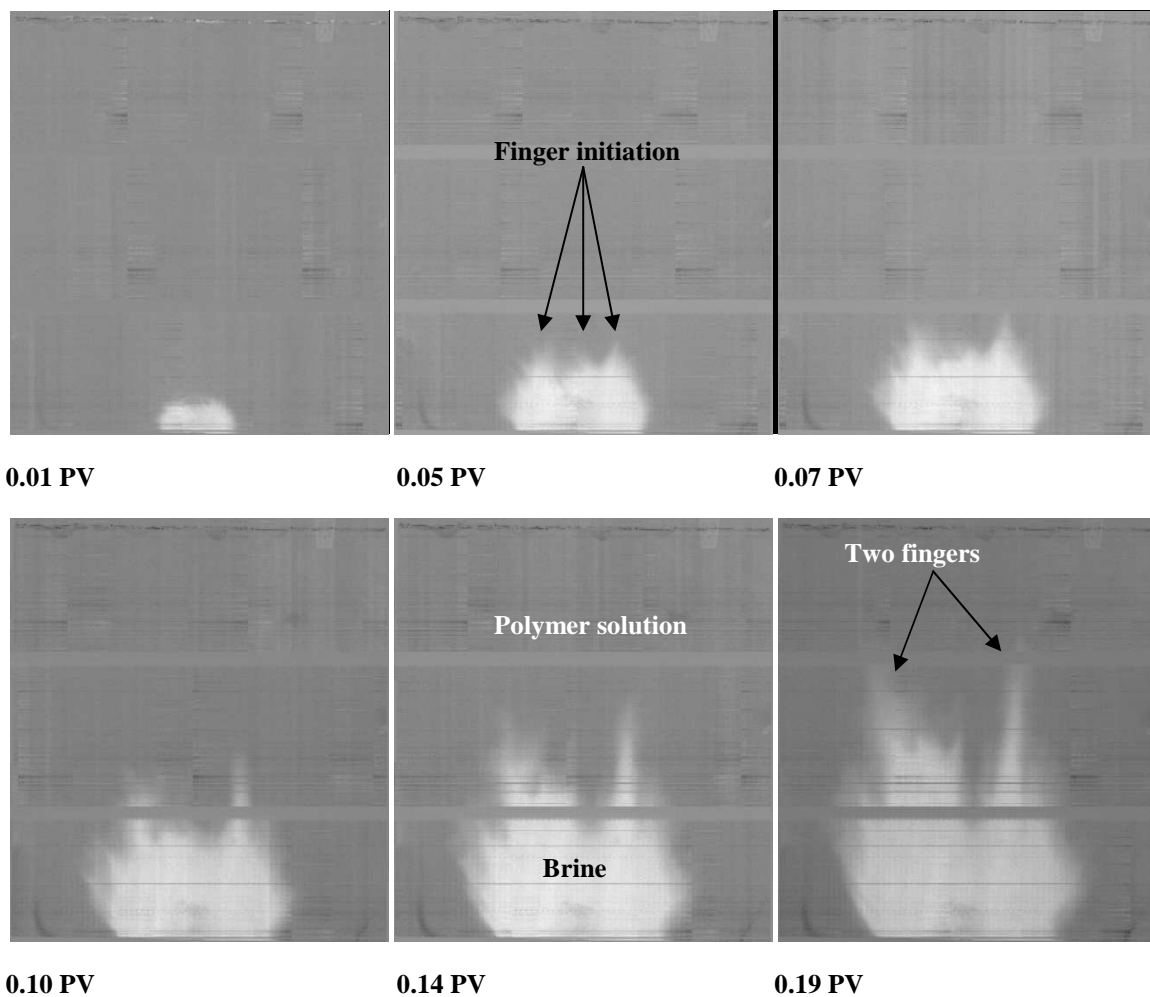
Figure 4.14 Comparison of polymer injection and effluent dispersion test.

From *Figure 4.14* it is observed that the polymer injection arrived earlier than the ideal dispersion displacement. Factors contributing to the early breakthrough are most possibly depleted layer and inaccessible pore volume (IPV) and the latter probably the most. Comparing the two individual displacements at 50% concentration it is possible to find the difference in *PV* injected (0.4 *PV* in difference). If only IPV contributed to the accelerated flow, it would be 40%. Similar values have been reported in sand packs with permeability of 12 D [78]. The acceleration is most likely caused by a combination of IPV and depleted layer effects.

4.2.3 Chase water injection

Chase water was flooded through the sample without being captured by image, and the slab had to be refilled with polymer and subsequently reinjected with chase water. The injection therefore starts at 4.1 PV instead of approximately 2.0 PV.

The viscosity ratio of the water/polymer displacement is approximately 1:11, hence an unstable miscible displacement in theory. In this experiment, retention has not been taken into consideration. However, it is vital to know the retention of full scale polymer injection to be able to save as much polymer as possible. When the polymer slug has been injected, water is injected to push the polymer slug through the reservoir. How the water will displace the polymer solution is visualised in *Figure 4.15*. To be able to see the water, brine is used instead of tracer. It will appear as white in the images because it has low attenuation compared to tracer. The injection rate is set to 1 mL/min.



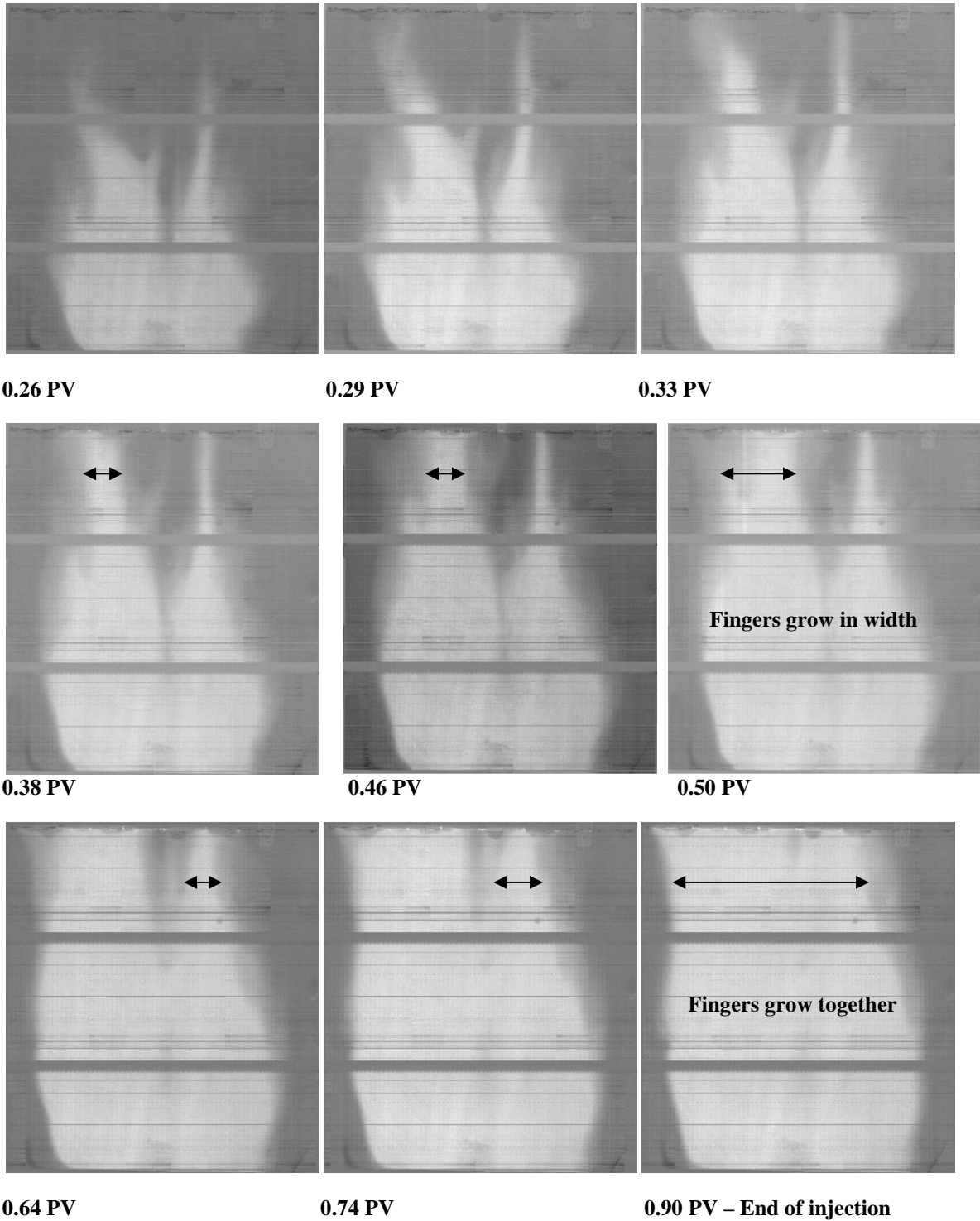


Figure 4.15 Chaser water injection in the WF+PF sample at different PV.

From all flooding performed in this sample before (dispersion, water injection and polymer injection), the clearly heterogeneity zone is seen in this experiment as well (*Figure 4.15*). This forces two distinct fingers to develop and follow the heterogeneity. After the breakthrough the fingers grow in width, which is an expected behaviour in a fingered system. A viscosity analysis of the effluent is shown in (*Figure 4.16*).

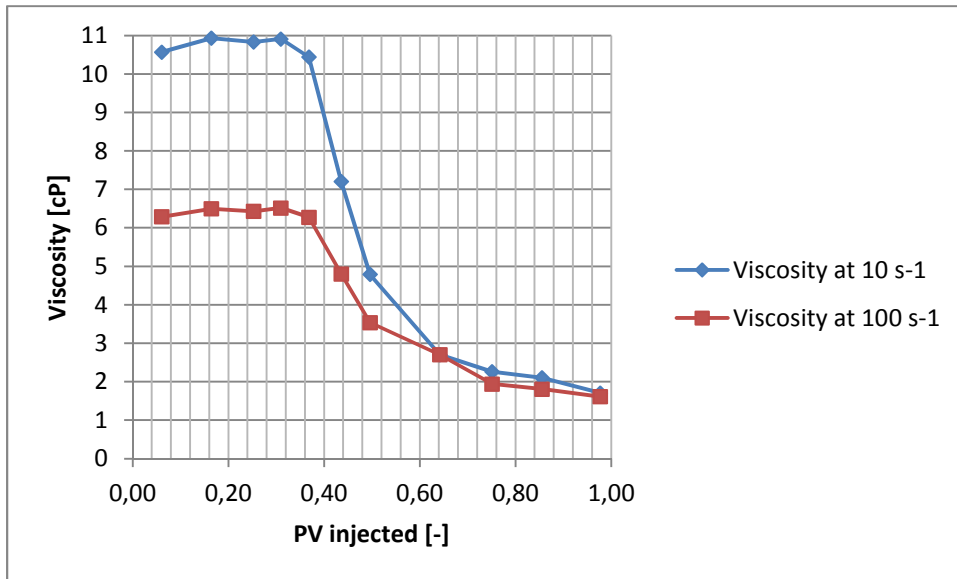


Figure 4.16 Viscosity measurement of effluent from chase water injection in the WF+PF sample.

From *Figure 4.16* it can be observed that the chase water front breaking through in the WF+PF sample just before 0.4 PV. The fingering of chase water through the polymer solution can present a problem. If the chase water fingers catch up with the polymer front, it will reduce the solution viscosity at the front and thus increase the mobility ratio between polymer and oil. In the end of the injection the viscosity is measured to be approximately 1.5 cP, which is just above water viscosity.

Comparing the effluent profile to an ideal situation, which is piston-like and no mechanisms retard or accelerate the displacement, can support the visual analysis of the displacement. Relative concentration and effective pore volume (*Equation 3.2 and Equation 4.1*) is accounted for.

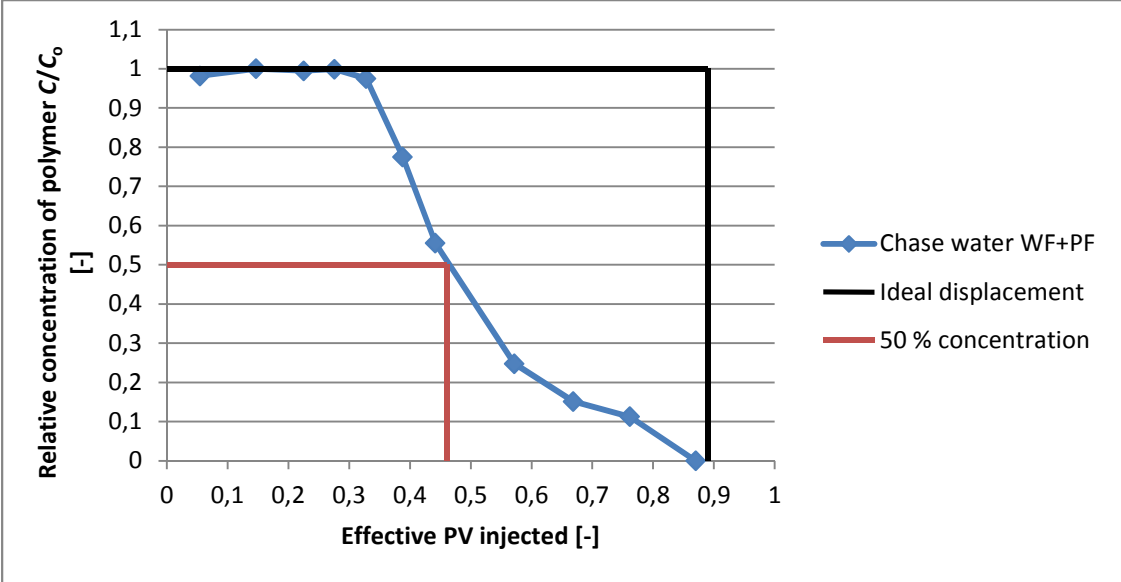


Figure 4.17 Comparison of chase water injection in the WF+PF sample to an ideal situation.

This chase water injection starts at 4.1 PV according to the production history, whereas *Figure 4.17* only regards this injection alone. It is observed that 50% concentration is reached by the chase water after 0.46 PV injected, 0.43 PV before an ideal displacement. This is a quantified measure of the degree of fingering which is quite pronounced during the chase water injection.

4.2.4 Recovery

Water injection:

The recovery for the different injections in the WF+PF sample are displayed and discussed in this chapter, where the water injection was the first main injection performed in this sample. The recovery efficiency and water-cut (WC) for the water injection is shown below in *Figure 4.18*.

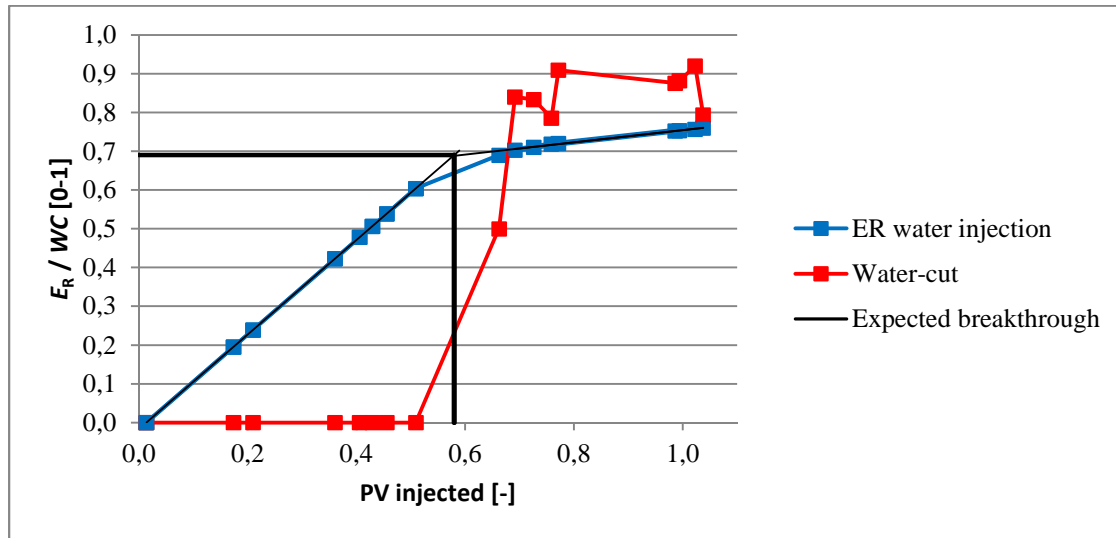


Figure 4.18 Recovery efficiency (E_R) and water-cut (WC) as a function of pore volume injected for water injection for the WF+PF sample.

Table 4.9 Observed values from water injection in the WF+PF sample.

Event	PV [-]	E_R [%]	Average WC [%]	$S_{o,rem}$ [%]
Breakthrough water	0.58	69.0	0	25.4
End of water injection	1.04	76.0	90	19.7

Water breakthrough (*Figure 4.9*) is estimated by linear trend lines to be at 0.58 PV . The capillary end-effect started at approximately 0.44 PV and it took 0.14 PV (10 hours) before the water saturation was high enough ($S_w(P_c=0)$) to escape the porous medium. Capillary end-effects support the argument that the sample is not strongly water-wet. The water injection was stopped when a WC of 90% was reached at 1.04 PV and the recovery was calculated by material balance to be 76%. This can be described as a relatively high recovery for water injection. The most likely reason for the high recovery is that the permeability is high and therefore the capillary forces low, in addition to a change in wettability towards intermediate-wet. The remaining oil saturation ($S_{o,rem}$) is calculated to be 19.7%.

Polymer injection:

The production characteristics for the polymer injection are shown in *Figure 4.19*.

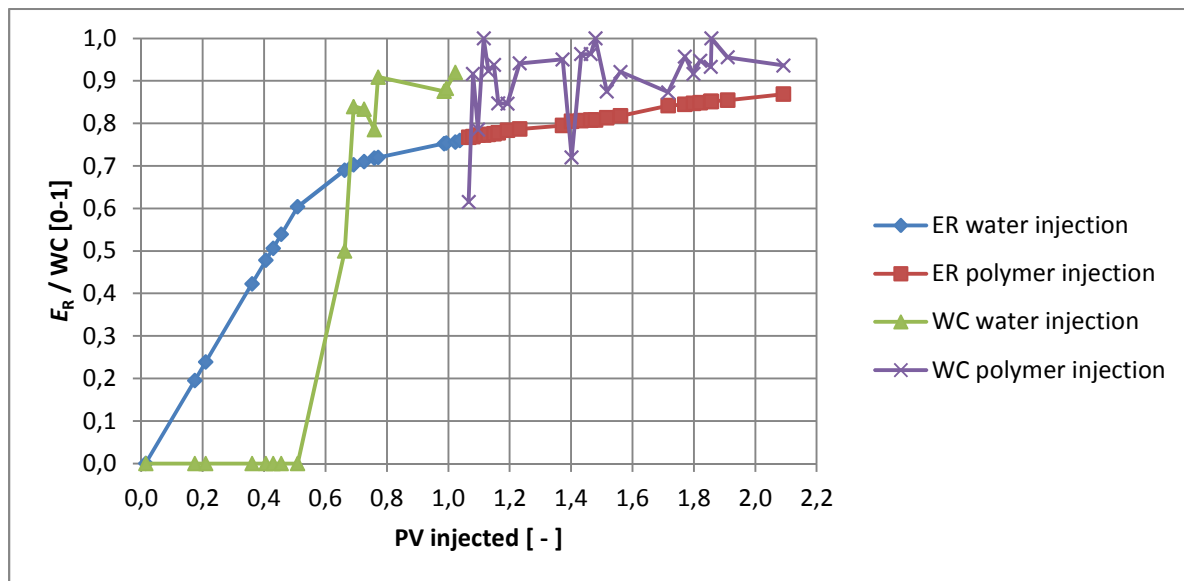


Figure 4.19 Recovery efficiency (E_R) and water-cut (WC) as a function of pore volume injected for water injection and polymer injection in the WF+PF sample.

Table 4.10 Observed values from polymer injection in the WF+PF sample.

Event	PV [-]	E_R [%]	Average WC [%]	$S_{o,rem}$ [%]
Water injection	1.04	76.0	90.0	19.7
Polymer injection, end	2.09	86.9	90.5	10.8
Difference	1.05	10.9	0.50	8.9

During the polymer injection the recovery efficiency is increased from 76.0% to 86.9%. This is an increase of 10.9%. There was no build up of an oil bank, simply continuous production. The slope of the polymer injection is the same as of the water injection and can be an indication that the same recovery would be obtained by a continuous water injection. However, the WC is kept constant at about 90.0% and it is impossible to exclude the polymer effect. The remaining oil saturation is calculated to 8.9% after the polymer injection.

From observations of the images, the polymer seems to affect the sweep efficiency the most and the microscopic efficiency not so much. With a remaining oil saturation of 19.7% after water injection, which is considered to be in the lower range, residual oil mobilising is not so pronounced as Kamaraj *et.al* [9] described.

Chase water injection:

The total production and water-cut for all injections are presented in *Figure 4.20*. The reason for all the curves are that the first chase water injection was not captured by image and a new portion of polymer solution had to be injected into the sample before performing the visualised chase water injection.

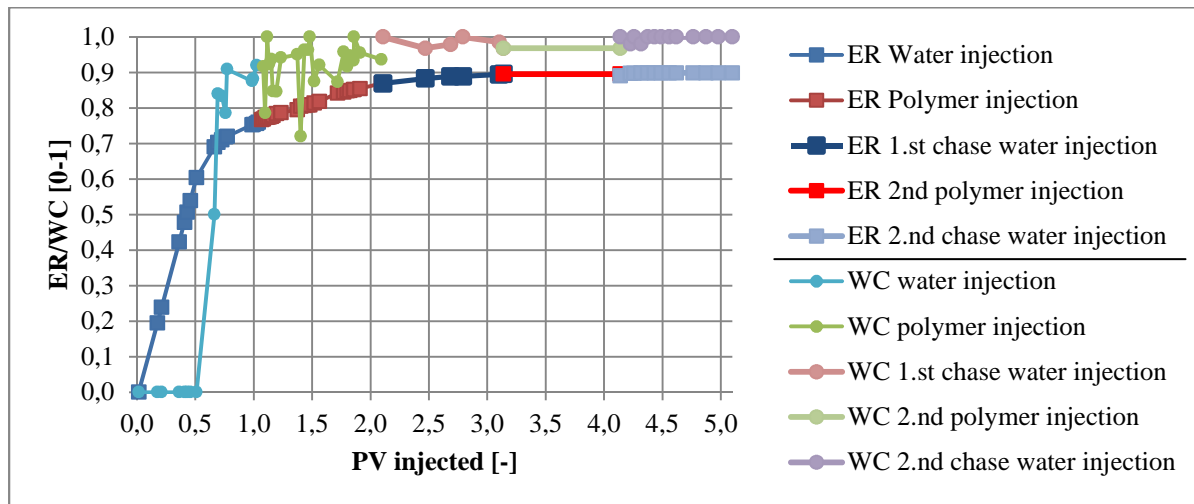


Figure 4.20 Recovery efficiency (E_R) and water-cut (WC) as a function of pore volume injected for water, polymer and chase water injection in the WF+PF sample.

Table 4.11 Observed values from chase water injection in the WF+PF sample.

Event	PV [-]	E_R [%]	Average WC [%]	$S_{o,rem}$ [%]
Polymer injection, end	2.09	86.9	90.5	10.7
1.st chase water injection, end	3.14	89.8	99.0	8.3
Difference	1.05	2.90	8.50	2.4

The first chase water injection produces 2.9% additional oil (*Table 4.11*) and the second chase water injection is the one which can be viewed in (*Figure 4.15*). A large factor for increased oil recovery, is most likely due to oil which was mobile during the polymer injection and is simply pushed through to the producer by chase water. It is also a chance that the oil is mobilised during the chase water injection, because the chase water displaces the polymer solution. The injection rate of the chase water is ten times higher than during the polymer injection, and could possibly contribute to the recovery. A final recovery of 90% is obtained after 3.1 PV of water, polymer and chase water injection. The average water cut is 99% during the chase water injection, and the remaining oil saturation is calculated to be 8.3%. No additional oil was produced during the secondary polymer- and chase water injection, which means that a final displacement efficiency was already reached.

4.2.5 Overall discussion WF+ PF sample

The WF+PF sample was exposed to a primary water injection, a secondary polymer injection and a chase water injection. The water injection did not yield as much fingering as expected. The fingering had similarities to numerical simulations performed by Riaz and Tchelepi [76], where instabilities in front was followed by Buckley-Leverett shock. Two distinct fingers developed in the early stage of the water injection, but as time went on they grew together. A capillary end-effect was observed between 0.44 *PV* and 0.58 *PV*, and at the water breakthrough the recovery was estimated to be 69.0%. The final recovery after 1.04 *PV* injected water was approximately 76.0%, with an average *WC* of 90.0%. Main reasons for the high recovery may be large pore throats (i.e. high permeability) which lead to low capillary pressure in addition to a changed wettability from strongly water-wet.

The polymer injection gave an additional recovery of 11%, mostly due to volumetric sweep. The remaining oil saturation was calculated to be 20% at the end oil the water injection and *WC* average was 90.5% throughout the entire injection.

Chase water injection showed miscible unstable fingering between the chase water and polymer solution. An additional 2.9% of oil was produced during the first chase water injection and the average *WC* was 99% in both chase water injections.

Table 4.12 Summary of injections in the WF+PF sample.

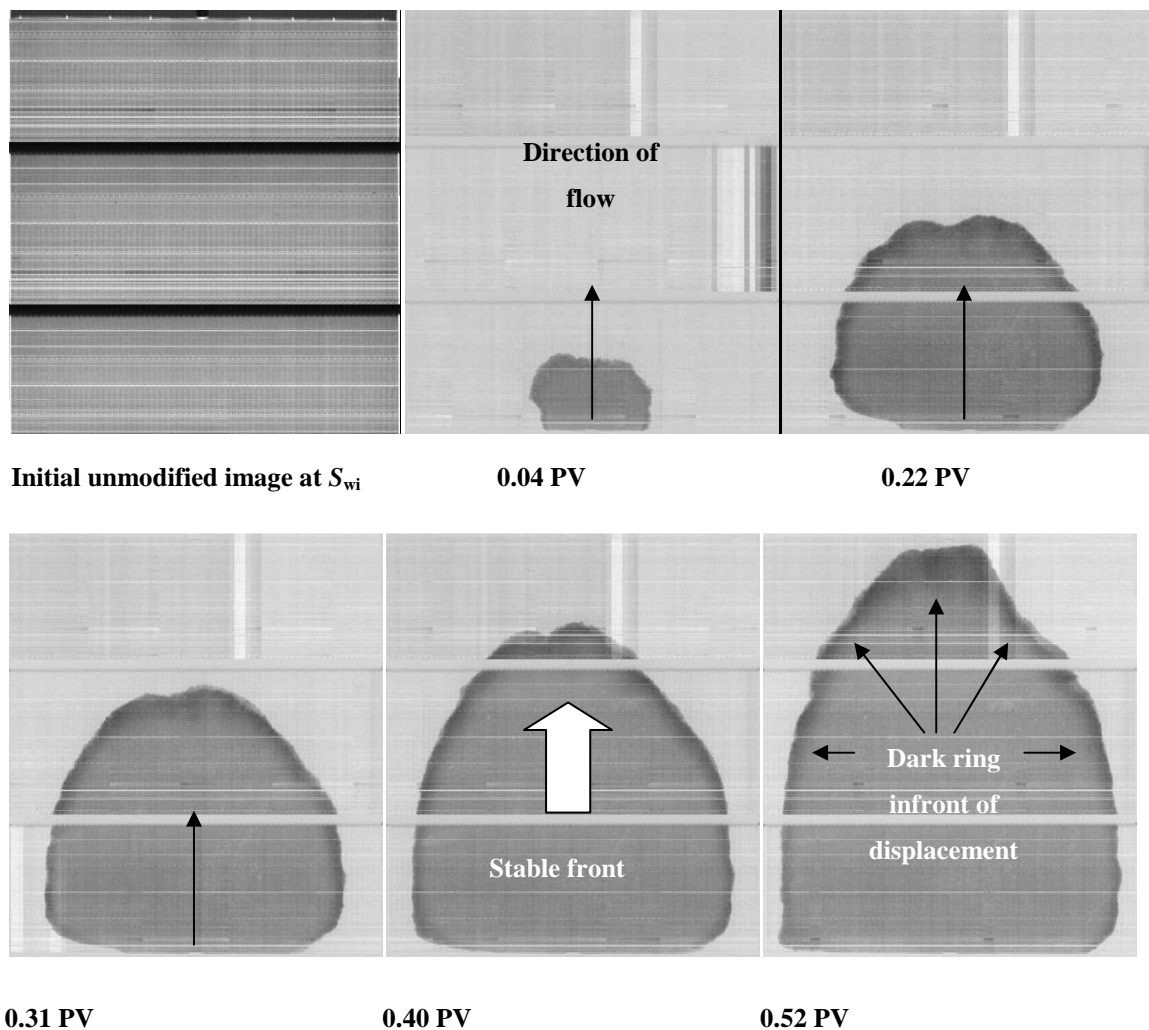
Event	<i>PV</i> [-]	<i>E_R</i> [%]	<i>WC</i> average [%]	<i>S_{o,rem}</i> [%]
Water breakthrough	0.58	69.0	0.00	25.4
Water injection, end	1.04	76.0	90.0	19.7
Polymer injection, end	2.09	86.9	90.5	10.8
1. st chase water injection, end	3.14	89.8	99.0	8.3

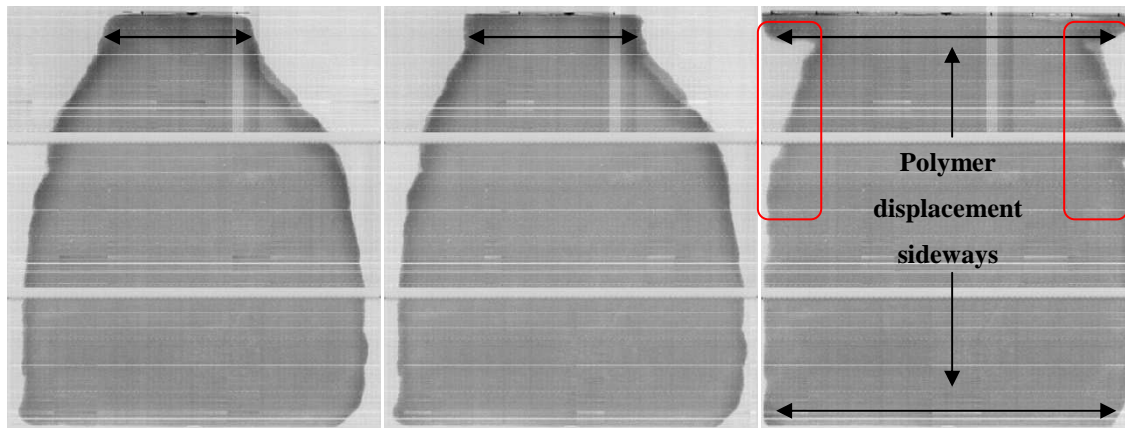
4.3 The polymer flooding sample (PF)

The PF sample is going to be exposed to a primary polymer injection and subsequently by a chase water injection. Comparisons to the WF+PF sample is made later in this thesis (*Chapter 4.4*). All further injections are made from the lower injection point.

4.3.1 Direct polymer injection

The viscosity ratio during the immiscible polymer/oil displacement is approximately 11:53. This is an unstable displacement, but more favourable than the water injection case. Injection rate is set 0.1 mL/min, and the direct polymer injection is shown in *Figure 4.21*.





0.56 PV

0.62 PV

0.99 PV – End of PF

Figure 4.21 Polymer injection in the PF sample at different *PV*.

The direct polymer injection (*Figure 4.21*) seems like quite a stable immiscible displacement, which is opposite of the expected. If we look at the image at 0.52 *PV* it has a coning shape towards the producing side. After the breakthrough, which occurs at 0.61 *PV*, the polymer front stretches in width and sweep oil in the corners at 0.56 *PV*, 0.62 *PV* and 0.99 *PV* in *Figure 4.21*. The unswept may be recovered by the chase water injection (Chase water injection, Chapter 4.3.2).

Throughout nearly all images it is observed a dark ring around the front. During the polymer injection at the WF+PF sample a similar scenario appeared and it might be a bank of connate water in front of the polymer solution. Such effect is illustrated schematically in *Figure 4.22*.

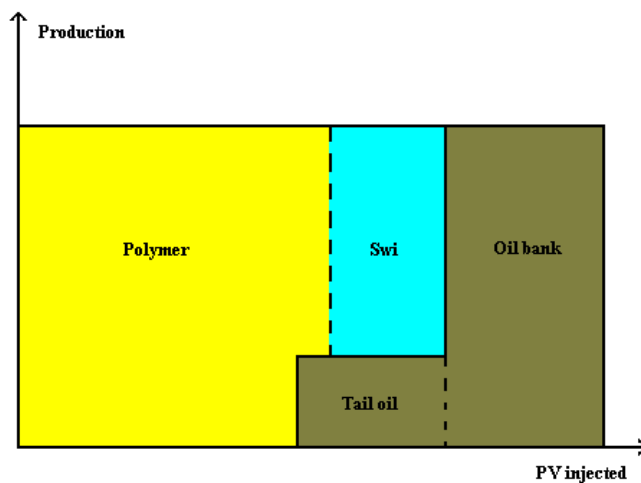


Figure 4.22 Schematic of direct polymer injection and potential connate water bank (S_{wi}).

If the observed darker ring (*Figure 4.21*) was connate water of the irreducible water saturation (18.6% of total *PV*) it would correspond to a volume of approximately 80 mL. However, if 80 mL of water was pushed in front of the polymer injection the viscosity would drop more significantly (0.67 *PV* at *Figure 4.23*). The effluent from the direct polymer injection is collected and viscosity is measured, and the result is shown in *Figure 4.23*. Viscosity is quite stable during the polymer injections, which is to be expected if no connate water banking is the case. The darker ring is investigated more thoroughly under *Chapter 4.5*.

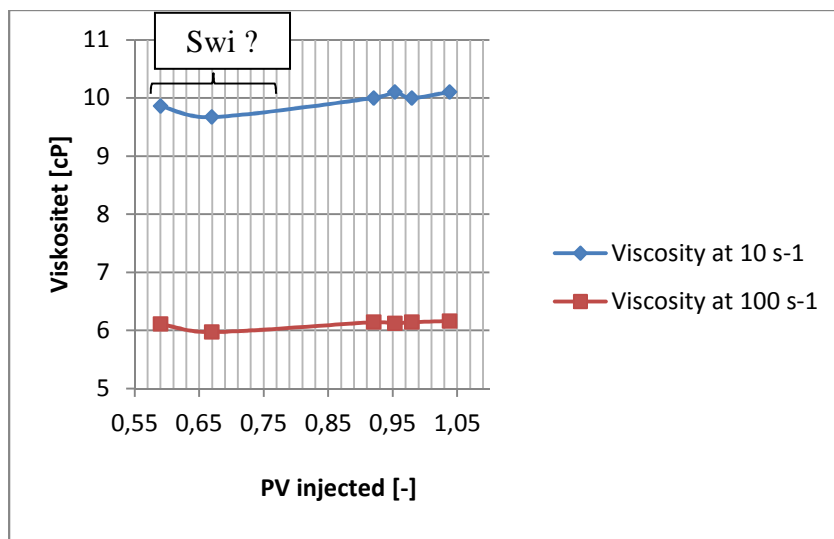
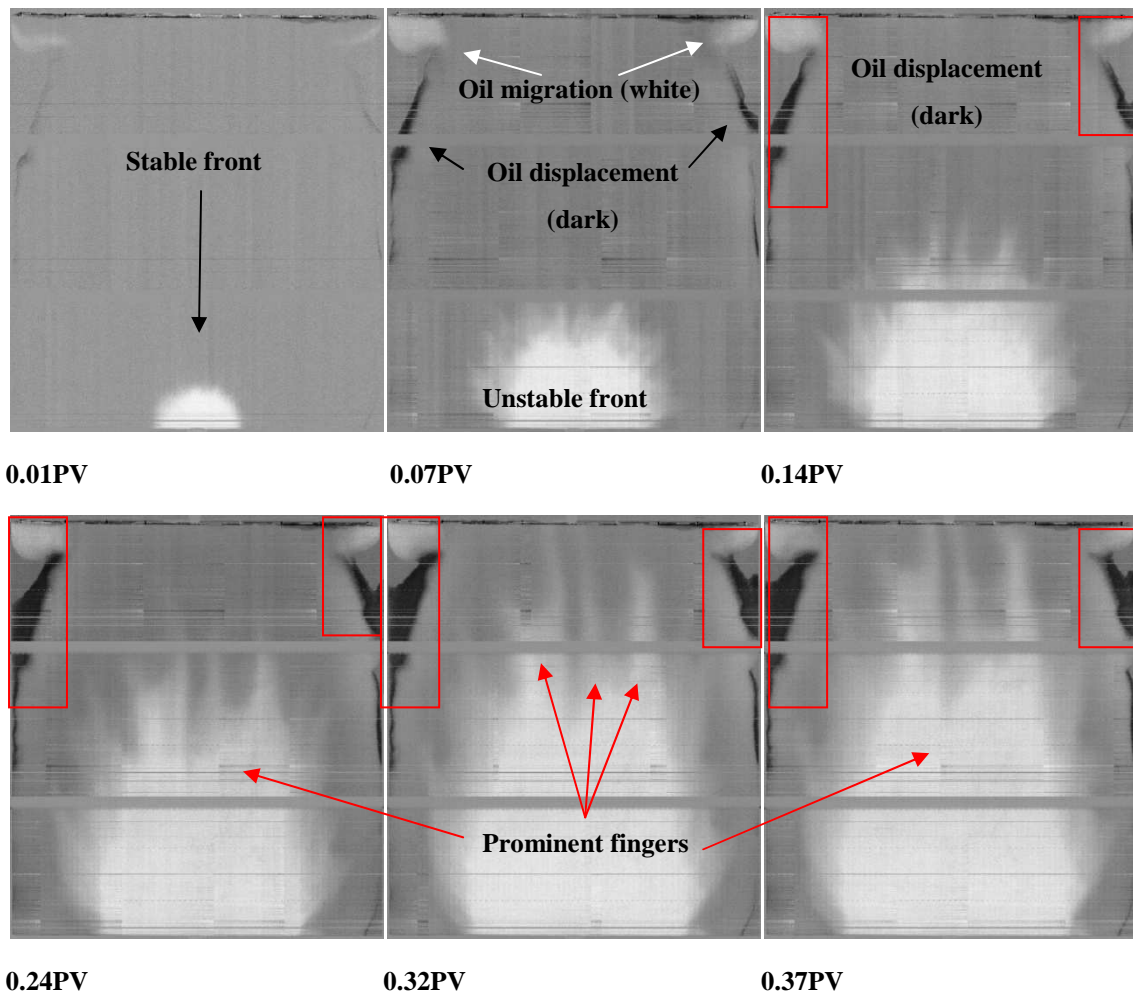
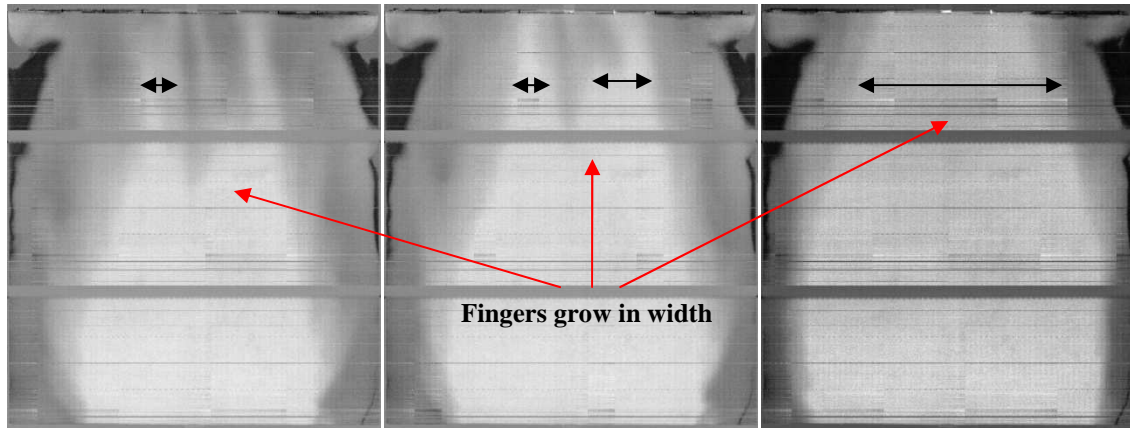


Figure 4.23 Viscosity measurement of effluent from polymer injection in PF sample at different shear rates.

4.3.2 Chase water injection

A chase water injection is performed. The viscosity rate of the miscible water/polymer displacement is approximately 1:11, and is accordingly an unstable displacement. The injection rate is set to 1 mL/min. Brine is used as chase water, and will appear as white (i.e. low attenuation). The chase water injection in the PF sample is visualised below in *Figure 4.24*.





0.40PV

0.50PV

0.89PV – End of injection

Figure 4.24 Chaser water injection PF sample at different *PV*.

The images in *Figure 4.24* show unstable miscible fingering between polymer solution and injected chase water (brine) and after breakthrough the fingers grow in width. At 0.07 *PV* in *Figure 4.24*, one can observe the flow of polymer (dark area) and the flow of oil (upper white area at the 0.07 *PV* image). It seems as if the whole sample has been swept from the last image.

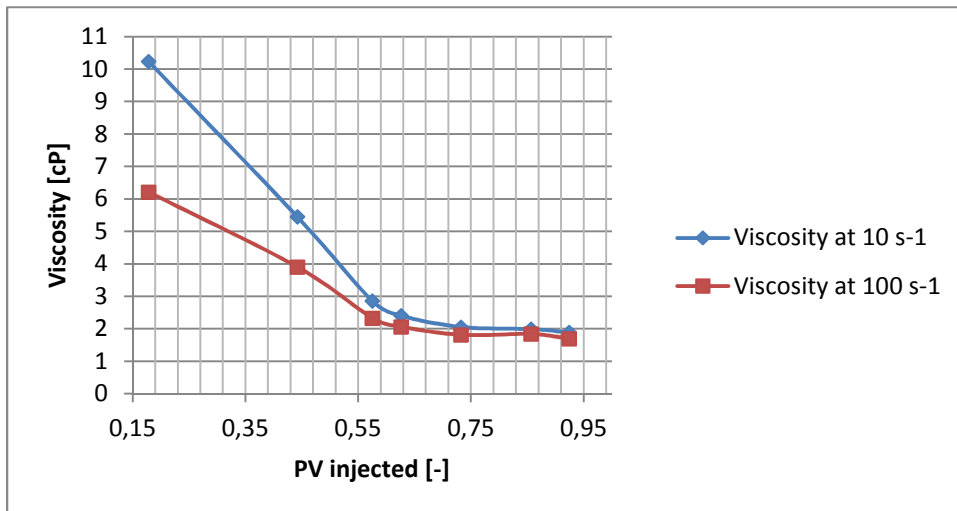


Figure 4.25 Viscosity measurement of effluent from chase water injection from PF sample at different shear rates.

A misunderstanding lead to the use of too large measuring cylinders to collect the effluent in this experiment, and it is difficult to observe the breakthrough of chase water. Looking at *Figure 4.25*, it can be assumed that the breakthrough happens somewhere between 0.18 *PV* and 0.44 *PV*. A better estimation of the breakthrough is made by observing images in *Figure 4.24*, more specific at 0.37 *PV* which seems like the timing of the breakthrough. It corresponds more or less to the breakthrough of chase water in the WF+PF sample (0.41 *PV*), which can be expected due to the similarities of the two core samples.

A comparison of the effluent profile to an ideal piston displacement is shown in *Figure 4.26*, where relative concentration and effective pore volume (*Equation 3.2 and 4.1*) has been taken into consideration. According to production history the injection starts at approximately 1 PV, whereas in this figure it is treated alone. It is observed that the 50% concentration is reached at about 0.44 PV, which is 0.47 PV before an ideal displacement. This shows that there is a large degree of fingering during the chase water injection, which corresponds to the images.

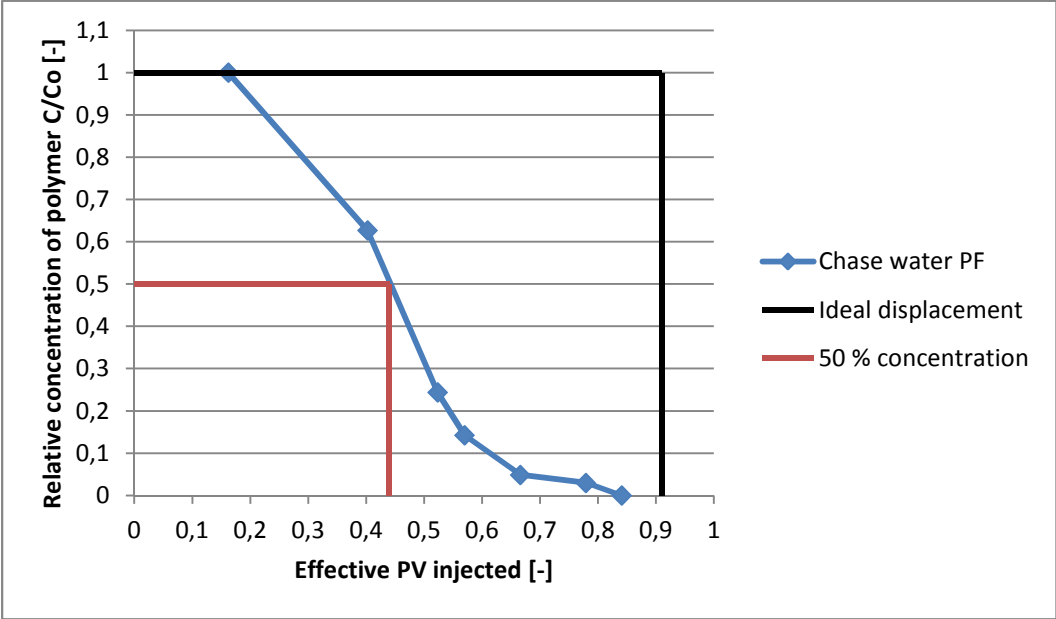


Figure 4.26 Comparison effluent chase water injection in the PF sample to an ideal situation.

4.3.3 Recovery

Primary polymer injection:

The recovery for the different injections in the PF sample are displayed and discussed in this chapter, where the polymer injection was the first injection. Recovery efficiency and water-cut (WC – actually polymer-cut in this case) for the direct polymer injection is shown in *Figure 4.27*.

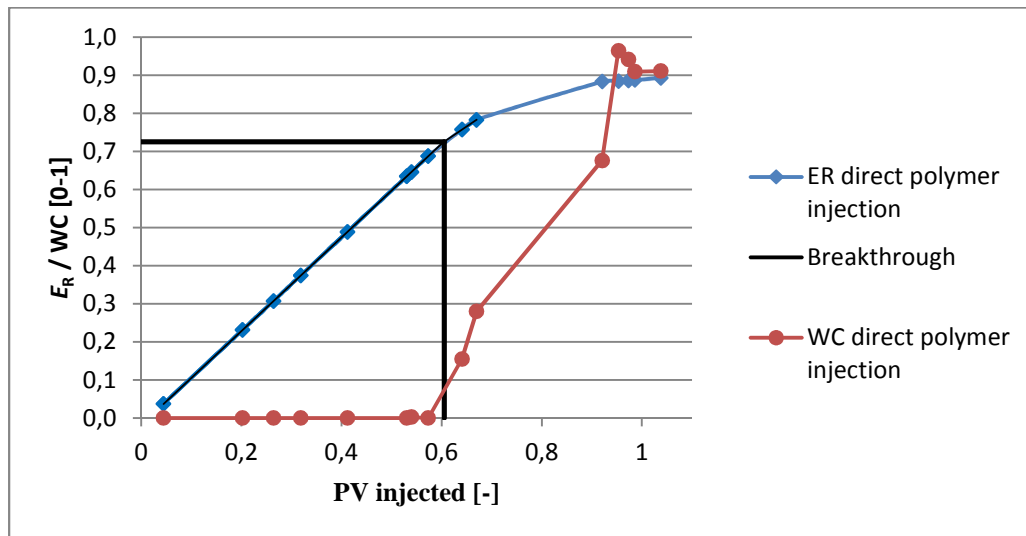


Figure 4.27 Recovery efficiency (E_R) and water-cut (WC) as a function of pore volume injected for direct polymer injection in the PF sample.

Table 4.13 Observed values from polymer injection in the PF sample.

Event	PV [-]	E_R [%]	WC average [%]	$S_{o,rem}$ [%]
Breakthrough of polymer	0.61	72.5	0.00	22.3
Direct polymer injection, end	1.04	89.3	88.0	8.7

Table 4.13 show observed values from *Figure 4.27*. Polymer breakthrough, estimated by linear trend lines, occurs at 0.61 PV with a respective recovery efficiency of 72.5%. When the WC reaches 90% the injection is stopped. The amount of fluid injected at that stage was 1.04 PV , and the recovery efficiency was calculated by material balance to be 89.3%. This recovery efficiency is quite high, and the remaining oil saturation at the end of the polymer injection is calculated to be 8.7% and might also indicate a change in wettability towards intermediate-wet.

Chase water injection:

The total production and water-cut for the different methods are presented in *Figure 4.28*.

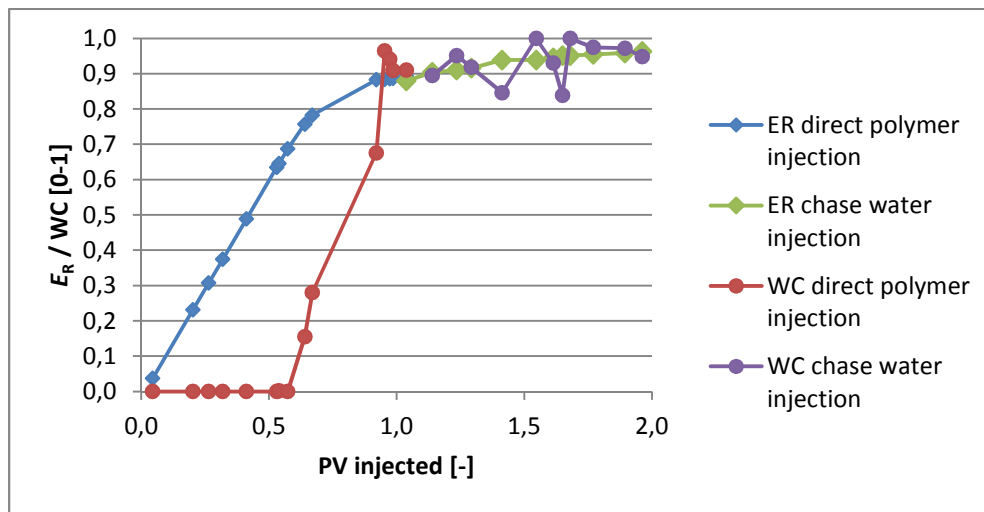


Figure 4.28 Recovery efficiency (E_R) and water-cut (WC) as a function of pore volume injected for direct polymer injection and chase water injection in the PF sample.

Table 4.14 Observed values from the chase water injection in the PF sample.

Event	PV [-]	E_R [%]	WC average [%]	$S_{o,rem}$ [%]
Direct polymer injection, end	1.04	89.3	88.0	8.7
Chase water injection, end	1.96	96.3	93.4	3.0
Difference	0.92	7.0	5.4	5.7

The chase water injection, with duration of 0.92 PV , produces some additional oil (*Table 4.14*). Like in the WF+PF sample, the chase water pushes the polymer through the PF sample and hence the polymer can intrude in the unswept zones. The injection rate is 10 mL/min, which is ten times higher than for the polymer injection and might affect the recovery. During the chase water injection the recovery efficiency increases from 89.3% to 96.3%, a 7% increase and a very high final recovery rate. The WC average is approximately 93.4% during the whole injection sequence. Remaining oil saturation is reduced to 3%, a difference of 6% from the polymer injection, which most probably can be referred as residual oil due to the high sweep efficiency seen from *Figure 4.21* and *Figure 4.24*.

4.3.4 Overall discussion PF sample

The PF sample was exposed to a primary polymer injection and a chase water injection. As expected, the immiscible polymer injection was more stable than the primary water injection in the WF+PF sample. However, it was still an unstable injection due to the viscosity ratio (11:53). When the polymer front reached the end of the sample, it stretched in width and produced more oil. At breakthrough the recovery was estimated by linear trend lines to be 72.5%. Final recovery after polymer injection was 89.3% and *WC* was 90.5% in the end.

Chase water injection revealed miscible fingering between the brine and polymer solution. It was approximated by the use of the images, due to the lack more and smaller samples, that the breakthrough of chase water occurred around 0.37 *PV*. An additional 7% of oil was produced and *WC* average was 93.4%. The reason for such a high final recovery is most likely due to high permeability which leads to low capillary forces in combination with a more favourable mobility ratio than during the water injection in the WF+PF sample. A change in wettability from strongly water-wet might also contribute to an increase in the recovery. The remaining oil saturation is 3%, and can be referred to as residual oil saturation due to very good sweep efficiency. All observed values from all the injections in the PF sample are shown in *Table 4.15*.

Table 4.15 Summary of observed values from injections in the PF sample.

Event	<i>PV</i> [-]	<i>E_R</i> [%]	<i>WC</i> average [%]	<i>S_{o,rem}</i> [%]
Breakthrough of polymer	0.61	72.5	0	22.3
Direct polymer injection, end	1.04	89.3	88.0	8.7
Chase water injection, end	1.96	96.3	93.4	3.0
Difference, polymer and chase	0.92	7.0	-	6.0

4.4 Comparison and summary of results

Comparing the results from both samples is vital to try explaining the difference of a secondary polymer injection to a primary polymer injection. The recovery efficiency for both samples is shown in *Figure 4.29*.

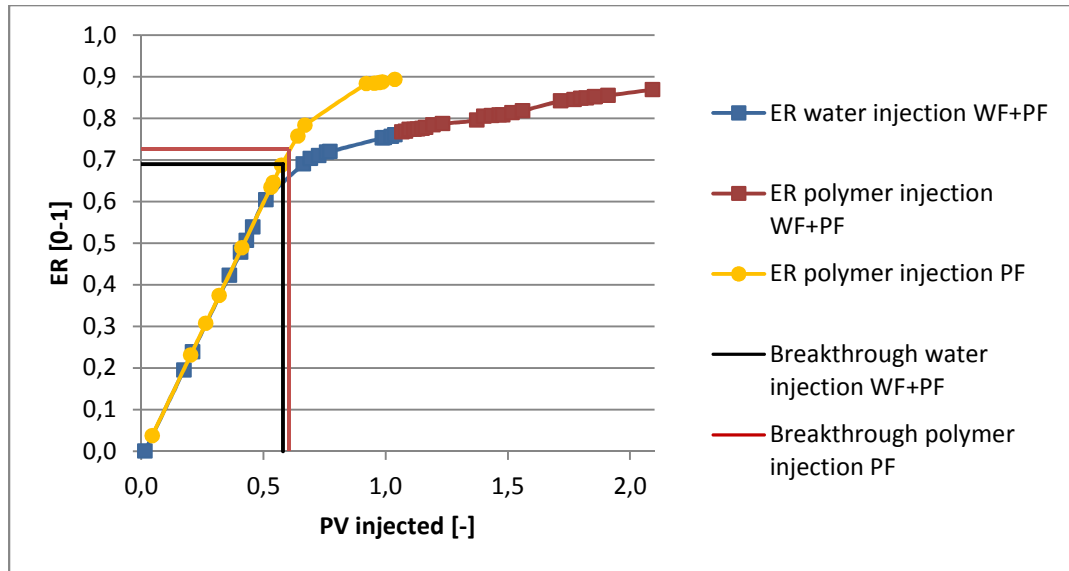


Figure 4.29 Recovery efficiency as a function of pore volume injected for all the injections in the WF+PF and PF sample.

The main difference in the polymer injection directly in the PF sample, compared to the polymer injection in the WF+PF sample is that the recovery is accelerated (*Figure 4.29*). The difference is roughly 1 *PV* injected to obtain the same recovery in the WF+PF sample compared to the PF sample. Observed values and differences from different injection are shown in *Table 4.16-Table 4.18*.

Table 4.16 Observed values in breakthroughs between the WF+PF and PF sample.

Event	<i>PV</i> [-]	E_R [%]	$S_{o,rem}$ [%]
BT water injection WF+PF	0.58	69.0	25.4
BT polymer injection PF	0.61	72.5	22.3
Difference BT`s	0.03	3.5	3.1

The production of oil for both samples (*Table 4.16*) can be compared. Although the water injection in the WF+PF sample is very efficient, it is observed a difference from the PF sample. Breakthrough (BT) of water occurs at 0.58 *PV* and polymer BT occurs at 0.61 *PV*.

The polymer injection delays the BT compared to the water injection which affects the recovery efficiency. A delay of 0.03 *PV* corresponds to 3.5% additional oil. The delay due to the polymer injection most likely occurs because of a better mobility ratio between oil and polymer solution, and thus a better displacement.

Table 4.17 Comparison of the first injections in both samples from Figure 4.29.

Event	<i>PV</i> [-]	E_R [%]	WC average [%]	$S_{o,rem}$ [%]
Water injection WF+PF, end	1.04	76.0	90.0	19.7
Direct polymer injection PF, end	1.04	89.3	88.0	8.7
Difference	0	13.3	2.0	11.0

From *Table 4.17* it can be observed that the direct polymer injection is the PF sample recovers 13.3% more oil than the water injection. The residual oil saturation is reduced by 11% more with the direct polymer injection. The polymer injection is more stable compared to the water injection, probably due to a better mobility ratio between oil and polymer solution, which also yield a better recovery.

Table 4.18 Comparisons of the polymer injections from Figure 4.29.

Event	<i>PV</i> [-]	E_R [%]	WC average [%]	$S_{o,rem}$ [%]
Direct polymer injection PF, end	1.04	89.3	88.0	8.7
Polymer injection WF+PF	2.09	86.9	90.5	10.7
Difference	1.05	2.4	2.5	3.0

From *Table 4.18* one can see the difference between the two polymer injections. The direct polymer injection in the PF sample yields a better recovery. This is most likely because applying polymer as a primary injection will give a more favourable displacement from the start, while the WF+PF sample already has been flooded by water when applying the polymer. Hence, a better start yields a better final recovery.

4.5 Concentration and residual oil saturation

WF+PF sample:

As pointed out in *Figure 4.12* at 0.06 *PV*, the polymer injection seem like it is of a different concentration than of the resident water. The resident water has the same concentration as the injected polymer, so there should not be any difference. Some investigations must be done to clarify this phenomenon. It must be checked if the injected fluid displaces an area equal to the volume injected. By concluding that the correct area/volume ratio is observed, it proves that the dark ring observed in both samples is a true description of the displacement.

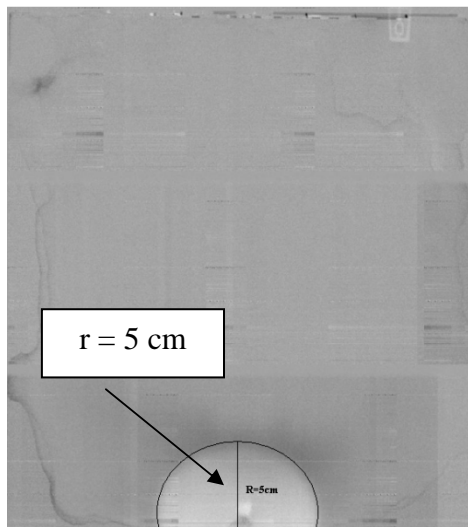


Figure 4.30 Area check of polymer injection at 0.04 *PV* in WF+PF sample.

As can be seen from *Figure 4.30*, the injected polymer has a radius of 5 cm. By calculation, the area of the injection is 4.36% of the total area of the slab. It corresponds approximately to the injected volume which is 4% of 1 *PV*. However, the radius is measured manually and is a large source of potential error. By changing the radius by ± 0.5 cm it affects the area by $\pm 20\%$. One has to assume that the measured radius is within the error limit. The area has also been checked for 0.088, 0.12 and 0.19 *PV* in *Figure 4.12* and they all correspond approximately with the area. It may be concluded that the area displacement of the injection is approximately equal to the *PV* injected.

Checking the collected effluent samples from the different injections with X-ray imaging and gamma-ray counts might determine if there is a different concentration. 100 mL measuring cylinders are used (*Figure 4.31*) for these tests.

It is important when checking the count rates for each cylinder, that the conditions are the same (i.e. the size of measuring cylinders and position is the same). A small shelf is mounted inside the 2-D cabinet which assures the same position for each cylinder.

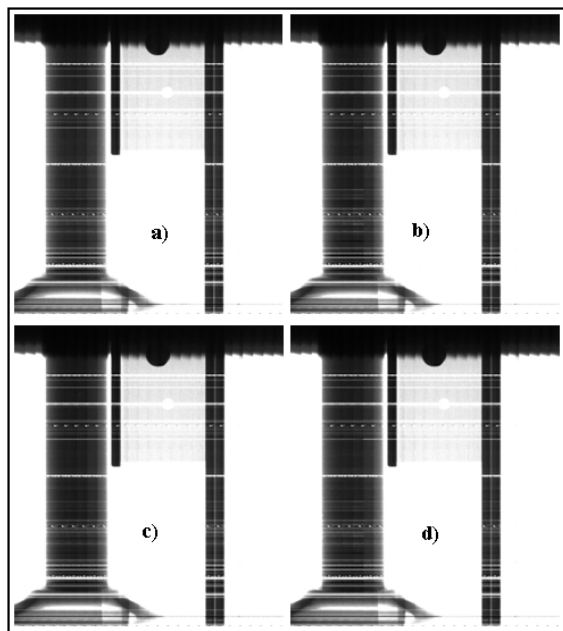


Figure 4.31 X-ray images of different measuring cylinders containing; a) Original polymer solution. b) Effluent water injection from the WF+PF sample. c) Effluent polymer injection from the PF sample. d) Effluent polymer injection from the WF+PF sample.

The images of the different measuring cylinder (*Figure 4.31*) are, by the intensity of contrast, exactly the same. If the eye cannot see the difference, a gamma count test might. All four cylinders were checked by gamma-ray at four specific points on the cylinder. An average value for each cylinder is shown in *Table 4.19*.

Table 4.19 Average gamma radiation count values for effluent samples (*Figure 4.31*).

Sample	Content	Gamma count rate[cps]
a	Unused polymer	158 ± 1
b	Effluent water injection WF+PF sample	169 ± 1
c	Effluent polymer injection PF sample	153 ± 1
d	Effluent polymer injection WF+PF sample	163 ± 1

By looking at *Table 4.19* one can see that the values are quite similar. Note that low values corresponds to a high attenuation, i.e. less counts per seconds (cps) and hence a lower radiation.

The lowest value (c), containing effluent polymer from the PF sample measured 16 counts per second less than the highest (b), containing effluent water from the WF+PF sample. One would expect the lowest value from clean water (sodium iodide). A difference of 16 cps, between those extremes, may be regarded as negligible. These two tests show no significant difference in effluent concentration.

A third option is to use MATLAB to check the count rates in the image pixels. A certain pixel value is associated with a certain concentration of sodium iodide. The images used in the results are drawn from an initial image, and the only thing which is displayed is the difference. To get the real values from pixels, an original image must be used to investigate the count values. The image which has been checked is shown in *Figure 4.32*.

By using MATLAB it is possible to check different areas of images to see what the average pixel value is. A simple code is written in MATLAB to retrieve an average value for a specified area. The different areas investigated are found by using Image Tool in MATLAB to locate the coordinates. Once the area is known, the code can run and an average value pops up automatically when the run is completed.

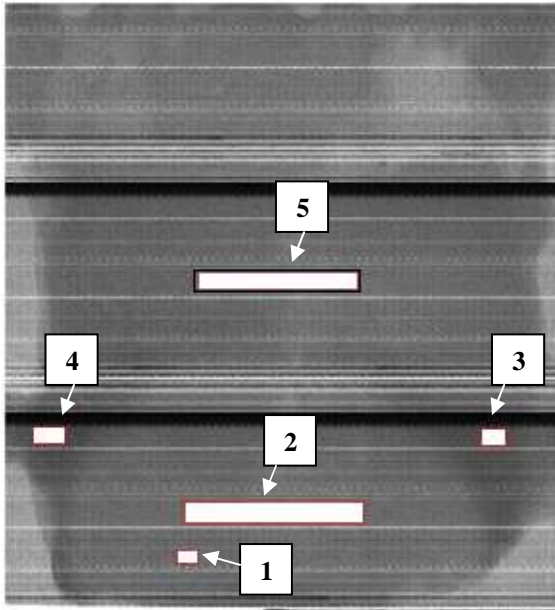


Figure 4.32 Testing pixel values at an original image during polymer injection in the WF+PF sample at 0.19 PV.

Areas which possess little noise (different numerated rectangular in *Figure 4.32*) have been checked for count rates. The size and position of the different rectangular corresponds to the areas which are investigated. The average value of each area is shown in *Table 4.20*.

Table 4.20 Counting numbers from red areas in *Figure 4.32*.

Area	Count rate [cps]
1	1415
2	1476
3	1090
4	1005
5	1446

As seen from *Table 4.20*, there is not a large difference in counting numbers from inside of the polymer injection (1) to outside of the injection (2). Zone 1, 2 and 5 confirms this statement. However, in zone 3 and 4 there is quite some difference from the other zones checked which is caused by a higher sodium iodide concentration.

The zone around the injection front (the half circle in *Figure 4.32*) has higher values than inside and outside the polymer injection. By these tests it seems like the concentration of sodium iodide is higher around the half-circle which indicates no concentration difference in the displacing and displaced fluid. The reason why the polymer injection is visualised is

because of the higher concentration around the injection front. To find out what is causing the increase of concentration around the injection front, more pixel counts are performed at a diagonal path from the inlet, such as the one in *Figure 4.33*.

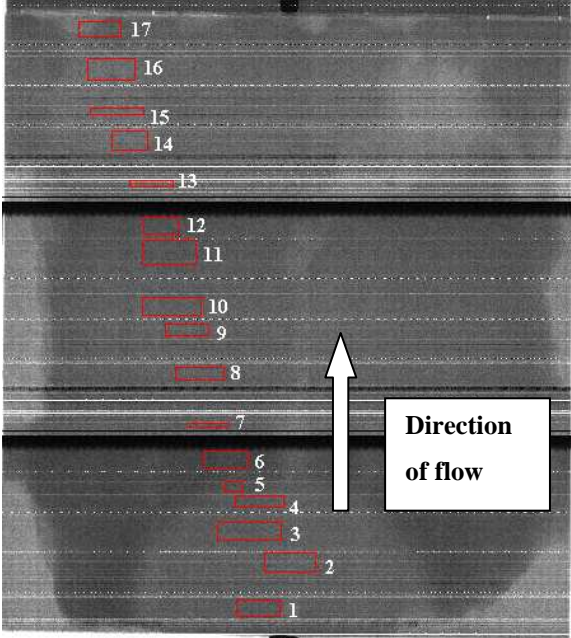


Figure 4.33 Testing pixel values at 0.09 PV of an unmodified image during polymer injection in the WF+PF sample.

The red zones correspond to the path investigated. In addition to the investigated areas in *Figure 4.33*, pixel value for S_{wi} to the left in the image is also checked. Values are plotted as a function of area (*Figure 4.34*)

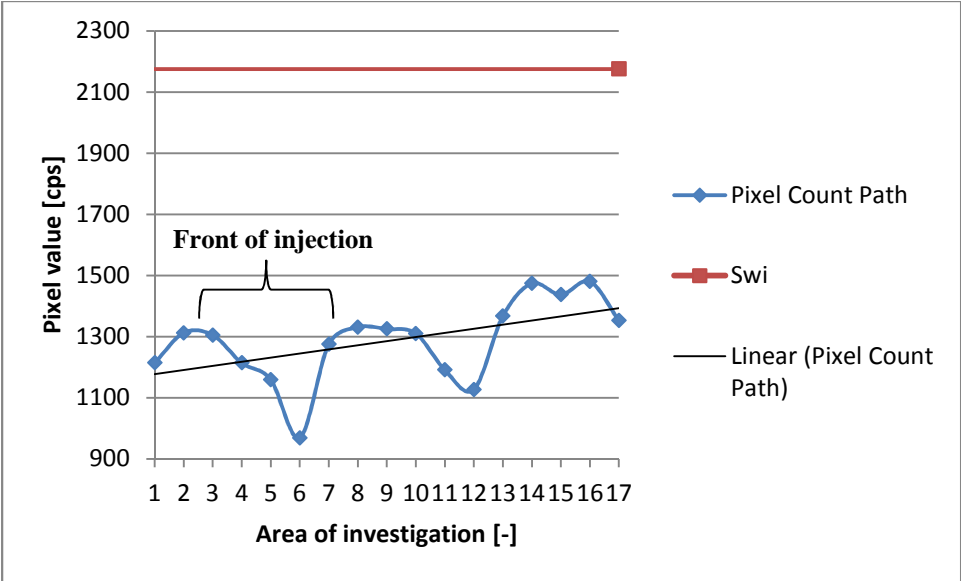


Figure 4.34 Pixels values from Figure 4.33.

The trend in *Figure 4.33* is increasing from the injection point towards the producer, which means that the water saturation is decreasing. Note that low counting value is a sign of high water saturation. Around the injection front a significant decrease is observed around point 6. This would have to mean that there is a higher concentration of water at the front than what is originally mixed in the water and polymer solution. A decrease is observed around point 12, which indicate a low concentration of water at that specific point. This might be the effect of the angle of the X-rays, where intensity is lower at the top and bottom of the images (*Chapter 3.4.4*).

A straight forward path is investigated at different pore volume injected (*Figure 4.35*) to try and investigate the reduction of oil saturation.

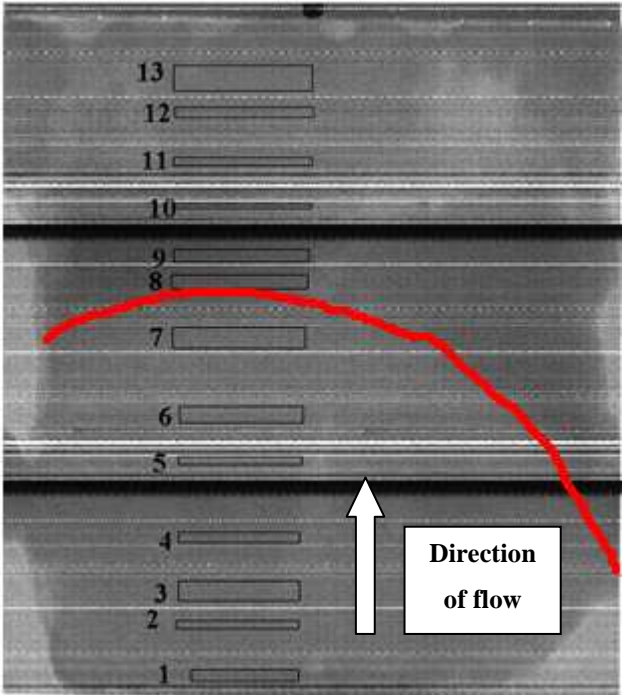


Figure 4.35 Testing pixel values at 0.33 PV of an unmodified image during polymer injection in the WF+PF sample. Front of injection marked in red.

The black rectangular correspond to the area of the path investigated. In addition to the investigated areas in *Figure 4.35*, S_{wi} is also checked in the left side of the sample.

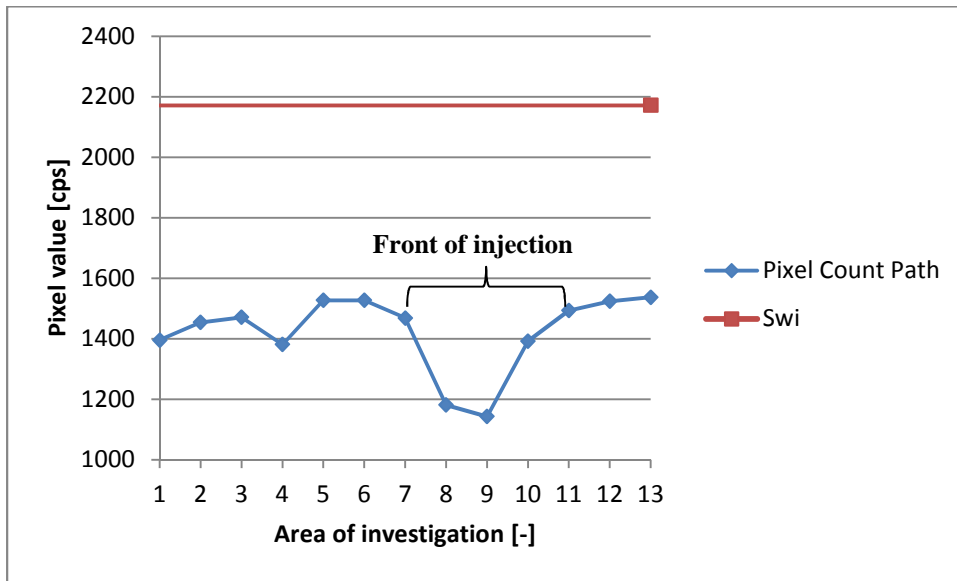


Figure 4.36 Pixels values from Figure 4.35.

From *Figure 4.36* the front of the polymer injection is observed from area 7 to 11. It is observed a small increase in pixel value along the sample, but probably not enough to represent a reduction in residual oil saturation. This can be explained by the dispersion tests which proved little or no dead-end pore volume. The polymer can only reduce the residual oil saturation by its viscoelastic effect on the dead-end type of pores. If no pores like this were existent, the polymer solution could not affect the residual oil saturation.

PF sample:

As in the WF+PF, an unexpected observation occurred. During the polymer injection, a dark ring surrounded the displacement front. The phenomenon with the black ring around the displacement front in *Figure 4.21* must be discussed. MATLAB is used to check the count rates in some specified sections of *Figure 4.37*.

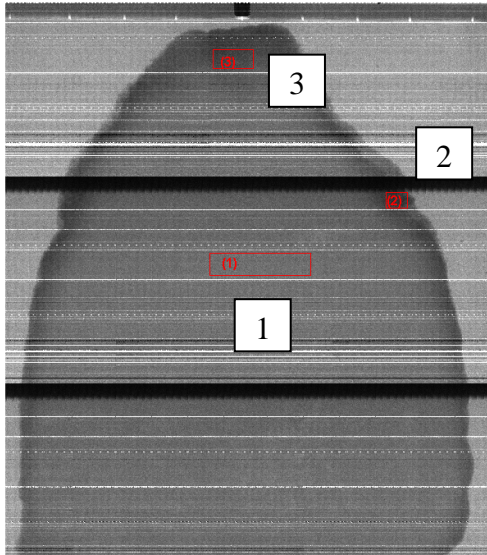


Figure 4.37 Testing the tracer concentration from the direct polymer injection in the PF sample. The image is the unmodified image at 0.52 PV from *Figure 4.21*. Red zones haven been checked for counting rates.

Areas which possess little noise, i.e. different numerated red rectangular in *Figure 4.37*, have been checked for count rates. The size and position of the red zones corresponds to the areas investigated. The average values from the investigated zones are shown in *Table 4.21*.

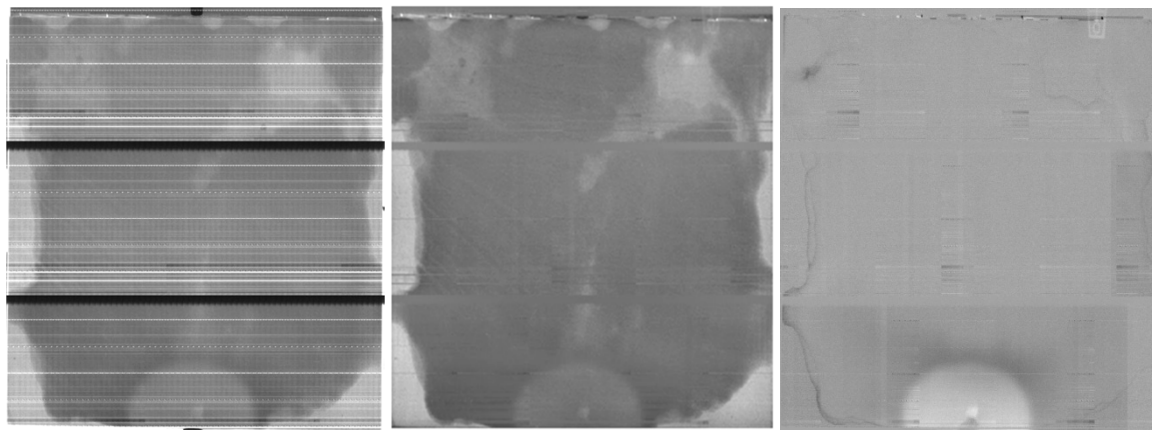
Table 4.21 Counting rates from red areas in *Figure 4.37*.

Area	Count rate [cps]
1	1538
2	757
3	1000

As seen from *Table 4.21*, there is quite some deviation from the different zones. Note that low numbers indicate a zone with a high concentration of sodium iodide (NaI). Zone 1 indicates the lowest NaI-concentration measured, and is located in the middle of the polymer injection. Zone 2 has the highest concentration of NaI and is located at the upper right side in *Figure 4.37*. Investigated zone 3 has an intermediate value compared to the other two zones. This is just below the tip of the front. The edge of the injection consistently has higher concentration of sodium iodide. The PF sample show the same properties as the WF+PF sample, which is a consequently higher NaI concentration at the darker areas around the injection front.

4.6 Image filtration

In the end of this thesis image filtration was applied to see the difference in image quality. A filter derived in MATLAB by a PhD student at CIPR show the transformation in image quality.



Original image

Filtered image

Retracted image

Figure 4.38 Polymer injection at 0.04 PV in the WF+PF sample illustrated by different versions of one specific image.

A clear difference is observed in *Figure 4.38* where the original image is simply raw data from the X-ray camera and the two other images are filtered and retracted from the initial image (i.e. before polymer injection).

The reduction of has clearly improved the image and filtered image reveals a much more detailed image where it is easier to observe partially swept zones and saturation distribution. In the retracted image only differences are observed, and can be useful to see which areas has been swept.

A combination of more processing of images with this applied filter together with a better quality of the X-ray camera could have improved the visual results with regards to details. However, it is possible to improve the results in future works.

5 Conclusions

The scope of this thesis was to investigate mechanisms behind increased recovery of viscous oil due to polymer injection and compare recovery between primary to secondary polymer injection in two similar samples called WF+PF and PF respectively. At water-wet conditions, capillary forces would dampen any viscous fingers formed. To investigate the effect polymer may have on the displacement of oil, an initial condition with dampened capillary pressure is preferred. Ageing rock material with crude oil at elevated temperature is assumed to alter wettability and thereby dampen capillarity.

High values of relative oil permeability most likely exclude an oil-wet porous medium. The relative water permeability of the WF+PF sample, which is not a good indicator in this case due to the inlet and outlet configuration, supports a water-wet sample. Fingering and capillary end-effects indicate that the sample is not strongly water-wet. The low residual oil saturation also indicates a change in wettability towards intermediate-wet.

Effluent dispersion tests revealed homogeneous samples where flow is little affected by dead-end pore volume, but more by the configuration of the inlet and outlet.

During the polymer injection in the WF+PF sample, no oil bank is observed, which might indicate that the same production could have been achieved by a continuation of the water injection. However, the water-cut is kept relatively constant during the injection, implying that the effect of the polymer cannot be excluded. The polymer front arrived 0.4 pore volumes earlier than the dispersion front in the WF+PF sample, something which indicates inaccessible pore volume and depleted layer effects.

A piston-like displacement is observed in primary polymer injection in the PF sample compared to the unstable water injection in the WF+PF sample.

The polymer injections basically reached the same recovery in both samples, but the WF+PF sample needed approximately 1 *PV* of water in addition to 1 *PV* of polymer solution to achieve the same recovery as the PF sample. This shows that polymer injection accelerates the recovery. The high recovery efficiency might be explained by low capillary forces due to high permeable material, in addition to a change in wettability towards intermediate-wet. No dramatic change in polymer viscosity is observed in the polymer injections, which indicate limitations in mixing between water and polymer and little mechanical degradation.

The chase water injections fingered through the polymer solution, which indicate an unstable miscible displacement, i.e. an unfavourable scenario.

Investigations of pixel values to images have identified water saturation along the samples. These tests show that the residual oil saturation has not decreased significantly by the viscoelastic effect in this Bentheimer rock material. The most likely reason for such a case is that the effluent dispersion tests revealed that few dead-end pores were existent in the samples, which is the spaces that is the target for the viscoelastic effect.

Injection of polymers revealed a dark zone surrounding the polymer injection in both samples. It is difficult to explain the dark zone, which has a higher sodium iodide concentration than the displacing and displaced fluid. The area displaced on the images corresponds to the volume injected, which indicates that images obtained are a true description of the front displacement.

6 Recommendations and Further Work

There are a lot of room for improvement related to experimental work on polymer injection in porous material.

The wettability alteration procedure might be changed with regards to a higher temperature. A Wettability closer to neutral-wet might yield a different flow regime with more fingering, and hence more visualised effects during polymer injection.

Maximizing contrasts by alternating between sodium iodide and sodium chloride in every other injection, together with image filtration might give better images which are easier to interpret. More detailed effluent profiles can be achieved by a more accurate accumulation of the effluent production.

Automatically preset sequenced X-ray imaging would provide a larger quantity of images and therefore a more detailed description of the fluid displacement.

Better setup for the differential pressure equipment could provide relative permeability measurements, whereas pressure points along the sample could give an accurate description of the pressure distribution in the porous media during flow.

Identifying the cause of change in polymer concentration, which is either by mechanical degradation (shear) or by mixing with connate water.

Polymer slug injections can be made to investigate the retention of the porous media, which is compulsory before field testing. Quantification of inaccessible pore volume in a specific porous material will give useful information about rock characteristics.

The dark ring observed in the polymer injections can be an area of further investigation. More accurate measurements using smaller measuring cylinders in addition to concentration measurements could yield useful information about this phenomenon.

7 References

1. Sorbie, K.S. (1991) "*Polymer Improved Oil Recovery*". Blackie and Son, Glasgow.
2. Skauge, A., Sorbie, K., Ormehaug, P. A and Skauge, T. (2009) "*Experimental and Numerical Modeling Studies of Viscous Unstable Displacement*". 15th European Symposium on Improved Oil Recovery. Paris, France. April 27-29.
3. Bondino, I., Nguyen, R., Hamon, G., Ormehaug, P. A., Skauge, A and Jouennes, S. (2011) "*Tertiary Polymer Flooding in Extra-Heavy Oil: An Investigation using 1D and 2D Experiments, Core Scale Simulation and Pore Scale Network Models*". International Symposium of the Society of Core Analysis. Austin, Texas, USA. September 18-21.
4. Davenport, B. (2008) "*Biofuels 2008 and the Impact on Chemicals*". Available from: http://www.sriconsulting.com/SSC/Public/biofuels_2008/.
5. Wassmuth, F.R., Green, K., Hodgins, L and Turta, A.T. (2007) "*Polymer Flood Technology for Heavy Oil Recovery*". Petroleum Society's 8th Canadian International Petroleum Conference. Calgary, Alberta, Canada. June 12-14.
6. Asghari, K. and Nakutnyy, P. (2008) "*Experimental Results of Polymerflooding of Heavy Oil Reservoirs*". Canadian International Petroleum Conference. Calgary, Alberta. June 17-19.
7. Wang, J. and Dong, M. (2009) "*Optimum Effective Viscosity of Polymer Solution for Improving Heavy Oil Recovery*". Journal of Petroleum Science and Engineering. **67**: p. 155-158.
8. Mai, A. and Kantzas, A. (2009) "*Heavy Oil Waterflooding: Effects of Flow Rate and Oil Viscosity*". Petroleum Society's 8th Canadian International Conference. Calgary, Alberta, Canada. June 12-14.
9. Kamaraj, K., Zhang, G., Liu, Y and Seright, R.S. (2011) "*Effect of Residual Oil Saturation on Recovery Efficiency during Polymer Flooding of Viscous Oils*". OTC Arctic Technology Conference. Houston, Texas, USA. February 7-9.
10. Wang, D., Xia, H., Liu, Z and Yang, Q. (2001) "*Study of the Mechanism of Polymer Solution With Visco-Elastic Behavior Increasing Microscopic Oil Displacement Efficiency and the Forming of Steady Oil Thread Flow Channels*". SPE Asia Pacific Oil and Gas Conference and Exhibition. Jakarta, Indonesia. 01/01-2001.
11. Yin, H., Wang, D and Zhong, H. (2006) "*Study on Flow Behaviors of Viscoelastic Polymer Solution in Micropore With Dead End*". SPE Annual Technical Conference and Exhibition. San Antonio, Texas, USA. September 24-27.
12. Delshad, M., Kim, D. H., Magbagbeola, O. A., Huh, C., Pope, G. A and Tarahhom, F. (2008) "*Mechanistic Interpretation and Utilization of Viscoelastic Behavior of Polymer Solutions for Improved Polymer-Flood Efficiency*". SPE/DOE Symposium on Improved Oil Recovery. Tulsa, Oklahoma, USA. April 20-23.
13. Taber, J.J., Martin, F. D and Seright, R.S. (1997) "*EOR Screening Criteria Revisited - Part 1: Introduction to Screening Criteria and Enhanced Recovery Field Projects*". SPE Reservoir Engineering. **12**(3): p. 189-198.
14. Lake, L.W. (1989) "*Enhanced Oil Recovery*". Old Tappan, New Jersey; Prentice Hall Inc.
15. Alagic, E. and Skauge, A. (2010) "*Combined Low Salinity Brine Injection and Surfactant Flooding in Mixed–Wet Sandstone Cores*". Energy & Fuels. **24**(6).

16. Alagic, E., Spildo, K., Skauge, A and Solbakken, J.S. (2011) “*Effect of Crude Oil Ageing on Low Salinity and Low Salinity Surfactant Flooding*”. Journal of Petroleum Science and Engineering. **78**(2): p. 220-227.
17. Åm, K., et.al. (2010) “*Økt utvinning på norsk kontinentalsokkel*”. Available from: <http://www.regjeringen.no/upload/OED/pdf%20filer/Oktutvinning.pdf>.
18. Skarestad, M. and Skauge, A. (2009) “*PTEK 213 - Reservoarteknikk II*”. University of Bergen. Bergen.
19. Dake, L.P. (1978) “*Fundamentals of Reservoir Engineering*”. Developments in petroleum science 8, Amsterdam Boston: Elsevier. xv, 443 s.
20. Chatzis, I., Morrow, N. R and Lim, H.T. (1983) “*Magnitude and Detailed Structure of Residual Oil Saturation*”. SPE Journal **23**(2): p. 311-326.
21. Brownell, L.E. and Katz, D.L.V. (1949) “*Flow of Fluids through Porous Media Part II*”. Chem.Eng.Process. Vol. 43.
22. Skjæveland, S.M. and Kleppe, J. (1992) “*Recent Advances in Improved Oil Recovery Methods for North Sea Sandstone Reservoirs*”. SPOR Monograph, Stavanger, Norway: Norwegian Petroleum Directorate. XIX, 335.
23. Dullien, F.A.L. (1979) “*Porous Media: Fluid Transport and Pore Structure*”. New York: Academic Press. XX,396 s.
24. Zolotukhin, A.B. and Ursin, J.R. (2000) “*Introduction to Petroleum Reservoir Engineering*”. Kristiansand: Høyskoleforlaget. VIII, 407 s.
25. Selley, R.C. (1998) “*Elements of Petroleum Geology*”. San Diego: Academic Press. XVI, 470 s
26. Lien, J.R. (2009) “*PTEK 212 - Reservoarteknikk I*”. University of Bergen. Bergen.
27. Solbakken, J.S. (2010) “*An Experimental Study of Low Salinity Surfactant flooding in Low Permeability Berea Sandstone*”. MS Thesis, Department of Chemistry, University of Bergen, Bergen.
28. Craig, J. and Forrest, F. (1971) “*The Reservoir Engineering Aspects of Waterflooding*”. Society of Petroleum Engineers of AIME, New York.
29. Anderson, W.G. (1986a) “*Wettability Literature Survey - Part 1: Rock/oil/Brine interactions and the Effects of Core Handling on Wettability*”. Journal of Petroleum Technology. **39**(10): p. 1125-1144.
30. Anderson, W.G. (1986b) “*Wettability Literature Survey - Part 2: Wettability Measurement*”. Journal of Petroleum Technology. **38**(11): p. 1246-1262.
31. Morrow, N.R. (1990) “*Wettability and Its Effect on Oil Recovery*”. SPE Journal of Petroleum Technology. **42**(12): p. 1476-1484.
32. Marshak, S. (2005) “*Earth: Portrait of a Planet*”. Second ed, New York: W.W. Norton & Company Inc.
33. Du, D., Zitha, P. L. D and Uijttenhout, M. (2005) “*Carbon Dioxide Foam Rheology in Porous Media: A CT Scan Study*”. SPE International Improved Oil Recovery Conference in Asia Pacific. Kuala Lumpur, Malaysia. 01/01/2005.
34. Morel, D.C., Jouenne, S., Vert, M and Nahas, E. (2008) “*Polymer Injection in Deep Offshore Field: The Dalia Angola Case*”. SPE Annual Technical Conference and Exhibition. Denver, Colorado, USA. September 21-24.
35. Pye, D.J. (1964) “*Improved Secondary Recovery by Control of Water Mobility*”. Journal of Petroleum Technology. **16** (8): p. 911-916.
36. Sandiford, B.B. (1964) “*Laboratory and Field Studies of Water Floods Using Polymer Solutions to Increase Oil Recoveries*”. Journal of Petroleum Technology. **16**(8): p. 917-922.
37. Mungan, N., Smith, F. W and Thompson, J.L. (1966) “*Some Aspects of Polymer Floods*”. SPE Journal of Petroleum Technology. **19**(09): p. 1143-1150.

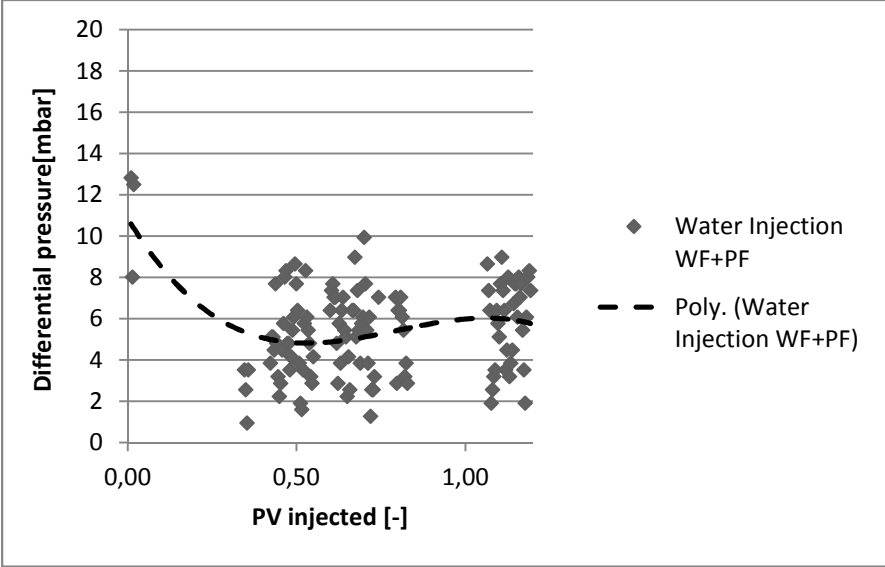
38. Gogarty, W.B. (1967) "*Mobility Control With Polymer Solutions*". SPE Journal. **7**(2): p. 161-173.
39. Schowalter, W.R. (1978) "*Mechanics of non-Newtonian Fluids*". Oxford: Pergamon Press. XIII, 300 s.
40. Wikipedia. (2004) "*Viscosity*". Available from: <http://en.wikipedia.org/wiki/Viscosity>.
41. Lunestad, S. (2011) "*Characterisation of Linked Polymer Solution (LPS) - Influence of salinity and divalent ions*". MS Thesis, Department of chemistry, University of Bergen, Bergen.
42. Hu, Y., Wang, S. Q and Jamieson, A.M. (1995) "*Rheological and Rheoptical Studies of Shear-Thickening Polyacrylamide Solutions*". Macromolecules, American Chemical Society. **28**(6): p. 1847-1853.
43. Dawson, R. and Lantz, R.B. (1972) "*Inaccessible Pore Volume in Polymer Flooding*". SPE Journal. **12**(5): p. 448-452.
44. Moctezuma-Berthier, A. and Fleury, M. (2000) "*Permeability Mapping on Vuggy Core Sample Using Tracer Experiments and Stream-Line Simulations*". SPE International Petroleum Conference and Exhibition in Mexico. Villahermosa, Mexico. February 1-3.
45. Sorbie, K.S. (1989) "*Network Modeling of Xanthan Rheology in Porous Media in the Presence of Depleted Layer Effects*". SPE Annual Technical Conference and Exhibition. San Antonio, Texas. October 8-11.
46. Perkins, T.K. and Johnston, O.C. (1963) "*A Review of Diffusion and Dispersion in Porous Media*". SPE Journal. **3**(1): p. 70-84.
47. Crank, J. (1979) "*The Mathematics of Diffusion*". Oxford: Oxford University Press.
48. Austgulen, M.M. (2009) "*Permeability and Dispersion in Porous Media by Dynamic NMR*". MS Thesis, University of Bergen, Bergen.
49. Grane, F. (1961) "*Measurements of Transverse Dispersion in Granular Media*". Journal of Chemical & Engineering Data. **6**(2): p. 283-287.
50. Brigham, W.E., Reed, P. W and Dew, J.N. (1961) "*Experiments on Mixing During Miscible Displacement in Porous Media*". SPE Journal. **1**(1): p. 1-8.
51. Van der Poel, C. (1962) "*Effect of Lateral Diffusivity on Miscible Displacement In Horizontal Reservoirs*". SPE Journal. **2**(4): p. 317-326.
52. Aris, R. and Amundson, N.R. (1957) "*Some Remarks on Longitudinal Mixing or Diffusion in Fixed Beds*". AIChE Journal. **3**(2): p. 280-282.
53. Bejan, A. (1984) "*Convection Heat Transfer*". New York: Wiley. 477.
54. Blackwell, R.J. (1962) "*Laboratory Studies of Microscopic Dispersion Phenomena*". SPE Journal. **2**(1): p. 1-8.
55. Horgen, T. (2010) "*An Experimental Study of Unstable Miscible Displacement in Vuggy Carbonate and Sandstone*". MS Thesis, Department of Physics- and Technology, University of Bergen, Bergen.
56. Brigham, W.E. (1974) "*Mixing Equations in Short Laboratory Cores*". SPE Journal. **14**(1): p. 91-99.
57. Legatski, M.W. and Katz, D.L. (1967) "*Dispersion Coefficients for Gases Flowing in Consolidated Porous Media*". SPE Journal. **7**(1): p. 43-53.
58. Carberry, J.J. (1976) "*Chemical and Catalytic Reaction Engineering*". New York: McGraw-Hill. xxi,642 s.
59. Taylor, G. (1953) "*Dispersion of Soluble Matter in Solvent Flowing Slowly through a Tube*". Proceedings of the Royal Society. **219**: p. 186-203.
60. Coats, K.H. and Smith, B.D. (1964) "*Dead-End Pore Volume and Dispersion in Porous Media*". SPE Journal. **4**(1): p. 73-84.

61. Norheim, E. (2010) "*Network Modeling of Linked Polymer Solution: A new EOR method*". MS Thesis, Department of Physics- and Technology, University of Bergen, Bergen.
62. Graue, A., Aspenes, E., Moe, R. W., Baldwin, B. A., Moradi, A., Stevens, J and Tobola, D.P. (2001) "*MRI Tomography of Saturation Development in Fractures During Waterfloods at Various Wettability Conditions*". SPE Annual Technical Conference and Exhibition. New Orleans, Louisiana. 30 September - 3 October.
63. Huang, D. and M, H.M. (1996) "*Capillary End Effects in Coreflood Calculations*". International Symposium of the Society of Core Analysts. Montpellier, France. September 8-10.
64. Hadley, G.F. and Handy, L.L. (1956) "*A Theoretical and Experimental Study of the Steady State Capillary End Effect*". Fall Meeting of the Petroleum Branch of AIME. Los Angeles, California, USA. October 14-17.
65. Gharbi, R.B., Qasem, F and Peters, E.J. (2000) "*A Relationship Between the Fractal Dimension and Scaling Groups of Unstable Miscible Displacements*". Springer Link. **31**(4): p. 357-366.
66. Saffman, P.G. and Taylor, G. (1958) "*The Penetration of a Fluid into a Porous Medium or Hele-Shaw Cell Containing a More Viscous Liquid*". Proceedings of the Royal Society. **245**(1242): p. 312-329.
67. Skauge, A., Horgen, T., Noremark, B and Vik, B. (2010) "*Experimental Studies of Unstable Displacement in Carbonate and Sandstone Material*". 16th European Symposium on Improved Oil Recovery. Cambridge, UK. April 12-14.
68. Zhang, H.R., Sorbie, K. S and Tsibuklis, N.B. (1997) "*Viscous Fingering in Five-Spot Experimental Porous Media: New Experimental Results and Numerical Simulation*". Chemical Engineering Science. **52**(1): p. 37-54.
69. Chuoke, R.L., Van Meurs, P and Van der Poel, C. (1959) "*The Instability of Slow, Immiscible, Viscous Liquid-Liquid Displacements in Permeable Media*". Society of Petroleum Engineers of AIME. **216**: p. 188-194.
70. Wang, Z., Feyen, J and Elrick, D.E. (1998) "*Prediction of Fingering in Porous Medium*". Water Resources Research. **34**(9): p. 2183-2190.
71. Homsy, G.M. (1987) "*Viscous Fingering in Porous Media*". Annual Review of Fluid Mechanics. Vol. 19. 271-311.
72. Habermann, B. (1960) "*The Efficiency of Miscible Displacement as a Function of Mobility Ratio*". Petroleum Transactions AIME. **219**: p. 264-272.
73. Day, P.P. (1955) "*Electromagnetic Spectrum of Am-241*". Physical Review. **97**(3): p. 689-700.
74. Noremark, B. (2010) "*Experimental study of viscous fingering in miscible displacements*". Master, Department of Physics- and Technology, University of Bergen, Bergen.
75. Sarwaruddin, M. (2003) "*Modeling of capillary pressure hysteresis curves by gamma adsorption technique*". PhD Thesis, NTNU, Trondheim.
76. Riaz, A. and Tchelepi, H. (2006) "*Influence of Relative Permeability on the Stability Characteristics of Immiscible Flow in Porous Media*". Transport in Porous Media. **64**(3): p. 315-338.
77. Seright, R.S., Fan, T and Wavrik, K. (2011) "*New Insights Into Polymer Rheology in Porous Media*". SPE Journal. **16**(1): p. 35-42.
78. Pancharoen, M., Thiele, M. R., and Kovscek, A.R. (2010) "*Inaccessible Pore Volume of Associative Polymer Floods*". SPE Improved Oil Recovery Symposium. Tulsa, Oklahoma, USA. April 24-28.

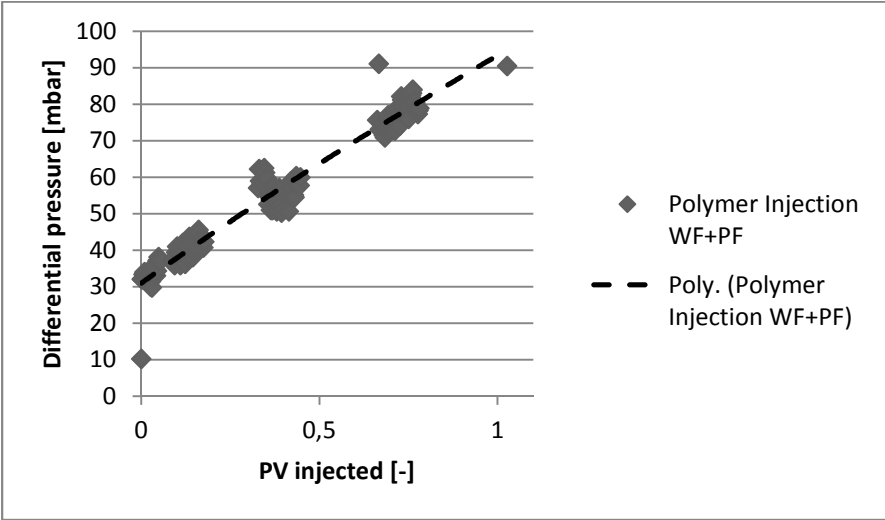
Appendix A: Differential Pressure – Main Injections

WF+PF sample:

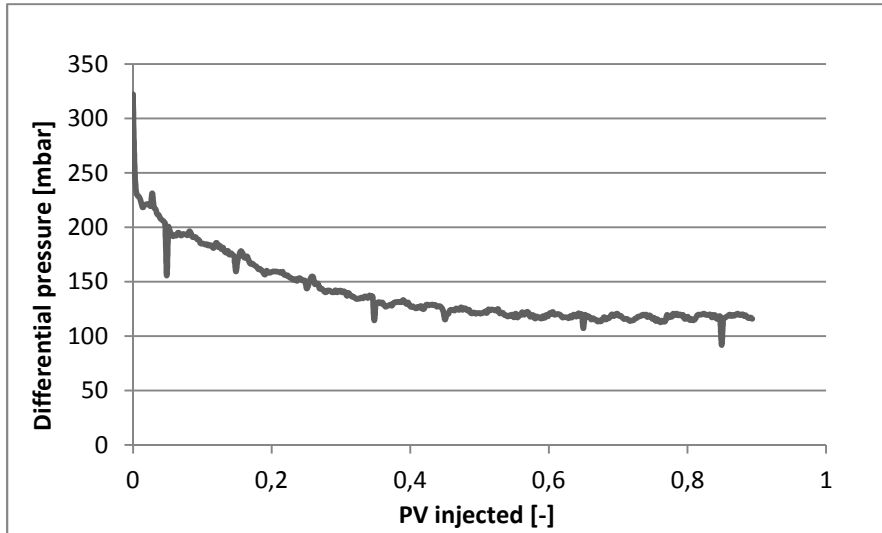
Differential pressure curves for the different injections in the WF+PF sample are found in A - Figure 1 to A - Figure 3. Due to the problems with the differential pressure transmitter, where logging simply stopped at certain periods (note where no data points are present), a trend line is added to illustrate the possible development of pressure.



A - Figure 1 Differential pressure during water injection in the WF+PF sample.



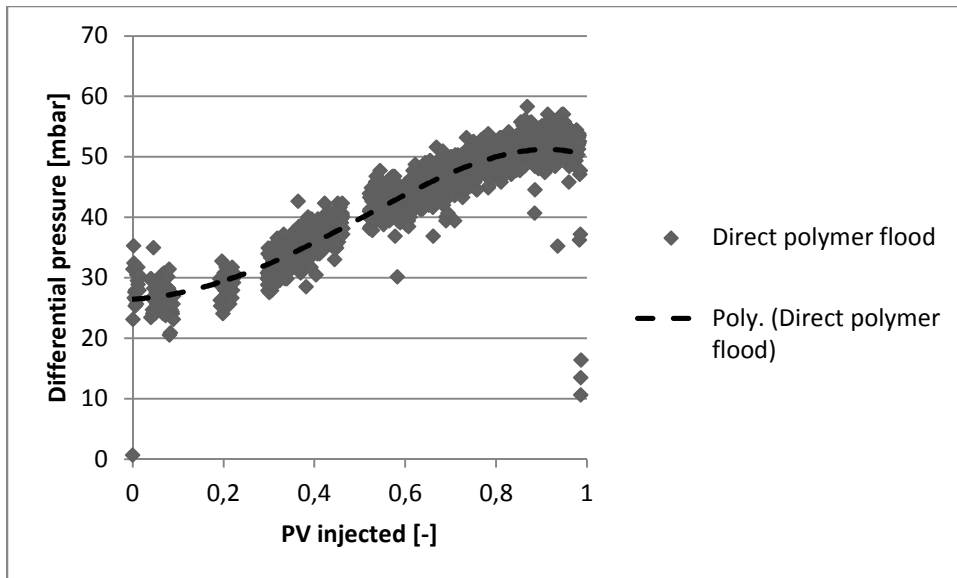
A - Figure 2 Differential pressure during polymer injection in the WF+PF sample.



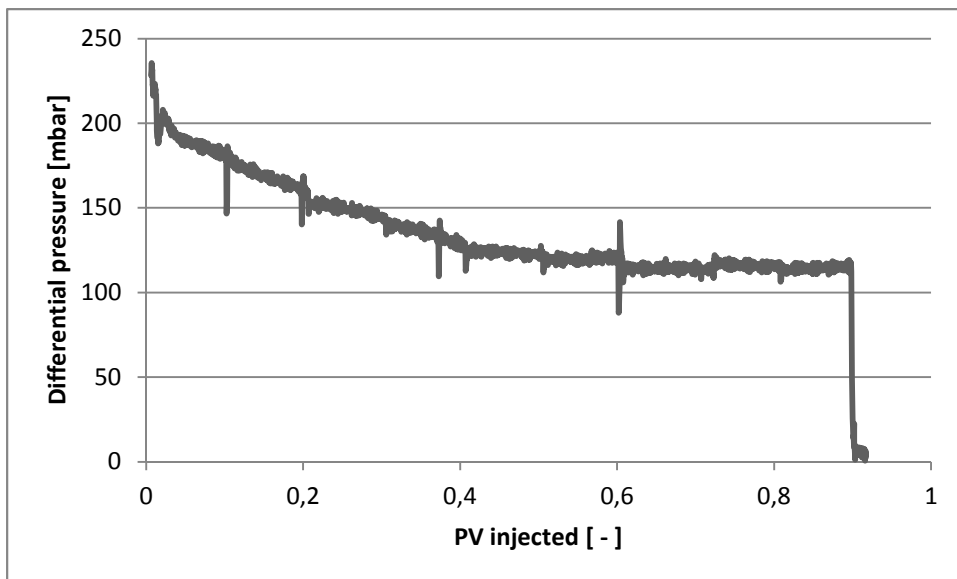
A - Figure 3 Differential pressure during chase water injection in the WF+PF sample.

PF sample:

Differential pressure curves for the different injections in the WF+PF sample are found in A - Figure 4 and A - Figure 5.



A - Figure 4 Differential pressure during polymer injection in the PF sample.



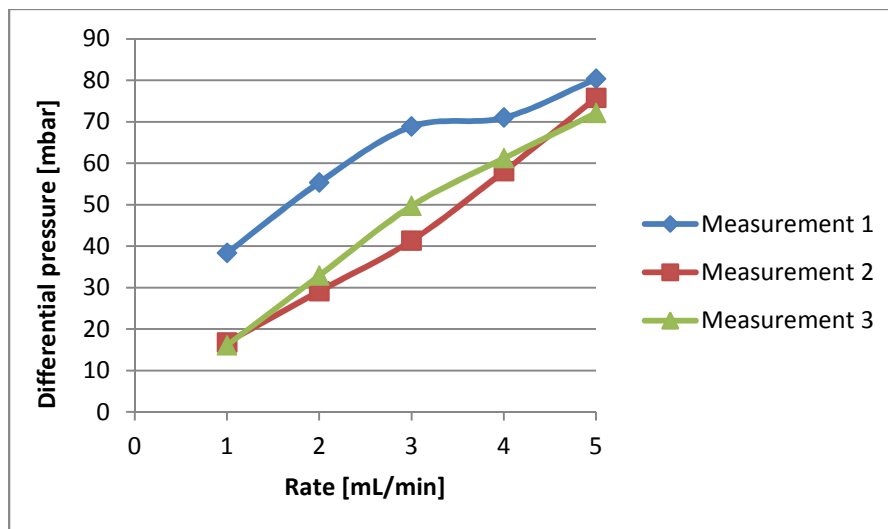
A - Figure 5 Differential pressure during chase water injection in the PF sample.

Appendix B: Differential Pressure – Absolute Permeability

B - Table 1 Permeability measurement data for the WF+PF sample.

Measurement	Rate [mL/min]	Average dp [mbar]
1	1	38
	2	55
	3	69
	4	71
	5	80
2	5	76
	4	58
	3	41
	2	29
	1	17
3	1	16
	2	33
	3	50
	4	61
	5	72

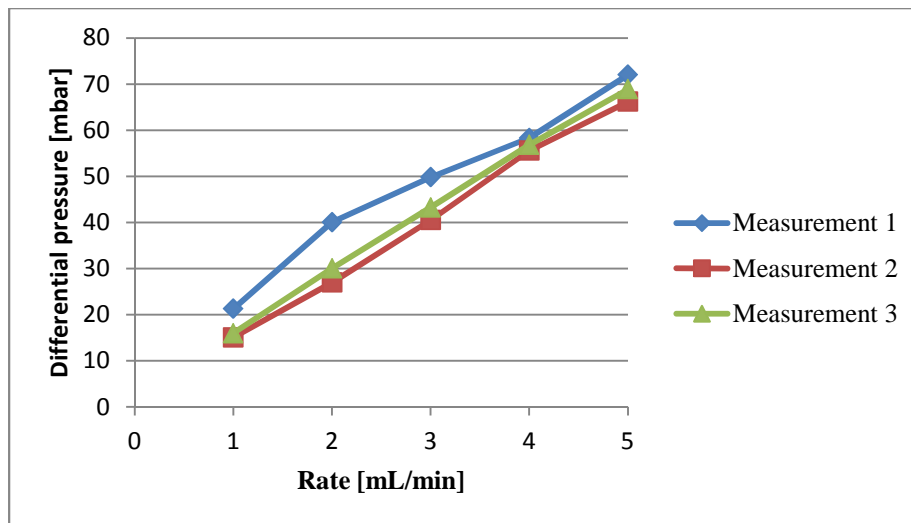
Only measurement 2 and 3 were used due to the poor quality of measurement 1.



B - Figure 1 Permeability measurements for the WF+PF sample.

B - Table 2 Permeability measurement data for the PF sample.

Measurement	Rate [mL/min]	Average dp [mbar]
1	1	21
	2	40
	3	50
	4	58
	5	72
2	5	66
	4	56
	3	41
	2	27
	1	15
3	1	16
	2	30
	3	43
	4	57
	5	69



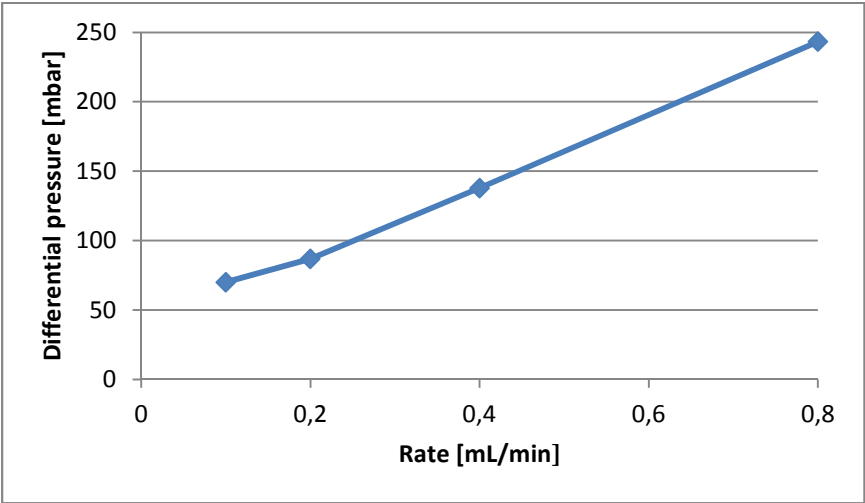
B - Figure 2 Permeability measurements for the PF sample.

Appendix C: Differential Pressure – Relative Permeability

Relative oil permeability:

C - Table 1 Relative oil permeability measurement data for the WF+PF sample.

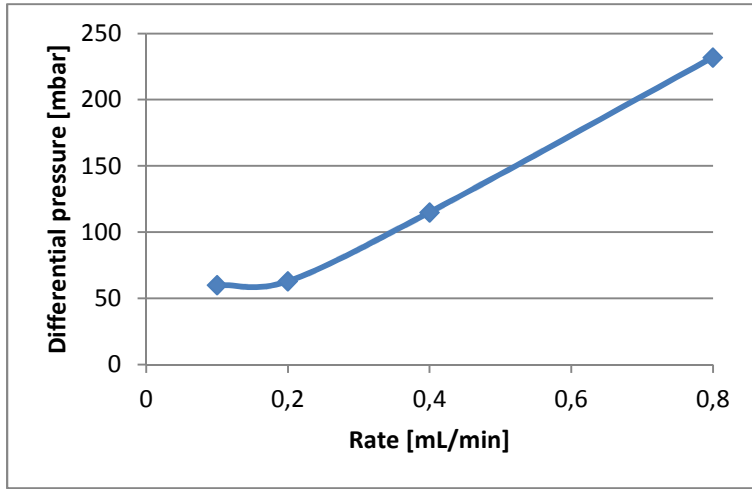
Rate [mL/min]	Average dp [mbar]
0.1	70
0.2	87
0.4	138
0.8	243



C - Figure 1 Relative oil permeability measurement for the WF+PF sample.

C - Table 2 Relative oil permeability measurement data for the PF sample.

Rate [mL/min]	Average dp [mbar]
0.1	60
0.2	63
0.4	115
0.8	232

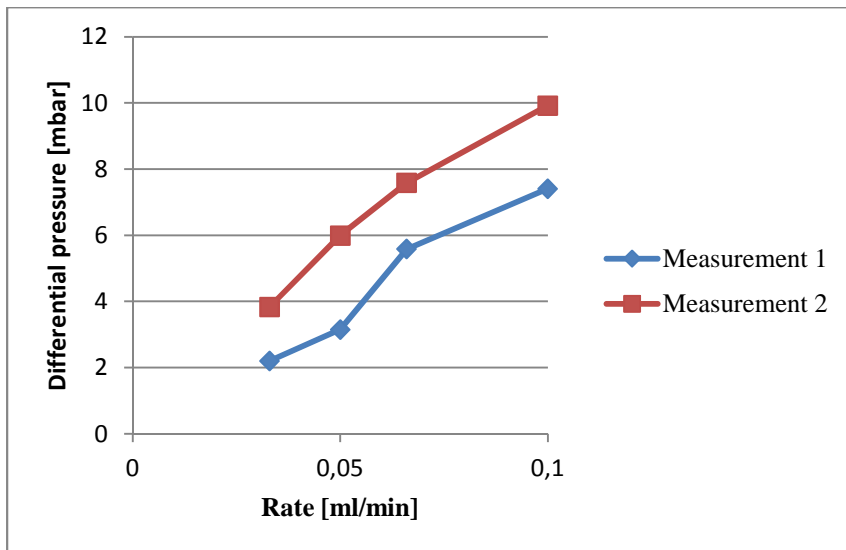


C - Figure 2 Relative oil permeability measurement for the PF sample.

Relative water permeability:

C - Table 3 Relative water permeability measurement data for the WF+PF sample.

Measurement	Rate [mL/min]	Average dp [mbar]
1	0.033	2.2
	0.05	3.2
	0.066	5.6
	0.1	7.4
2	0.1	9.9
	0.066	7.6
	0.05	6.0
	0.033	3.8



C - Figure 3 Relative water permeability measurements for the WF+PF sample.

